Research and Development of GEM based Muon Chamber Detector for the Compressed Baryonic Matter experiment at FAIR

Thesis submitted for the degree of

Doctor of Philosophy (Science)

of the

University of Calcutta

By

Rama Prasad Adak

Regn. No. - 5908 Ph.D.(Sc.) Proceed / 12

Dated - 17/12/2012

Department of Physics

University of Calcutta

2017

Dedicated to my parents

Shri Shib Nath Adak and Smt. Basana Adak

whose endless support helped me in every aspect of my life.

Acknowledgements

This thesis is the collection of the works I have done in the last few years. There are so many people who helped me to reach this state to write a thesis. First of all, I wish to express my sincere gratitude to my research supervisors Prof. Sibaji Raha and Dr. Supriya Das for their continuous support, motivation, patience and knowledge. They help me a lot during my PhD work and writing the thesis. A substantial part of my work has been done in collaboration with Variable Energy Cyclotron Centre. A very special gratitude goes out to Dr. Subhasis Chattopadhyay of VECC, India, for giving me the opportunity to work for the CBM collaboration. His immense knowledge and discussions regarding the works helped me to reach the significant results that help me to write the thesis. I would like to thank Dr. Anand Kumar Dubey, Jogendar Saini of VECC for their support during the experiments related to my works. It is my great pleasure to work with Dr. Saikat Biswas in our laboratory at Bose Institute. I also thank Dr. Sanjay Kumar Ghosh, Dr. Rajarshi Ray and Dr. Sidhartha Kumar Prasad of Bose Institute for their fruitful discussions, suggestions and encouragements.

I have made countless discussions and debates with my dear friends. A special thanks go out to those friends - Subhasis Samanta, Avik Banerjee, Rupamoy Bhattacharyya, Shyam Behari Mehta, Sayan Biswas, Soumitra maity, Kinkar Saha, Sudipa Upadhyay, Prosenjit Deb, Saronath Halder and Arpita Kundu. I also thank my junior research scholars - Rathijit Biswas, Dipanjan Nag, Shreya Roy, Deeptak Biswas, Procheta Singha, Sumana Bhattacharya, Pratapaditya Bej for their helpful discussions.

I offer my heartfelt thanks to my parents Shri Shib Nath Adak and Smt. Basana Adak and other members of my family. Their endless love and support are the key inspiration of my Ph.D.. My thesis would not be completed without them.

I acknowledge the University Grant Commission (Sanction No.- F. No. 2-8/2002 (SA-I)) and Bose Institute for their financial support during my Ph.D..

Abstract

The Compressed Baryonic Matter (CBM) experiment is a future experiment to be held at FAIR, GSI, Germany. The experiment aims to study the properties of the rarely produced particle in order to investigate the behaviour of the matter at extremely high density that prevails in the core of neutron stars and micro seconds after the big-bang. The rarely produced particles will be reconstructed via their decay into dileptons i.e. via decay into dimuons or electron-positron pairs. A Muon Chamber (MUCH) using segmented absorbers has been proposed for the detection of the dimuons. The interaction rate of the ions in this fixed target experiment will reach up to $\sim$ 10 MHz. In order to identify the rare particles that are signature of the early high density matter created just after the collision, the conventional detector and the data acquisition system will not work at this high particle rate. The data will be acquired in trigger-less mode because during selecting a trigger some data might be missed. Out of the presently available detector technologies, Gas Electron Multiplier (GEM) based detector is suitable to work efficiently at this extremely high rate and in a harsh radiation environment. The efficiency of detection of the GEM should be $>$90% and most importantly they should be capable of handling a particle rate about 1 MHz/cm^2. In the direction of developing the MUCH detection system, several Research and Development (R& D) on GEM has been arrived on. In this thesis, the R & D with the GEM prototypes has been described in detail. The R & D works started with a small 10 cm$\times$10 cm prototype GEM detector. The small prototype was successfully tested in laboratory and using ion beam with efficiency $>$95%. The tracking residue of the array of 3 GEM prototypes has been found to be 0.12 cm. After this, a medium size (31 cm$\times$31 cm) trapezoidal GEM detector was tested using proton beam with efficiency $>$95%. The main challenge is to make the detector capable of handling high flux of particles. A large trapezoidal GEM detector was successfully tested using intense proton beam with high efficiency. This prototype has uniformity of efficiency and gain up to 2 MHz/cm^2, this rate is well above the particle rate expected at the 1^{st} detector station of the MUCH detector. The detectors will have to be operated in an environment with very high level of radiation, so the long-term stability of the detector should be verified. A small 10 cm$\times$10 cm GEM prototype has been tested in laboratory for its performance on long-term basis. The normalised gain of the detector is stable with mean at 1.003 with sigma of 0.086 up to a charge acquisition of 12 mC/mm^2. No ageing of the detector is observed in the detector. So large GEM detector can be used to design a muon detection system for the CBM experiment for the detection of the muons with high efficiency and without any ageing.

Declaration

I do hereby declare that the investigations presented in this thesis are my own contributions under the guidance of Prof. Sibaji Raha and joint supervision of Dr. Supriya Das. This work has not been submitted anywhere as a whole or in part for requirement of any degree/diploma under this university or any other university/institute.

Rama Prasad Adak

(Sign. of Candidate)

List of Publications

Journals

- Performance of a large size triple GEM detector at high particle rate for CBM Experiment at FAIR*, **Rama Prasad Adak** et al., Nucl. Instr. Meth. A **846** (2017) 29-35, arXiv:1604.02899v2.
- Long-term stability of a triple GEM detector*, **R. P. Adak** et al., Journal of Instrumentation 11 (2016) T10001., arxiv:1608:00562v1.
- Design and performance simulation of a segmented-absorber based muon detection system for high energy heavy ion collision experiments, S. Ahmad, **R. Adak** et al., Nucl. Instr. Meth. A **775** (2015) 139–147.
- Testing of Track Point Resolution of Gas Electron Multiplier with Pion Beam at CERN SPS*, **R. P. Adak** et al., Indian National Science Academy **81** No. 1 February 2015 Special Issue, pp. 36-39.
- Challenges in QCD matter physics — The scientific programme of the Compressed Baryonic Matter experiment at FAIR, T. Ablyazimov et al., Eur. Phys. J. A **53** (2017) 60., arXiv:1607.01487 [nucl-ex].

* - Thesis Publication .

Coference Proceedings

- Test of a triple GEM chamber with neutrons using alpha beam at VECC cyclotron, A. K. Dubey, **R. P. Adak** et al., Proceedings of the DAE Symp. on Nucl. Phys. **58** (2013) 862.
- Testing of Triple-GEM chambers at High Intensity Beam for CBM Experiment, **R. P. Adak** et al., Proceedings of the DAE Symp. on Nucl. Phys. **59** (2014) 840.
- Testing of Large Real-Size GEM Detector for CBM Experiment, **R. P. Adak** et al., Proceedings of the DAE-BRNS Symp. on Nucl. Phys. **60** (2015) 1018.
- Building of a 4-GEM prototype for ALICE-TPC upgrade, S. Swain, **R. P. Adak** et al., Proceedings of the DAE-BRNS Symp. on Nucl. Phys. **61** (2016) 994.
- R & D on Straw Tube detector for CBM Muon Chamber, **R. P. Adak** et al., Proceedings of the DAE-BRNS Symp. on Nucl. Phys. **61** (2016) 996.
- Stability test of the GEM detector, **R. P. Adak** et al., Proceedings of the DAE-BRNS Symp. on Nucl. Phys. **61** (2016) 998.

Internal Notes

- Test of a $31\ cm \times 31\ cm$ GEM chamber at COSY, **R. P. Adak** et al., CBM Progress Report 2013.
- Test of a triple GEM chamber with neutrons using alpha beam at the VECC cyclotron, A. K. Dubey et al., CBM Progress Report 2013.
- Testing of a real-size GEM proto-type at COSY, **R. P. Adak** et al., CBM Progress Report 2014.
- Building of a 4-channel TTL scaler for counting detector signals, S. Sahu, **R. P. Adak** et al., RD51-NOTE-2016-003.

Contents

List of Figures

List of Tables

Chapter 1

Introduction

A charged particle loses a part of its energy by ionising collision with the gas molecules while passing through a gaseous medium. The number of electron-ion pairs created in this process is called primary electron-ion pairs. The charge corresponding to the primary electron-ion pairs created during the ionisation process are not enough to produce a detectable signal over the noise level of the electronics; the charges have to be amplified by further ionisation. The basic working principle of a gaseous detector is based on the ionisation of the gas by the incoming charged particles through electromagnetic interaction. A preliminary knowledge of the interaction of the particle should help in understanding the principle of operation of the gaseous detectors. This chapter will introduce the basic working principle of the gaseous detector followed by the micropattern gaseous detectors used in the high energy heavy-ion experiments.

1.1 Interaction of charged particle with matter

A charged particle passing through a gas or solid medium can interact with it through three different types of interactions: the weak, the strong and the electromagnetic interactions. The electromagnetic interaction occurs more frequently because its cross-section is several orders of magnitude higher than the other types of interactions. The weak interaction usually plays a fundamental role in the detection of extremely elusive particles such as the neutrinos; the strong force usually concerns in detecting neutrons (in particular, it refers to nuclear reactions producing charged particles from an incoming neutron). Coulomb interactions between incoming particles and matter, lead to two important phenomena: the excitation and the ionisation of the atoms of the medium. Ionisation stands for the creation of an electron-positive ion pair, while excitation signifies the generation of an atomic state with higher energy. De-exciation of an atom from the excited state can also libearte electrons. All these extracted electrons are called “primary ionisation electrons”. In addition, if these electrons can acquire additional energy (when an external electric field is present) they can further ionise, creating the so-called secondary delta electrons. A charged particle usually releases energy along all its path inside the medium and creates clusters of ions/electrons. Other electromagnetic processes, such as Bremsstrahlung, Cherenkov and transition radiation may occur; but in the case of a gaseous detector, they are negligible and can be ignored.

1.1.1 Energy loss by heavy charged particle

A heavy charged particle (m >> m_e) loses its energy through electromagnetic interaction with the gaseous medium through many successive interactions. The process of energy loss is a statistical process. The differential loss of energy by a particle divided by the differential path traversed, is called the differential energy loss of a charged particle, S = $-\frac{dE}{dx}$. The classical energy loss formula that describes the specific energy loss of a heavy charged particle is the Bethe-Bloch formula [1] and is given by,

$$\frac{dE}{dx} = \frac{4\pi z^2.e^4.N.Z}{m_0.v^2}[\ \ln\frac{2.m_0.v^2}{I_p} - (\ln(1-\beta^2)) - \beta^2\ ] \tag{1.1}$$

where v and ze represent the velocity and the charge of the incoming particle, N and Z represent the atomic density and the atomic number of the detecting medium, m_0 is the rest mass of electron and e is the unitary electronic charge and $\beta = \frac{v}{c}$. The parameter I_p is the average ionisation potential of the absorber and it is normally treated as an experimentally determined parameter for each element. The average value of the ionisation potential can be written as a function of atomic number as, $I_p = I_0.Z^{0.9}$ with I_0 = 12 eV. Eq. 1.1 is generally valid for different types of charged particles when their velocity is higher than the orbital velocity of the electrons of the absorbing atom. The minimum value of the differential energy loss does not depend on the target medium. This value is about $\sim$ 2 MeV.g^{-1}.cm^2 at a value of β= 0.95. The charged particles with this minimum value of average energy loss is called the Minimum Ionising Particles (MIP's). The charged particle having energy lower than the MIP's interacts more with the medium and loses larger amount of energy. The energy loss rises for the particles with higher energy due to the transfer of large energy in the collision. The Bethe-Bloch formula is also valid for the mixture of gases. In this case, the energy losses are added taking into account the necessary weighting factors of the components.

1.1.2 Energy loss by electron and positron

The electrons and the positrons at low energy lose energy through excitations and ionisations. Additional energy loss mechanism by emission of electromagnetic radiation, namely bremsstrahlung [2], become significant due to the small mass of the electron. The rate of energy loss in the case of bremsstrahlung depends on Z^2 and is given by,

$$E(x) = E_0\ exp(-\frac{\rho.x}{X_0}) \tag{1.2}$$

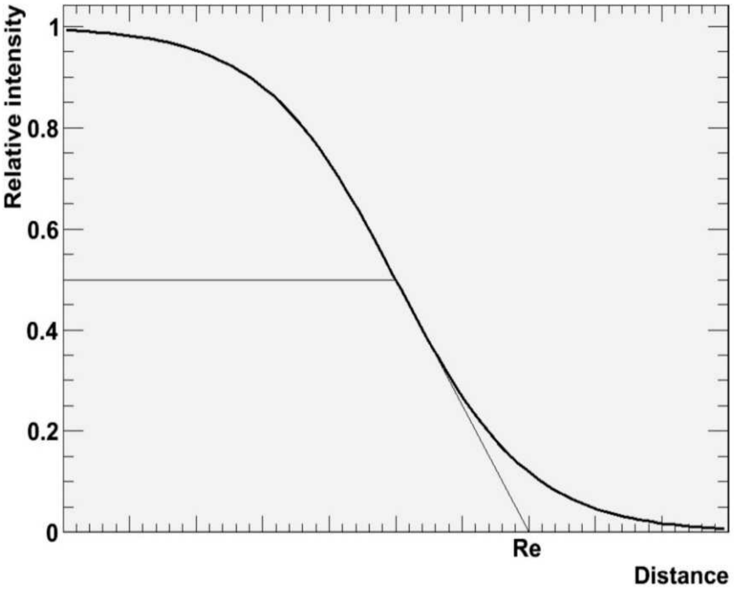

Figure 1.1: The variation of the intensity of the electron with range.

X_0 is the radiation length. The radiation length is defined as the length of the track travelled by the particle by which energy is decreased by a factor of e. The above equation implies that the energy of the charged particle decreases exponentially along the track of the particle. The radiation length is given by Eq. 1.3 for particles with the atomic number greater than 4.

$$\frac{1}{X_0} = \frac{4N_A\alpha {r_e}^2}{A}\{Z^2[\ln\frac{184.15}{Z^{1/3}} - \alpha^2Z^2(\frac{1}{1+\alpha^2Z^2} + 0.20206 - 0.0369\alpha^2Z^2)] + Z\ln\frac{1194}{Z^{\frac{2}{3}}}\} \tag{1.3}$$

α is the fine structure constant and r$_e$ the classical electron radius. The above equation can be written in terms of Z and A as,

$$X_0 = \frac{716.4\ A}{Z(Z+1)\ \ln{(287/\sqrt{Z})}} \tag{1.4}$$

The electron can lose a large amount of energy in a single collision with the orbital electron. They also suffer large deflections. So electrons have many tortuous paths than the heavy charge particles. The penetration depth of electron is smaller than the total path travelled by it. The intensity of a monochromatic electron beam is shown in Fig. 1.1 as a function of the traversed path. A small absorber length can reduce the rate of the electrons substantially. Large deflections in their path can put them out of the acceptance of the detector. Sometimes it is preferable to use the extrapolated range R$_e$ which is a linear extrapolation of the intensity from the half intensity. The value of the absorber corresponds to the length within which almost all electrons will be stopped.

1.1.3 Multiple Coulomb scattering

The trajectory of the charged particles is deflected by many interactions while passing through a medium. Multiple Coulomb scattering is one such interaction. A charged particle is deflected by the Coulomb interaction with the atomic nucleus. The theory of Molière [3] describes the multiple Coulomb scattering. When deflections occur at small angle, the angular distribution is almost Gaussian in nature. For deflection at large angle, the distribution is similar to the Rutherford scattering with a long tail. The distribution in the first case can be represented by,

$$\frac{N}{\theta} = \frac{1}{\sqrt{2\pi}\theta_{RMS}} exp(-\frac{\theta^2}{2\theta_{RMS}^2}) \tag{1.5}$$

θ_{RMS} is the angular deflection and its value can be obtained from the fit to the Molière distribution, given below [4].

$$\theta_{RMS} = 13.6MeV.\frac{Z}{v\,p}\sqrt{\frac{x}{X_0}}.(1 + 0.038 \ln \frac{x}{X_0}) \tag{1.6}$$

where Z is the atomic number, v is the velocity, p is the momentum of the incoming particle and x is the thickness, X_0 is the radiation length of the medium. The formula given in Eq. 1.6 can be applied for any incoming charged particle and its accuracy in the range of $10^{-3} \leq \frac{x}{X} \leq 100$ is 11 % or better than that.

1.2 Ionisation

The energy loss by a charged particle inside a medium can result in excitation or ionisation. In case of the excitation, the atom/molecule of the gas gains energy from the charged particle and jumps up to an excited energy level. The excitation of an atom, X by a charged particle A is given by,

$$A + X \rightarrow A + X^* \tag{1.7}$$

In this reaction, no electron-ion is produced but the excited atom/molecule may participate in further reactions that may lead to ionisation.

When the outermost electron inside the atom is released by the incident radiation, the atom is ionised,

$$A + X \rightarrow A + e^- + X^+ \tag{1.8}$$

The loss of energy of the incoming particle must be greater than the ionisation potential (I_p) of the atom. Since in most of the cases, energy loss is low, the excitation is the dominant process. The electrons and ions created by the incident radiation itself are known as primary ionisation. In presence of an external electric field the electrons are accelerated; otherwise they will recombine with the ion. If the energy of the primary electron is sufficiently high it will also create ion-electron pairs; this ionisation is known as secondary ionisation. The secondary electrons liberated in the gas can produce further ionisation inside the gas if the energy of the secondary electrons is large enough. This process will continue until the energy of the electrons is below the ionisation energy. Ionisation in gas is also possible from the metastable state of an atom. The process is called Penning effect [5]. Some atoms may be excited to a metastable state. The atom does not de-excite to lower state immediately from the metastable state by emission of radiation. In such atoms, a de-excitation may occur through a collision with a second atom resulting in the ionisation of the latter. The molecular gases on noble gases or noble gases on noble gases are the example of Penning effect.

$$Ne * +Ar \rightarrow Ne + Ar^+ + e^- \tag{1.9}$$

Molecular ions may be formed through the interaction of an ionised atom with a neutral atom. This is an important ionisation mechanism in noble gases. For an example,

$$He^+ + He \rightarrow He_2^+ \tag{1.10}$$

1.2.1 Townsend theory of electron avalanche

An electron is created in an ionisation process. If this electron gains sufficient energy it can further ionise another atom and the process of ionisation will continue until the threshold of ionisation is reached. The process of creating electrons leads to electron avalanche. Finally, a large number of electrons will reach the anode. The positively charged ions being heavy, will slowly recede towards the cathode. The electrons have large drift velocity than the heavy ions, so the avalanche of charge will look like a liquid drop with the electrons near the head and the slowly moving ions trailing behind. This avalanche will produce anode current while collected at the anode. If 'l' is the mean free path for a secondary electron, the inverse of the mean free path is called first Townsend coefficient (α) [6], the ionisation probability per unit length for secondary ionisation. The number of electrons produced inside the gas depends on the number of primary electrons that were presented (n_0) and the length of the path travelled by the electron (x). In terms of α it can be written as,

$$n = n_0 \; exp(\alpha x) \tag{1.11}$$

The ratio $\frac{n}{n_0}$ is the multiplication factor. The multiplication factor depends on the choice of the gas and the intensity of the electric field. If the multiplication factor is high enough, about 10^7-10^8 a discharge is created, this limit is called the Raether's limit [7]. The distance travelled by an electron to reach the anode is 'd', then the number of electrons that will reach the anode will be

$$n = n_0 \; exp(\alpha d) \tag{1.12}$$

Here α is assumed to be constant independent of the electric field. Then $(n - n_0)$ is the number of ions created inside the avalanche. It is assumed that all the ions returned to the cathode where they are collected. At the cathode, the ions will release $\gamma_i \; (n - n_0)$ new electrons, where γ_i takes care of the efficiency of the ions impinging on the cathode to release electrons. So the number of electrons leaving the cathode increased to $(n_0 + \gamma_i \; (n - n_0))$. They will be collected at the anode after traversing a distance 'd'. So according to the Townsend's theory of electron avalanche, the total number of electrons reaching the anode will be,

$$n = (n_0 + \gamma_i \; (n - n_0)) \; exp(\alpha d) \tag{1.13}$$

1.2.2 Recombination and electron attachment

The electrons created during ionisation may be lost due to two effects: recombination and electron attachment. In a region where there is no electromagnetic field, the ion and the electron are recombined to form a neutral atom due to their Coulomb attraction. The rate of recombination depends on the concentration of the electron and the ions in the medium along with the intensity of the electromagnetic field present there. The presence of electro-negative atoms in the avalanche region will attract electrons thereby reducing the number of the electron. The atom attracts the electron to form a negative ion.

$$X + e^- \rightarrow X^- + h\nu \tag{1.14}$$

A large number of electrons are captured in the electron attachment process. The efficiency and gain of any gas detector are drastically reduced due to the presence of electro-negative gas like O_2.

1.3 Interaction of photon with matter

Photon being a neutral particle, interacts with matter mainly by three types of interactions - photoelectric effect, Compton effect and pair production. The intensity of the incoming photon decreases as,

$$I = I_0 \; exp(\mu t) \tag{1.15}$$

where t is the thickness of the material travelled by photon and μ is the attenuation constant of the material. Photons interact with matter in several different ways. Each mechanism is characterised by its specific cross-section and the total cross-section is the sum of all the processes.

1.3.1 Elastic Scattering

When a photon suffers an elastic scattering with an atom, the photon is absorbed by the atom and same photon is emitted subsequently without any loss of energy. In this scattering only the direction of the momentum is changed but its magnitude remains the same. The cross-section of such scattering is very low and is not used for detection of photon. The cross-section depends on the energy of the photon and drops above an energy of few keV.

1.3.2 Photoelectric effect

The electrons near the surface of a photosensitive material is emitted when a photon impinges on the surface. The minimum energy required for the electrons to come out of the surface is called the work function of the material. The electron liberated in this process is called photoelectron. Part of the energy of the photon is used for the work function and the rest energy is the kinetic energy with which the photoelectron is liberated. If hν is the energy of the photon and W is the work function of the material, then kinetic energy of the photoelectron is given by,

$$E_k = h\nu - W \tag{1.16}$$

The photon interacts with the bound electrons inside the atom in case of photoelectric effect. So the most tightly bound K or L-shell electrons are knocked out by the interaction of the photon. The vacancy left in the K-shell is subsequently filled up by electrons from other shell and a characteristic X-ray is emitted. The photon does not interact with a single electron but with the atom as a whole. Photoelectric effect is the dominant process for the interaction of photon of relatively low energy. The interaction cross-section of a photon from different mechanisms in carbon and lead are shown in Fig. 1.2. The cross-section of photoelectric effect depends on the shell from which the photoelectron is ejected. There are discontinuities in the cross-section called absorption edges. The energies at the discontinuities are observed at the binding energies of the various shells. The highest absorption edge is seen for K shell and next for the L shell and so on. The only absorption edge for carbon is outside the considered energy range and the edge is not present in Fig. 1.2 (left). The photoelectric cross-section increases for the interaction of a photon having energy slightly higher than the edge because in this case, the photon can access the electrons in the inner shell. If the energy is just below the edge, the cross-section decreases sharply. No universal formula exists to describe how the cross-section depends on the energy of the incoming photon and the atomic number (Z) of the material, but an empirical scaling law can be written as,

$$\sigma_{photoelectric\ effect} = \frac{Z^n}{E^3} \tag{1.17}$$

here n is function of energy and its value is between 4 to 5 [8]. The photoelectron is

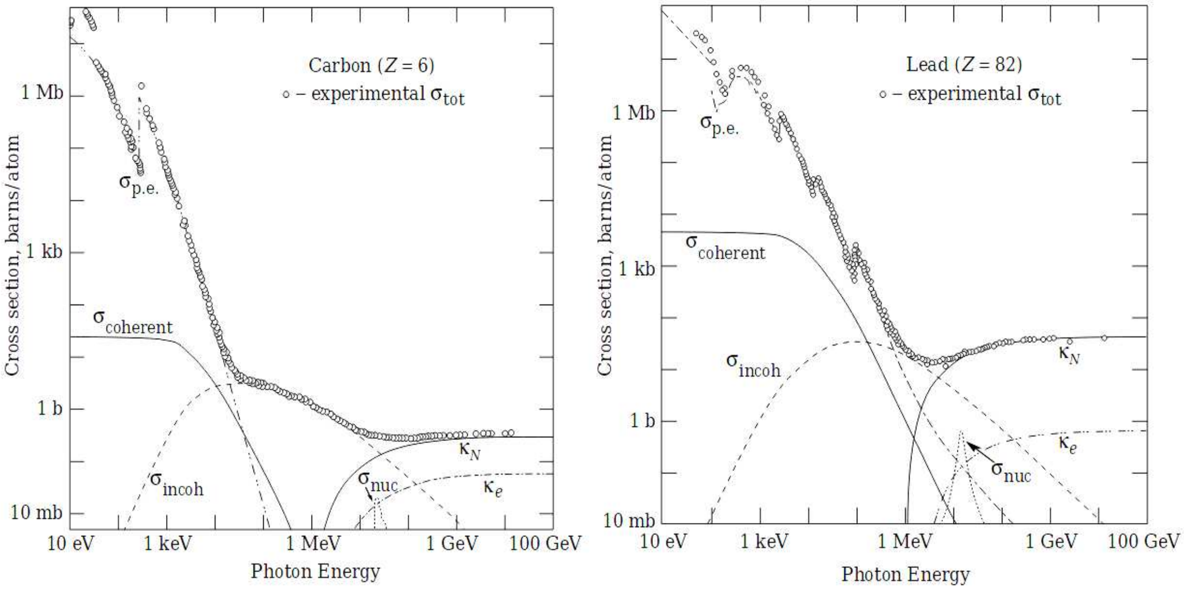

Figure 1.2: The total cross-section of a photon in light element, carbon (left) and in a heavy element lead (right). The contribution to the total cross-section are from $\sigma_{p.e.}$ = photoelectric effect, $\sigma_{Rayleigh}$ = Rayleigh scattering, $\sigma_{Compton}$ = Compton scattering off an electron, k_{nuc} = Pair production from nuclear field, k_e = Pair production from electron field.

emitted with the energy equal to the difference in energy of the photon and the binding energy of the electron in the atom. The angular momentum is conserved with the momentum carried by the atom. Photoelectron emission is not an isotropic process. At lower energies, the effect is controlled by the photon electric field and a bipolar angular distribution is obtained. For high energy of the photon, the electrons are Lorentz boosted, so the two angular distribution lobes are squeezed in forward direction. The vacancy created in the atomic shell is quickly filled up by another electron from other shells. As a result, a characteristic X-ray or Auger electron [9] is produced. Auger transition occurs mainly for light materials while a fluorescent production is seen in the case of high Z material. The Auger electron mostly deposits all of its energy near its origin because of the short range. The emitted X-rays are absorbed near the interaction point through another photoelectric effect by knocking loosely bound electron from another atom. The energy of the incoming photon will be equal to the sum of the total kinetic energy of all the electrons when no radiation is coming out of the detector. Ideally, there should be a sharp delta function in the energy spectrum. Practically, one gets a Gaussian distribution due to detector resolution. The peak is called photopeak. If an X-ray escapes from the detector, the missing energy is undetected. The peak is termed the escape peak. The escape peak has an amplitude that depends on the energy of the photon, the material of the detector, yields of fluorescent, set up geometry out of many factors.

1.3.3 Compton scattering

When the angle of incidence of a photon of energy E = hν changes due to interaction with an electron in an atom, the scattering is called Compton scattering. In this case, the photon interacts with the electron that is assumed to be free and is at rest, unlike photoelectric effect where the photon interacts with a bound electron. The theory of quantum electrodynamics is used to calculate the differential cross-section on single electron for a solid angle dΩ and is known as Klein-Nishina formula [10].

$$\frac{d\sigma}{d\Omega} = \frac{r_e^2}{2}\left[\frac{1}{1+\epsilon(1-cos\theta)}\right]^2\left[\frac{1}{1+\epsilon(1-cos\theta)} + \epsilon(1-cos\theta) + cos^2\theta\right] \tag{1.18}$$

where r$_e$ is the Bohr radius and the photon has an energy ε = hν/m_ec^2 in units of the free electron mass. The above formula reduces to the Thomson formula when the energy of the photon is less than the rest mass energy of the electron.

$$\frac{d\sigma_{Thomson}}{d\Omega} = \frac{r_e^2}{2}(1+cos^2\theta) \tag{1.19}$$

The Thomson formula is the angular distribution of the radiation scattered elastically by a free charge as obtained using simple electromagnetism. The formula is symmetric for $\theta \leftrightarrow (\pi - \theta)$, with maxima at θ = 0 and π. The distribution is boosted in the forward direction as the energy of the photon increases also the probability of back scattering of the photons decreases. The atomic differential cross-section can be obtained by multiplying the Klein-Nishina formula by the atomic number Z because of the incoherent contributions from the electrons. When the Klein-Nishina formula of Compton cross-section is integrated over total 4π solid angle, the total cross-section is obtained. This gives the attenuation cross-section that includes the elastic and inelastic cross-sections. For the photons with highest wavelengths, the attenuation cross-section is maximum and it starts to follow Thomson cross-section where all scatterings are elastic scattering as shown in Eq. 1.20.

$$\sigma_{Thomson} = \frac{8\pi r_e^2 Z}{3} \tag{1.20}$$

The attenuation cross-section decreases due to increase of the frequency; as a result, the inelastic cross-section increases. A fit to the attenuation cross-section is given by,

$$\sigma_{Thomson} = \frac{8\pi r_e^2 Z}{3}\frac{1}{1+\frac{3\epsilon^{0.7}}{2}} \tag{1.21}$$

After losing a part of its energy, the energy of the photon changes to

$$h\nu' = \frac{h\nu}{1+\epsilon(1-cos\theta)} \tag{1.22}$$

where ν' is the frequency of the emerging photon. The corresponding change in the wavelength of the photon is given by,

$$\Delta\lambda = \lambda - \lambda' = \lambda_C(1 - cos\theta) \tag{1.23}$$

here $\lambda_C = \frac{h}{m_e c}$ is called the Compton wavelength. The energy transferred to the electron by means of collision is given by,

$$E_e = \frac{h\nu\epsilon(1 - cos\theta)}{1 + \epsilon(1 - cos\theta)} \tag{1.24}$$

As the scattering angle of the photon increases E_e increases and reach its maximum for $\theta = \pi$. The photon can not transfer all of its energy to the electron because it is forbidden from the kinematic point of view. The energy spectrum of the electron exhibits it; the spectrum starts from 0 to a maximum value then suddenly drops. The energy value where the energy falls is called the Compton edge. The Compton edge is smeared off if the binding energy of the electron is considered. In the limit of large energy of the photon, the energy gap between the Compton edge and the photon energy approaches $m_ec^2/2$.

1.3.4 Pair production

The phenomenon of pair production is the creation of a pair of electron and a positron from a photon. The photon interacts with a virtual photon from a nucleus and eventually disappears giving rise to an electron-positron pair. A medium is required for the conservation of the momentum, so pair production is not possible in the vacuum. The photon should have an energy greater than $2m_ec^2$ for the process to occur. The pair production cross-section increases with the increase of the photon energy above the threshold and reaches a plateau. At a higher energy, the pair production is the dominant process for the interaction of the photon with matter as can be seen from Fig. 1.3. The cross-section of the pair production process is related to the cross-section of Bremsstrahlung. At high energy of the photon, the cross-section can be written in terms of the radiation length as shown in Eq. 1.25.

$$\sigma_{pair} = \frac{7A}{9N_AX_0} \tag{1.25}$$

The kinetic energy of the electron-positron pair is equal to the photon energy exceeding $2m_ec^2$. This electron-positron pair will interact with the medium. The positron is annihilated with interaction with an electron inside the medium and two 511 keV photons are liberated. A single peak corresponding to the original photon will be present in the energy spectrum if the two 511 keV photons are absorbed inside the medium. If one of the photons escapes from the active medium of the detector, a peak, called missing peak, is found in the spectrum 511 keV below the original peak. A double-escape peak

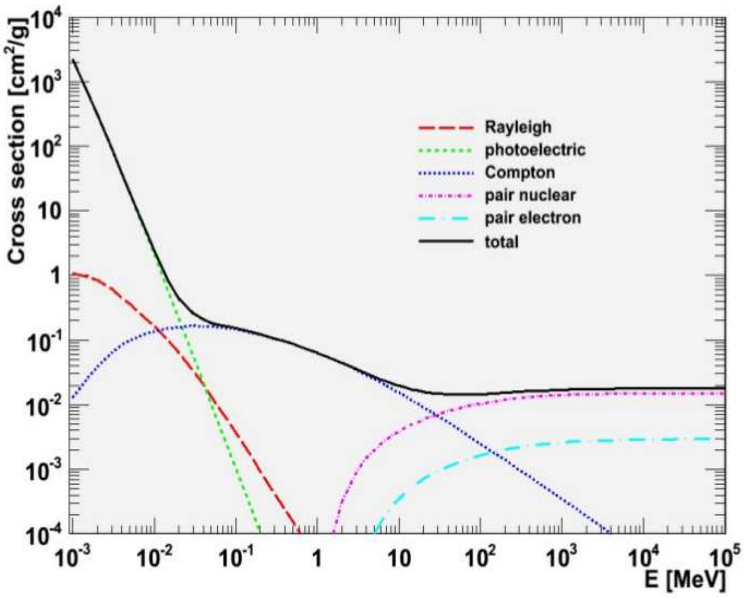

Figure 1.3: Cross section of different processes of interaction of photon with matter.

can be seen in case of escape of both the photons at 1022 keV below the full-energy peak.

1.4 Interaction of neutrons

Neutrons are uncharged particles and do not participate in Coulomb interactions with other charged particles. So they can travel large distance in matter without any interaction with the matter. The mean free path can be few millimetres to few centimetres. Neutrons can suffer elastic or inelastic collisions with the atom. They can induce nuclear reactions also. The type of interaction is decided by its energy. Depending on the energy, neutrons can be divided into two types - slow and fast neutrons. Neutrons having energy below 1 eV are called slow neutrons. The slow neutrons usually lose energy through scattering with the nuclei. A neutron with an energy of 0.025 eV, is called thermal neutron. A thermal neutron can induce a nuclear reaction. A nuclear reaction can give rise to the production of gamma rays, a proton, an alpha particle or a nuclear fission can take place. The interaction cross-section of neutron decreases as the energy increases. But the cross-section of elastic scattering becomes a dominant process. The amount of energy transfer depends on the target material. Neutron loses maximum energy in collisions with the hydrogen atom. A neutron can lose its sole energy in a single collision. Inelastic scattering is important at a higher energy where a nucleus is excited to higher energy state and eventually de-excites by emitting a photon.

1.5 Particle detectors

Particle detectors are based on the interaction of the particles with the active medium of the detector. Detectors can be broadly divided into two types based on the active medium used - i) gaseous ionisation detectors and ii) solid state detectors. In gaseous detectors, a gas or a mixture of gases, generally noble gas, are used as the active medium. The solid state detectors use solid material as the active medium like - semiconductor or plastic scintillator. The particle detectors are used to measure the energy, momentum, charge, spin and various others properties of the detected particle. To measure the momentum, the particle is allowed to pass through a magnetic field. A charged particle will experience a Lorentz force $\vec{F}$ = q.$\vec{E}$ + q.($\vec{v} \times \vec{B}$). The particle will bend due to magnetic force. The momentum of the particle is measured from the curvature of the charged particle. The information obtained from the detectors are used to make tracks of the particles and to identify the particle.

Modern particle physics experiment uses many detectors placed one after another, each of them being used for specific purposes dedicated to it. The detectors are of three main types of sub-detectors :

- Tracking detector – detects and reveals the path of a particle
- Calorimeter – stops, absorbs and measures the energy of a particle
- Particle identification detector – identifies the type of particle using various techniques

1.5.1 Tracking detector

The trajectory of a charged particle can be reconstructed by the ionsing effects on the material the particle passed through. An array of several layers of tracking detectors is placed for the purpose of tracking. Silicon based solid state pixel detectors are used as tracking detector which is placed close to the collision point for precise measurement of the track parameters. The gaseous detectors are used as the particle trackers which is normally placed after the inner trackers. The coordinates of the point interaction of the particle are recorded from the signal produced by the charged particle while passing through the tracking detectors. This coordinates are used to make the full track of the particle. Modern computer-based cellular automation technique and Kalman filter algorithm [11] is used to reconstruct the track of the particle. In case of tracking the muons, an iron absorber is used to stop the large background due to the hadrons. Muons, being a lepton, can pass through long distances inside matter. The muon chamber detector for the future Compressed Baryonic Matter (CBM) experiment will use alternative layers of absorbers and tracking detectors. A detailed description of the muon chamber for the CBM experiment at FAIR is described in Sec.3.6.2.

1.5.2 Calorimeters

When a particle passes through an absorber, it loses its energy by means of collision and produces other particles. The produced particles may also produce secondary particles, so a shower of particles can be produced as shown in Fig. 1.4. A calorimeter [12] measures the total energy deposited by a charged or a neutral particle. It is usually designed to stop the particle or absorb most of the secondary particles produced by the incoming particle. A calorimeter is made of several layers of material, usually, lead (Pb) or tungsten. There are scintillating fibres that collect the photon and are connected to the photo-multiplier tube to produce the signal. There are two types of calorimeters - hadron calorimeter and electromagnetic calorimeter. The electromagnetic calorimeter is used to measure the energy of the electrons and photons. Although the main task of the calorimeter is to measure the energy of the particle, it is also used to identify particles, to determine the position of the shower of particles and to measure the arrival time of the particles.

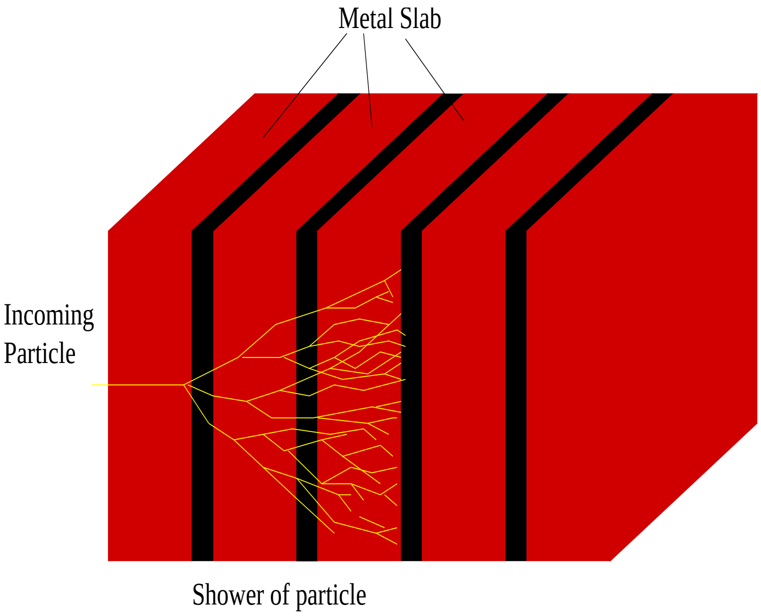

Figure 1.4: A schematic diagram of the shower of particle produced inside a calorimeter.

1.5.3 Particle identification detector

Particle identifier detector is used to identify the particle [13, 14]. To identify a particle, information of its mass is necessary. The Cherenkov detector and the transition radiation detectors are used to identify the particles. When a particle passes through a medium faster than the velocity of light in that medium, then Cherenkov radiation is emitted making an angle with the direction of the particle. So, a cone of radiation is created. The mass of the particle can be measured from the radius of curvature of the ring produced by the radiation. Transition radiation is produced when a fast charged particle passes the boundary between two electrical insulators. The energy of that transition radiation is related to the energy of the particle. Hence the particle can be identified. A particle can be identified by the time of flight detector. It can discriminate a heavy particle from a light one of same momentum using the information of their time of flight. A Time Projection Chamber (TPC) uses electric and magnetic fields inside a large sensitive volume containing a gas mixture of liquid as the active medium. The TPC is used in many experiments as the particle identifier detector, such as - A Large Hadron Collider Experiment (ALICE) at CERN, T2K experiment in Japan.

1.6 Gaseous ionisation detector

When a charged particle passes through a gas it will lose its energy by ionising the gas molecules. A gaseous ionisation detector [15] collects the charge produced in the gas. The ionisation detector is the first instrument developed for the detection of radiation. Three basic types of gaseous detectors were developed in the early 20^{th} century: the ionisation chamber, the proportional counter and the Geiger-Müller counter. This detectors were used in those days but now they are replaced by new age detectors. Only some of their applications are found as radiation monitors in laboratory. In the late 1960's, there was a breakthrough in the detector technology by inventing multi-wire proportional chamber (MWPC) [16] by Georges Charpak who was awarded the Nobel prize in 1992. The detector has a simple design and good position resolution (less than a millimetre) and was quickly accepted in many particle and nuclear physics experiments. The success of the MWPC is followed by the development of drift chamber and the time projection chamber. They work on the same basic principle of proportional counter and still are in operational in physics experiments. There are three basic types of gaseous ionisation detectors -

- Ionisation chambers
- Proportional counter
- Geiger-Müller tubes

The basic operational principle and structures are the same for the three types of detectors but they work under different operating parameters exhibiting different phenomena. The basic design of an ionisation detector consists of a container, a metallic cylinder which acts as the cathode and a thin window as shown in Fig. 1.5. An anode wire is suspended along the axis of the cylinder and a positive potential is applied relative

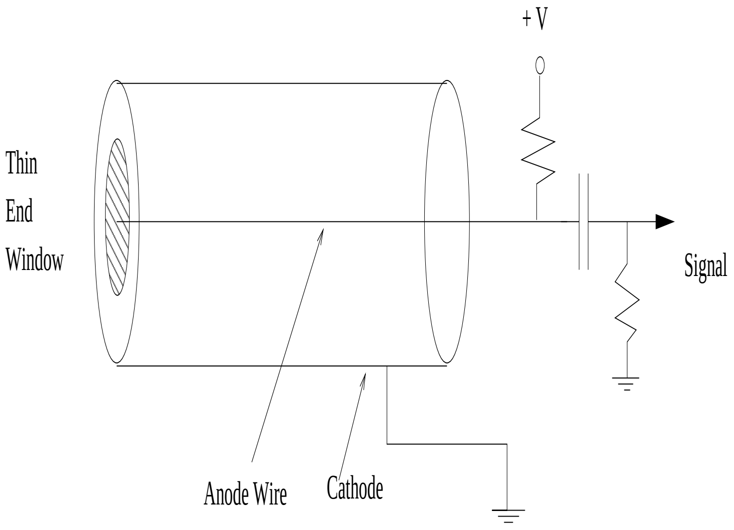

Figure 1.5: The basic structure of an ionisation chamber.

to the cathode. A noble gas or a mixture of gases is used as the active medium. The gas mixture is chosen keeping in mind the purposes of using the detector. If ’a’ is the radius of the central anode wire, ’b’ is the inner radius of the cylinder, then the radial electric field at a distance ’r’ from the axis of the cylinder is given by,

$$E(r) = \frac{V_0}{r.\ln(\frac{b}{a})} \tag{1.26}$$

Now when an energetic particle passes through the detector, it ionises the gas directly if the incident particle is charged or via secondary interactions due a neutral particle. The electrons will be accelerated towards the anode wire following the electrical field. The slowly moving heavy ions will move towards the cylindrical cathode where they will be collected. The average number of primary electrons produced by the particle is proportional to the amount of energy deposited by the particle in the active medium of the detector. The primary electrons may produce further ionisation and a signal corresponding to the charge collected at the anode will be generated. The amplitude of the signal depends on the energy deposited by the incident radiation and on the strength of the electric field. The variation of the charge collected for different values of the intensity of the electric field is illustrated in Fig.1.6. When no electric field is present inside the detector, the produced electron-ion pairs will recombine due to their electrostatic attraction. As the intensity of the electric field increases the electrons are attracted towards the anode and are collected to produce the signal. When the electric field is sufficiently large to attract all the primary electrons, the anode current due to the electrons is saturated. There is no further increase of the signal due to increase of the field intensity. The ionisation chamber is operated in this region (region - I) as indicated in Fig. 1.6.

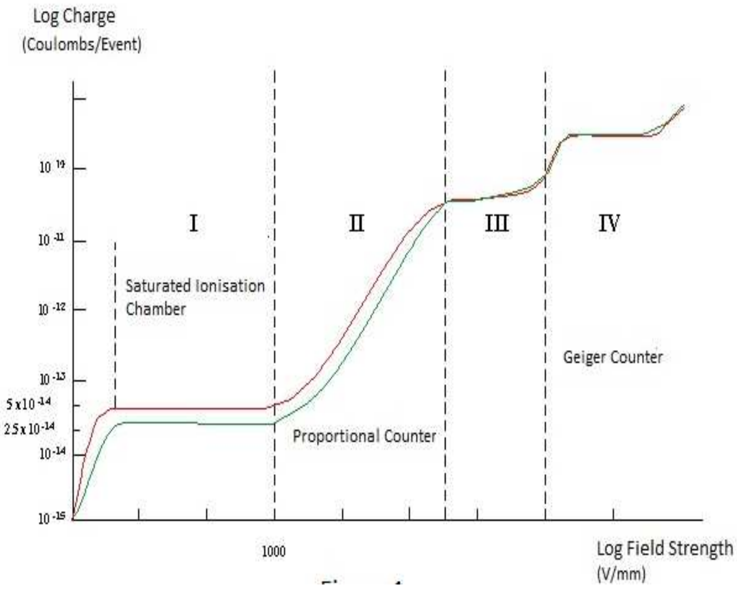

Figure 1.6: The charge collected in a basic ionisation detector with the applied voltage for α particles of mass 5 MeV (green) and 10 MeV (red).

1.6.1 Ionisation chamber

No gas multiplication occurs in the ionisation region due to low intensity of the electric field in an ionisation chamber [17]. The anode current is generated due to the primary electrons only. So the amplitude of the signal is very small and should be measured with a electrometer having low noise amplifier. The intensity of the electric field has no effect on the current. The chamber has no dead time so they are preferably used to measure the high radiation dose rate.

1.6.2 Proportional counter

When the electric field intensity is increased beyond the ionisation region, the primary electrons gain sufficient energy to ionise another gas molecule. This ionisation is called secondary ionisation. These secondary electrons can produce further ionisation if they acquire sufficient energy and so on. So an avalanche of electrons is produced and reach the anode. The electric field is stronger near the anode wire, so the avalanche occurs quickly near the wire. The avalanche collected at the anode develops a momentary voltage across the detector and a pulse is produced. The charge collected or the anode current is directly proportional to the intensity of the electric field, so the detector operated in this region is called proportional counter [18]. The multiplication factor, defined as the ratio of the total electrons collected at the anode to the number of primary electrons, can be as high as 10^7. This value is also known as the gas gain. The signal is much higher than the ionisation detector but proportional to the electric field.

1.6.3 Geiger-Müller tube [19]

An increase of the electric field beyond the region of proportionality results accumulation of space-charge around the anode wire which modifies the electric field configuration. The proportionality is then lost, this region is called the limited proportionality region. When the electric field is further increased the avalanche is so high that a discharge starts occurring in the gas. A long series of avalanches occurs along the entire length of the anode wire. The ultra-violet photons from the primary avalanche induce this chain of avalanches. The anode current is then saturated completely and independent of the electric field. Polyatomic gas, such as CO_2, CF_4 are mixed with the active gas to absorb the UV photons. The gas is called quenching gas. The current pulse is recorded by the electronics and the rate of the particles can be counted. This region of operation of the detector is called Geiger region marked as region-IV in the figure. The working voltage of the Geiger counter is chosen at the middle of the plateau.

1.7 Micro pattern gaseous detectors

The wire based gas detectors were widely used in experiments. But there are some limitations on their use. The space charge effects at high particle rate affect the electric field configuration around the anode wire. As a result, the gain of the detector decreases at a high flux of particles. Micro Pattern Gaseous Detectors (MPGDs) [20] are a class of devices that exploit microscopic structures to obtain charge amplification together with fast ion collection, therefore offering improved performance at high particle rates. Typical space resolution about few tens of microns, a time resolution of about 10 ns and a rate capability of several hundred kHz/cm^2 can be obtained from MPGDs. The MPGD family has members like - Micro-Strip Gas Chamber (MSGC), MICRO-MEsh GAseous Structure (MICROMEGAS), Gas Electron Multiplier (GEM), micro-dot chamber, micro grove chamber, Micro Hole and Strip Plate (MHSP) [21, 22] detector etc.

1.7.1 Micro-strip gas chamber

In 1988, Anton Oed introduced a novel concept in detector: the Micro-Strip Gas Chamber (MSGC) [23] which consists of a set of tiny metal strips engraved on a thin insulating support and alternatively connected as anodes and cathodes. The MSGC relies for its operation on the same processes of avalanche multiplication as the multi-wire devices. A close view of the strips is shown in Fig. 1.7.(a) and the electric field configuration is shown in Fig. 1.7.(b). The photolithography technology used for manufacturing permits to reduce the electrode spacing by at least an order of magnitude, correspondingly improving the multi-hit capability. Moreover, the fast collection of most positive ions by the nearby cathode strips reduces space charge and the rate capability is also increased. A

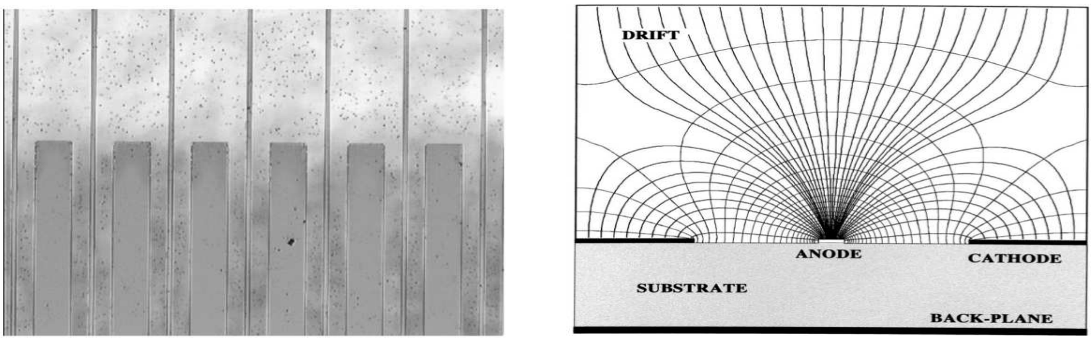

(a) (b)

Figure 1.7: (a) A close view of alternative array of cathode and anode strips in MSGC, (b) the electric field configuration in the MSGC.

substantial and successful development effort has been undertaken to improve the technology, with the development of supports preventing charge accumulations. Some problems persisted, namely the slow degradation under sustained irradiation (ageing) and the serious damages that may be produced by accidental discharges [24]. Advances in photo-lithography and micro-processing technology during the past decade triggered a major transition in the field of gas detectors from wire chambers to Micro-Pattern Gas Detector (MPGD) concepts, revolutionising cell size limitations for many gas detector applications. They have in general higher reliability and can be produced at lower cost. All of them are based on the same phenomena of ionisation of gas in proportional mode, using different configuration of the electric field which drives towards the readout pads the induced and then amplified charges. The most recent types of detectors aiming at improving spatial and time resolution, capable of economically covering large detection volume with the low mass budget are MICROMEGAS (MICRO-MEsh GAseous Structure) [25, 26] and Gas Electron Multiplier (GEM) detector [27, 28], both of which have the stability of operation in long-term basis even in an experimental environment with a high flux of particles. As a remark, the main advantage in MICROMEGAS and GEM detector is the decoupling of the gain stage from the induction stage, whereas in wire chambers the gain and the induction stage were together within a few free path length away from the wire, increasing the probability of highly energetic discharges.

1.7.2 MICROMEGAS

The MICROMEGAS [25, 26] is a gaseous detector based on a two-stage parallel-plate avalanche operation. It was developed by the CEA Saclay for the COMPASS experiment to withstand a flux up to 500 kHz/cm^2 with a spatial resolution better than 100 μm and low material budget. The detector is developed by a stretched thin metal grid keeping a small distance of 50-100 μm from the anode readout electrode as shown in Fig. 1.8.(a). A

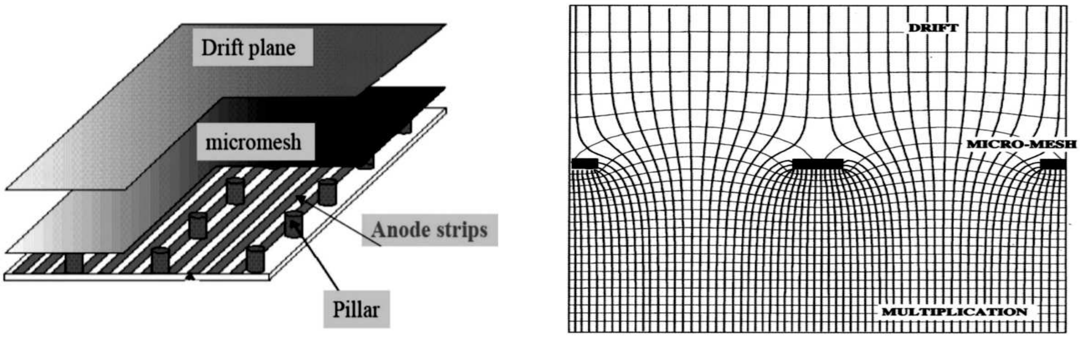

(a)

(b)

Figure 1.8: (a) The MICROMEGAS detector with the wire mesh and the spacers, (b) the electric field inside a MICROMEGAS chamber.

high electric field $\sim$ 30 kV/cm is developed across the gap by application of a high voltage (Fig. 1.8.(b)). The electrons created in the drift region are multiplied in the gap with high gains. The thin gap between the wire mesh and the anode readout electrode is maintained by inserting insulating spacers at a regular array. The anode readout printed circuit board with the readout strips is laminated with an etchable polymer foil and the metal mesh at high temperature. An insulator is masked on the anode readout. The spacer support pillars are produced by selectively removing the insulator using photolithographic process. A fast signal is induced due to the small gap and high electric field. The ions are mostly collected at the cathode mesh thus the back drifting ions are reduced. A maximum gain of 10^5 can be attained for a small amount of ionisation at least in the absence of heavily ionising environment. The MICROMEGAS detector has good position resolution for its narrow amplification gap and small readout strip pitch in low diffusion gas. A position resolution of 12 μm has been obtained in CF_4 gas with strip readout of a pitch of 100 μm [29].

1.7.3 Gas Electron Multiplier (GEM) detector

The GEM detector is a novel micro-pattern detector which has both excellent space and time resolution. Developed by F. Sauli [27, 28] the detector can be operated at high gain at relatively low operating voltage. The detector has low spark probability and is stable for long-term operation at harsh radiation environment. The rate capability of the detector is up to several MHz/cm^2. A detailed description of GEM detector will be given in the next chapter.

1.7.4 Thick GEM detector

The THick GEM (THGEM) has a hole pattern same as the GEM but the thickness of the detector plane is 5-20 times than the GEM [30]. THGEM is a very robust and cheap detector. The foils are manufactured economically by drilling mechanically followed by copper etching of the hole's rim (typically 0.1 mm) using a photolithographic mask. The typical hole diameter is 0.3-1 mm with a hole pitch of 0.7-4 mm. The thickness of the plate is about 0.4-3 mm. The rim of the hole results in an increase of the gain about 10 times higher than the foils without a rim; also the discharge probability is reduced [31]. Two or three THGEM foils can be cascaded to make a double or triple GEM for higher gain and stability.

1.7.5 Other micro-pattern detectors

The polyimide etching technology used for the GEM detector is used for the developing other micropattern gas detectors with the same readout structure. The MPGD family includes Micro Dot (MDOT) [32, 33], well detector [34], micro groove detector [35]. The MDOT detector has a central anode inside each hexagonal cathode as shown in Fig. 1.9. The diameter of the anode dots are 12-20 μm and that of the cathodes are 20-40 μm wide. The gap between the anode dot and the cathode is 75 μm for a 200 μm pitch and 35 μm for a 100 μm pitch. Large gain $\sim 10^4$-10^5 can be obtained with an MDOT of 200 μm pitch in an argon-dimethyl ether gas mixture. An energy resolution of FWFM of 19% is achieved with a 8 keV X-ray.

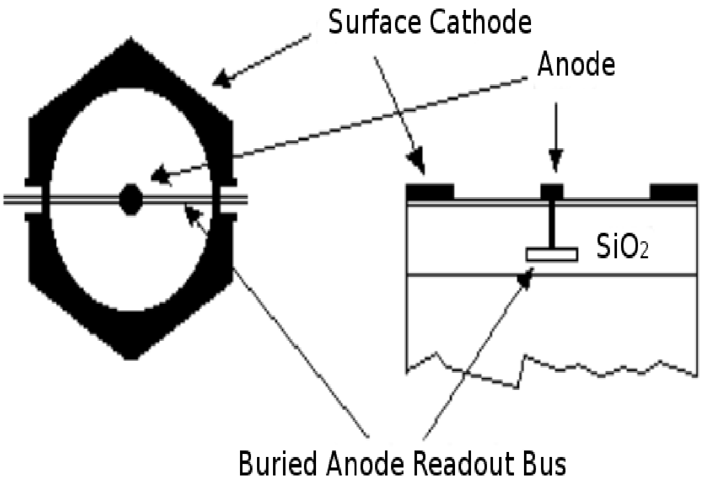

Figure 1.9: A single cell of the MDOT detector from above the detector and the cross-section.

There is no induction region in the well and micro-groove detectors. So the electrons after amplification are collected at the bottom electrode. The gain of the detector is higher than a single GEM detector because the electron avalanche is not shared between the bottom electrode and the anode. The amplification principle of GEM foil and the microstrip detector technology is combined to develop microhole [36] and strip plate detector to provide a high gain of the detector.

1.8 Summary

A charged particle creates ion-electron pairs in a gas. After amplification of the charges by the electric field, they are collected at the anode readout plate and a signal is generated. The gas detector is based on this principle. In the early days, ionisation chamber or Geiger-Müller counter were used to detect radiation. The MWPC is widely used in detecting particles produced in high energy nuclear collision experiments. Due to increase in the collision rate and energy of the heavy-ions, new detector technologies have been developed to detect the particles efficiently. To detect the signal from the rare probes, the detector should have high efficiency, excellent rate capability with excellent time and space resolution operating at relatively low voltage with small discharge probability having low material budget. Modern photolithography technique allows to design detectors with low material budget, highly efficient with large gain like - MICROMEGAS, GEM. The GEM detector is now widely used in many experiment as a tracker, triggering device, preamplifier etc. The detector can be realised in plannar, cylindrical or spherical shapes, according to the experimental requirement.

Bibliography

[1] K.A. Olive et al., (Particle Data Group), Chin. Phys. C, **38**, 090001 (2014).

[2] Y. Tsai, Reviews of Modern Physics **46** (1974) 815–851.

[3] W. T. Scott, Reviews of Modern Physics **35** (1963) 231–313.

[4] G. R. Lynch, et. al., Nucl. Instr. Meth. B **58** (1991) 6–10.

[5] F. M. Penning, The Science of Nature **15** (1927) 818.

[6] J. S. Townsend, Nature **62** (1900) 340.

[7] H. Raether, Electron avalanches and breakdown in gases, Butterworths advanced physics series:

[8] C. M. Davisson, Interaction of γ-RADIATION with Matter - Alpha, Beta and Gamma-ray Spectroscopy, ed. by K. Siegbahn, North-Holland Publishing Company, 1965

[9] The Theory of Auger Transitions, D. Chattarji, Academic Press, London, 1976

[10] O. Klein and T. Nishina, Zeitschrift für Physik A Hadrons and Nuclei **52** (1929) 853–868.

[11] R. Kalman, Transactions of the ASME - Journal of Basic Engineering Series D **82** (1960) 35.

[12] C. W. Fabjan, Ann. Rev. Nucl. Part. Sci. **32** (1982) 335-389.

[13] J. Va'vra, Nucl. Instr. Meth. A **453** (2000) 262.

[14] Christian Lippmann, arXiv:1101.3276v4 [hep-ex]

[15] C. Grupen et al., Particle Detectors, Cambridge University Press, Newyork, 2008.

[16] G. Charpak et al., Nucl. Instr. Meth. A **62** (1968) 262.

[17] Glenn F. Knoll, Radiation Detection and Measurement, Wiley, USA, 2010.

[18] E. Rutherford, H. Geiger, Proc. Royal Soc. A 81 (1908) 141.

[19] H. Geiger and W. Müller, Das Elektronenzählrohr. Phys. Zeits. 29 (1928) 839.

[20] F. sauli et al., Annu. Rev. Nucl. Part. Sci. **49** (1999) 341–88.

[21] J. Veloso, et. al., Rev. Sci. Instr. **71** (2000) 2371-76.

[22] J. Maia, et. al., Nucl. Instr. Meth. A **504** (2003) 364-368.

[23] A. Oed, Nucl. Instr. Meth. A **263** (1988) 351.

[24] R. Bouclier et al., Nucl. Instr. Meth. A **365** (1995) 65.

[25] I. Giomataris et al., Nucl. Instr. Meth. A **376** (1996) 29.

[26] I. Giomataris et al., Nucl. Instr. Meth. A **560** (2006) 405.

[27] F. Sauli et al., Nucl. Instr. Meth. A **386** (1997) 531.

[28] F. Sauli et al., Nucl. Instr. Meth. A **805** (2016) 2-25.

[29] D. Jerré et al., Nucl. Instr. Meth. A **459** (2001) 523-526.

[30] R. Chechik et al., Nucl. Instr. Meth. A **535** (2004) 303.

[31] C. Shalem et al., Nucl. Instr. Meth. A **558** (2006) 475.

[32] S. Baigi et al., Nucl. Instr. Meth. A **361** (1995) 72-78.

[33] H. S. Cho et al., Nucl. Instr. Meth. A **422** (1999) 296-299.

[34] R. Bellazzini et al., Nucl. Instr. Meth. A **423** (1999) 125.

[35] R. Bellazzini et al., Nucl. Instr. Meth. A **424** (1999) 444-458.

[36] J. F. C. A. Veloso et al., Review of Scientific Instruments, **71** (2000) 2371–2376.

Chapter 2

Gas Electron Multiplier (GEM) Detector

There has been tremendous advancement in the area of high energy heavy-ion collision experiments in the last few decades. The energy of the heavy-ions has been increased after successful operation of the powerful accelerators at extreme energies up to several TeV per nucleon. For example, the Large Hadron Collider (LHC) is colliding p + p beams at an energy of 13 TeV per nucleon. The detectors used in this experiments are also developed keeping in mind the essential requirements of the experiment. The major development started with G. Charpak in 1968 in inventing Multi Wire Proportional Chamber (MWPC) [1]. The MWPC consists of a grid of thin and parallel wires fixed between two cathode planes. A multiplication of electron is created by a charged particle in the gas on application of suitable voltage. MWPC is being used in many experiments for collection of electrons or the measurement of its drift time to the anode readout plane. Despite their wide range of application, the MWPC is limited in use due to their low rate handling capacity. The gain and efficiency of MWPC start to decrease for particle rate above 10^4 Hz/mm^2. The thin wire spacing and deposition of thin insulating coating of polymer on the wire is itself a limitation. Some of the limitations of MWPC are overcame by the Micro-Strip Gas Counter (MSGC), developed by Anton Oed [2]. The MSGC is a gaseous detector with thin parallel metallic strips connected to the anode and cathode alternatively. The rate capability of MSGC is two orders of magnitude higher than that of MWPC whereas the gain is 10 times higher. But the MSGC has a problem of formation of streamers or even discharges that can damage the detector. The Gas Electron Multiplier (GEM) detector is a novel detector that can handle higher flux of particles and is less prone to discharges.

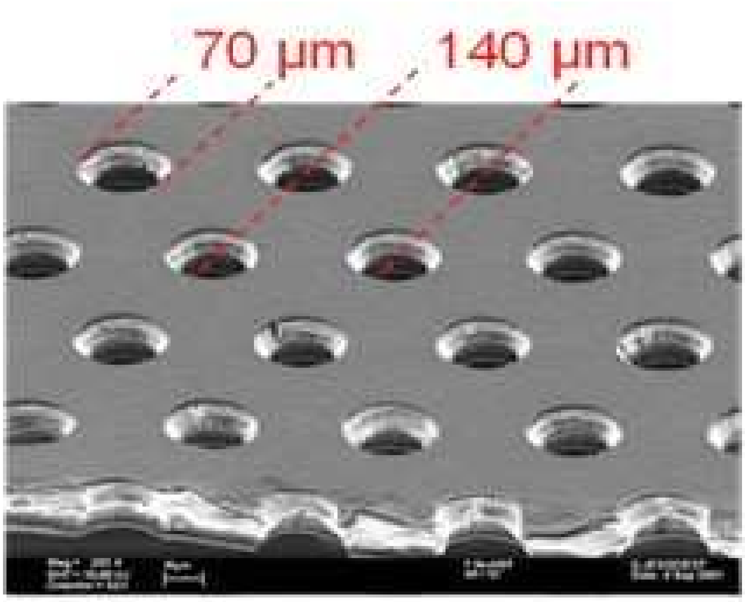

Figure 2.1: Picture of a GEM foil with electron microscope. There are holes of diameter 70 μm with a pitch of 140 μm.

2.1 GEM foil

A GEM foil is a thin polymer foil (kapton [3]) with copper cladding on both sides. The kapton polymer has a thickness of 50 μm and the copper cladding is 5 μm thin. The foil is pierced with a high density of holes. The density of the holes is about 50-100 per cm^2. The diameter of the hole varies from 50-100 μm and the pitch of the holes may be 100-280 μm depending on the requirement of the experiment. The gain of the detector decreases with the increase of the diameter of the hole. A standard GEM foil developed at CERN has holes having a diameter of 70 μm on the copper side and 50 μm on the kapton with a pitch of 140 μm as shown in Fig. 2.1.

2.1.1 Production of GEM foil : Double-mask and single-mask foil

The GEM foil has holes on it. Depending on the techniques of etching of the holes the foils are of two kinds - double-mask and single-mask foil. In the beginning double mask, high-quality wet etching technique was used for production of GEM foils. In the case of double mask foil, masking and etching are done from top and bottom sides of the foil. The steps are described in Fig. 2.2.(a). First, a photo-resist film of thickness 15 μm is laminated on both sides of the metal coated polymer sheet. The hole pattern is transferred from photo-lithographic masks to the photo-resist by exposure to Ultra-Violet (UV) light. Both photo-resist layers have to be patterned and careful mask alignment is needed to ensure good pattern matching. The required alignment accuracy depends on the hole diameter and size of the foil, and it should be kept below 10 μm for a good

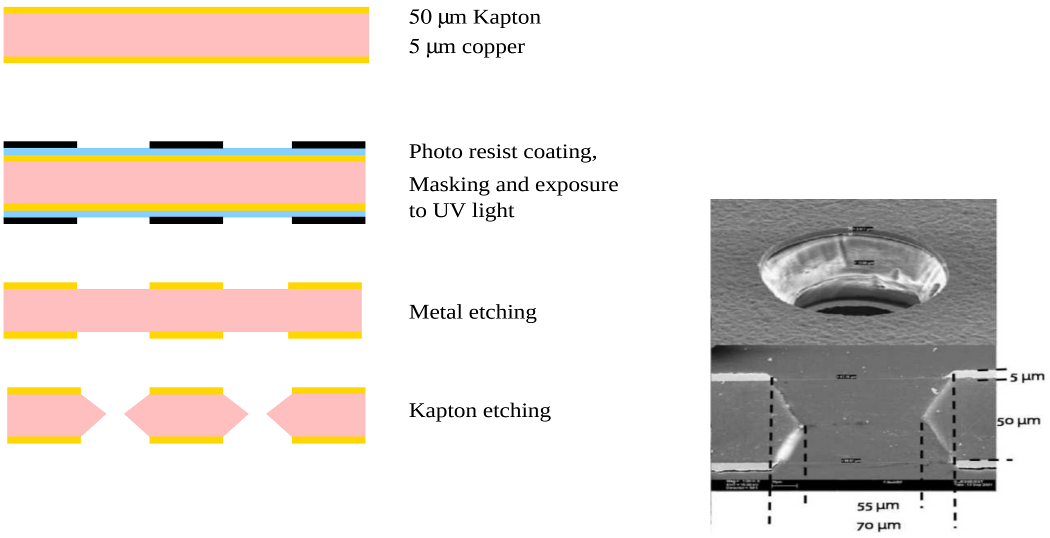

(a) (b)

Figure 2.2: (a) Double-mask GEM production procedures, (b) Bi-conical hole in double-mask GEM foil.

quality of the detector. The copper is etched by ferric chloride ($FeCl_3$) solution followed by the hydrochloride acid. Next, the kapton is etched. Since the kapton is etched from both sides of the base plane, the shape of the hole is bi-conical as shown in Fig. 2.2.(b). The production of double mask GEM is restricted for the production of large GEM due to the difficulty of alignment of the hole pattern. When the length of the GEM foil exceed 30 cm, double-mask technology is not feasible at all. Using the single-mask technique GEM foil of an area of 2 m^2 can be produced [4, 5]. The steps of the single-mask technique are shown in Fig. 2.3. In this case the GEM mask is transferred only to one side of the base plane, thus removing the need for alignment. After masking and UV light exposure, the metal is etched followed by polyimide etching. The polyimide is further etched chemically up to the bottom side. The second polyimide etching makes the holes quasi-conical [6]. The shape of the hole plays an important role in determining the characteristics of the detector. In the case of a cylindrical hole, high gain can be achieved, but it is prone to discharge at a high gain operation of the detector. The gain of GEM foil with biconical holes increases slowly at first due to charging up of the kapton. A comparison of the relative gain of the GEM foils with different kinds of hole geometries is presented in [7]. Many other techniques for the production of GEM foil have been developed, such as- plasma cooling [8], laser drilling [9], mechanical drilling for the manufacture of thick or Large Electron Multiplier (LEM) [10].

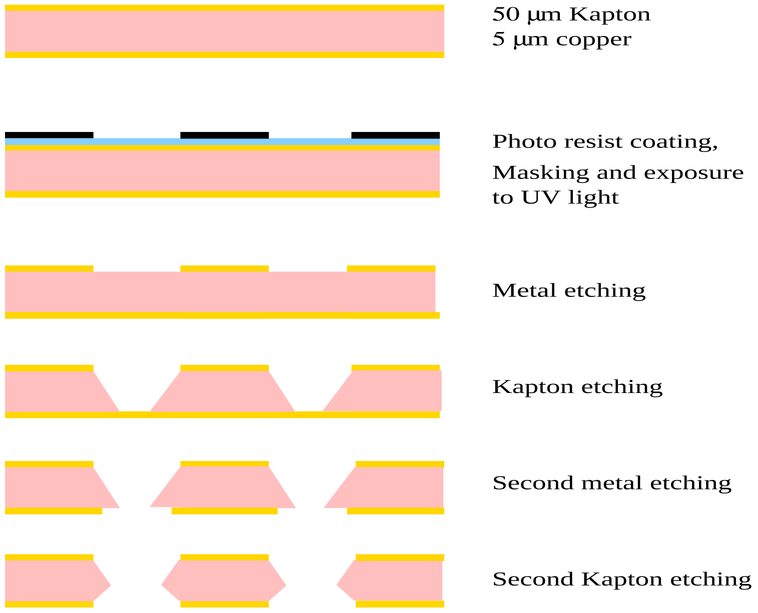

Figure 2.3: The different steps for producing single-mask GEM foil.

2.1.2 GEM detector

A single GEM foil has a gain of 100 at a voltage of about 400 V across the foil [11]. The GEM foil has an extra advantage that they can be operated in cascade. Two, three, four even five GEM foils can be stacked to make double, triple, quadruple [12, 13] and quintuple GEM [14, 15] respectively. One GEM foil is placed on top of another keeping a gap between two foils. The gap between two foils is called transfer gap. The gap between the cathode plane and the first foil is called the drift gap. A kapton plane with one side coated with copper act as the cathode or drift plane. The typical thickness of the drift plane is about 3 mm. The anode readout plane is a PCB of typical thickness of 2.5-3 mm. The readout anode plane can be X, Y strips or rectangular readout pads. The geometry of the readout can be chosen at will. The typical drift gap for the GEM detector is 3 mm. The gap between the last foil and the readout plane is called the induction gap. The widths of the gaps are optimised for experiment specific operation of the detector. In case of triple GEM detector for the operation in CBM experiment, the typical gap parameters are the following: drift gap of 3 mm, two transfer gaps of 1 mm and induction gap of 1.5 mm. A schematic of a triple GEM detector is shown in Fig. 2.4.

2.1.3 Stretching of the GEM foil

In order to maintain uniformity of the gaps, the surface of the GEM foil should be taut as far as possible. The foils are stretched to make the surface taut. The gap between the foils should remain undisturbed due to the electromagnetic attraction between the planes. The gap is maintained by using a spacer between the GEM foils or using a thin cross rib between the foils for the case of a large GEM. For small GEM foils (10 cm × 10 cm),

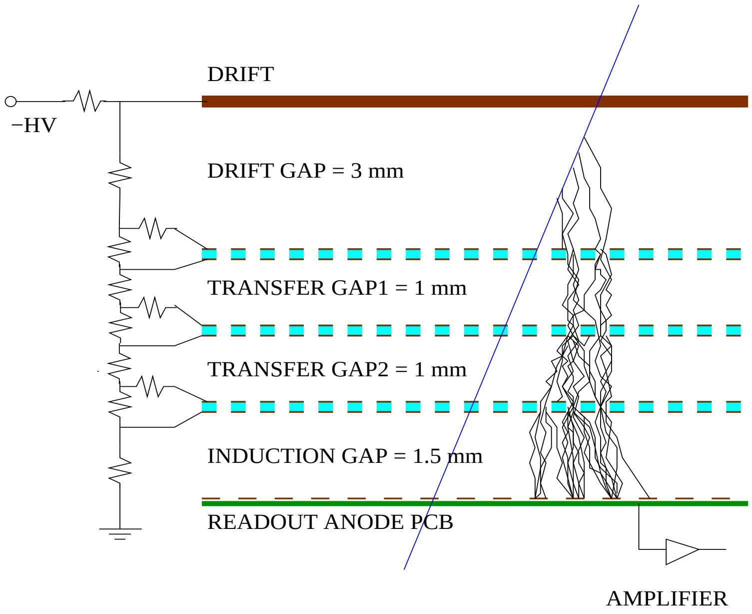

Figure 2.4: Schematic of a triple GEM detector with drift gap of 3 mm, two transfer gap of 1 mm each and an induction gap of 1.5 mm.

the base foil is stretched mechanically from all sides using a jig and a frame is glued into the stretched foil. For large size GEM foils, the foils are stretched by thermal stretching [16, 17] or mechanical stretching [18, 19].

2.1.4 Fill gas for GEM

The chemical properties of the gas play a crucial role in the operation of any gas detector. Theoretically, any gas mixture can be used as the active medium inside the detector. But experiment specific operations such as- low working voltage, high gain operation, low discharge probability, high rate capability, long-term operation etc., restrict the choice of the gas mixture. Usually, a mixture of two or more gases is used inside the detector. The ratio of the gases in the mixture is optimised to the requirement of the experiment. Avalanche multiplication of electrons occurs in noble gas at relatively low voltages than in other gases. So noble gas is the main component that takes care of the electron multiplication and is called the counting gas. But with pure noble gas, the discharge probability increases because the molecules of the gas can only return to the ground state through radiative emission. For this reason, a small amount of heavy, polyatomic gas such as CO_2 is used as quencher which can dissipate a considerable amount of energy, because they can have radiationless transitions into their excited vibrational and rotational modes. Combined in suitable proportions, these two types of gases permit an effective, stable operation of the detector. For GEM detector, Ar:CO_2 is a standard choice for its non-flammability and chemical stability. The mixture, mixed in 70:30 ratio, has a moderate resolution for relatively small drift velocity of electrons. The time resolution of the de-

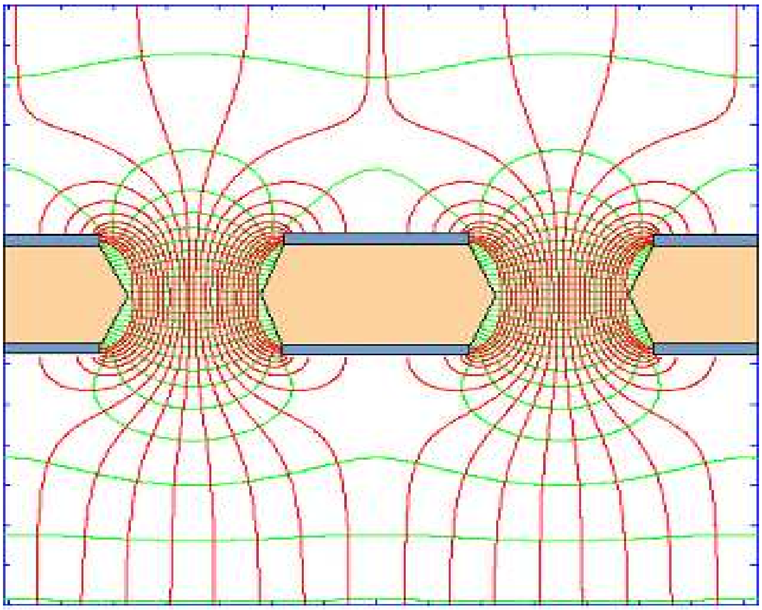

Figure 2.5: The electric field lines and equipotential surfaces inside hole of a GEM foil.

tector with Ar:CO_2 is about 10 nsec. The resolution is even better for gas mixture with added CF_4. But the use of CF_4 requires special precautions due to its chemical reactivity of fluorinated compounds created during the avalanches in presence of moisture [20].

2.1.5 Working principle of GEM detector

Like other gas detectors, detection of particles by GEM detector is based on the ionisation of the gas by the incoming charged particle. When suitable voltages are applied across the GEM foils, a high electric field is created inside the hole. As the thickness of the foils is small, an electric field about 80 kV/cm is created inside the hole due to a voltage difference of 400 V across the GEM foil. A schematic diagram of the electric field created inside the hole of a GEM foil is shown in Fig. 2.5. The GEM detector works in the proportional region. When a charged particle passes through the detector, it ionises the gas and electron-ion pairs are created inside the drift region. The electrons are called primary electrons. The typical electric field inside the drift region is 2-4 kV/cm. The electrons are drifted toward the GEM holes following the field lines. Due to the high electric field inside the hole, the primary electrons experience ionising collisions thereby resulting in an multiplication of electrons, that depend on the dipole field inside the hole. After multiplication of the primary electrons inside the hole in the first GEM foil, the electrons are transferred to the next GEM foil and further multiplication occurs again inside the holes. As the electrons have greater mobility than the ions, the avalanche has the shape of a liquid drop with the electrons grouped near the head and the slower ions trailing behind, like shown in Fig. 2.6. Thus an avalanche of the electron is collected at the readout anode plane. The anode current can be measured by a pico-ammeter. The

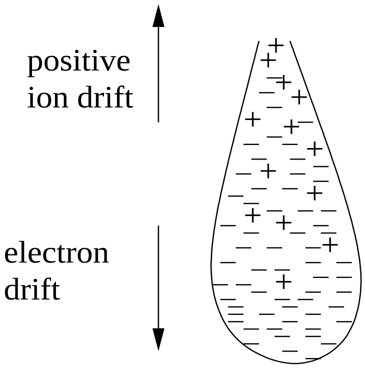

Figure 2.6: The avalanche has a shape of a liquid drop, the electrons drift toward the anode and the heavy ions slowly drift towards the cathode.

charge is allowed to pass through the pre-amplifier followed by an amplifier to get a signal corresponding to the charged particle in the oscilloscope. A block diagram of the setup is shown in Fig. 2.7. The positively charged ions created due to ionisation are slow and most of them are collected at the top copper plane. Thus a (negative) signal is generated at the anode plane due to the avalanche of electron without any contribution from the slowly moving positively charged ions. So the detector is practically free from the space charge effect and becomes potentially fast. The number of primary electrons created inside the drift gap depends on the ionisation potential of the gas mixture. For Ar:CO_2 gas mixture mixed in 70:30 ratio, the number of primary electrons for the minimum ionising particle is 30. A full list of number of primary electrons created in different gas mixtures are reported in [25]. The gain of the detector is defined as the ratio of the charge of the primary electrons to the charge collected at the anode. The noticeable advantage of multiple GEM foils structure is that the overall gain needed for operation of the detector can be attained with each of the GEM electrodes operated at a much lower voltage, therefore much less prone to discharges. The GEM detector can be used as an energy trigger by measuring the equal and opposite charges on the bottom electrode for the detection and localisation of an event due to radiation from neutral sources.

2.1.6 Positive ion backflow

The positively charged ions created in the amplification region during the ionisation of the gas have low drift velocity and they slowly move towards the drift volume. These back drifting ions will modify the electric field and consequently modify the drift field.

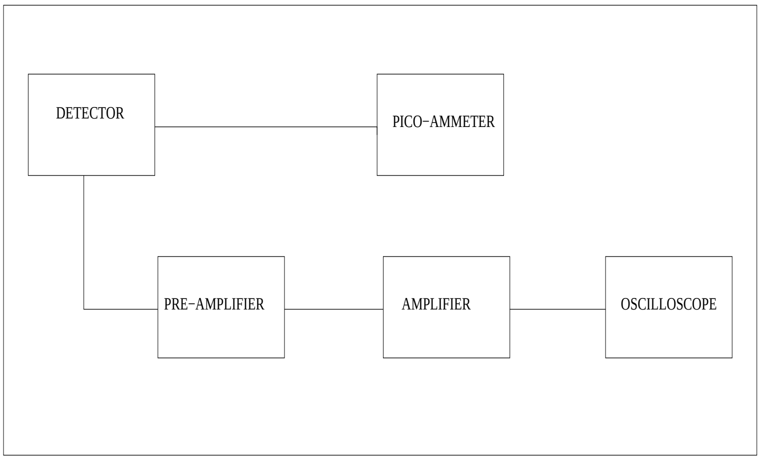

Figure 2.7: The block diagram of the setup to view signal in the oscilloscope. The current due to avalanche can be measured by a pico-ammeter. To detect the signal the raw signal is allowed to pass through a charge sensitive pre-amplifier followed by an amplifier to view a signal on the oscilloscope or fed to an MCA for energy spectroscopy.

Most of the detectors suffer a loss of gain due to these back drifting ions particularly when the flux of incoming particle is increased. Thus those detectors fail to qualify for their use in heavy-ion collision experiments with a high flux of particles. The Ion Back Flow (IBF) is defined as the ratio of the cathode current to the anode readout current.

The net amount of charge accumulated inside the drift volume depends on the rate and momentum distribution of the incident charged particles, the properties of the gas mixture, and the amount of ions from the avalanche region drifting back into the drift region. As the rate of the incoming particle increases the ion backflow increases. The minimization of ion backflow is, therefore, a prerequisite for keeping the ion feedback at the lowest possible level. In case of a MWPC the space charge due to positively charged ions affects the gain of the detector. The gain of MWPC starts to decrease sharply on and above a particle flux of 10^4 Hz/mm^2 as shown in Fig. 2.8. This restricts MWPC for their operation in a high flux of particles. The use of a grating grid operated at alternative voltage can block the ions to enter the drift region to reduce the back drifting ions. But the use of a gating grid limits the rate handling capacity [22, 23]. A substantial part of the ions are captured on the top plane of the GEM foils in a multi-GEM structure and the IBF is drastically reduced. The variation of IBF with gain for a triple GEM is shown in Fig. 2.9 using different gas mixtures at different drift fields. The ion backflow is practically independent of the gas mixture and the pressure [24]. IBF is mainly sensitive to the drift field and increases linearly with it. So gas mixtures providing good performance at low field such as Ar/CH$_4$ is the best choice to reduce IBF. As the gain increases IBF decreases. Also, it depends on the pitch of the GEM holes. A combination of the standard pitch (140 μm) and large pitch (280 μm) GEM foils will be used to reduce the ion feedback in a quadrupole GEM detector in ALICE TPC. They will use a combination of two

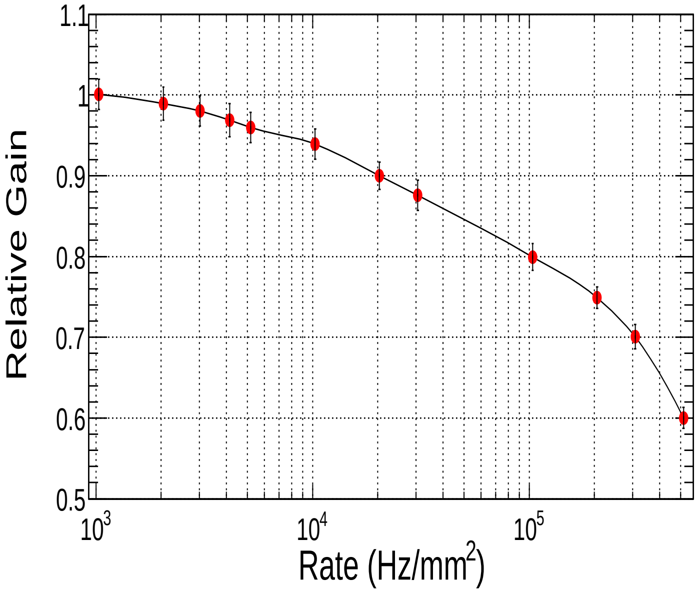

Figure 2.8: The gain of MWPC drops down sharply due to space charge effect of ions at high rate of particles.

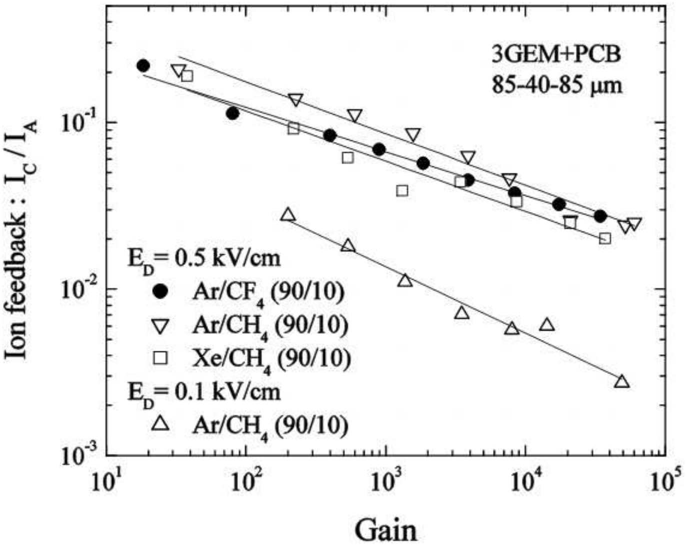

Figure 2.9: Correlation of ion backflow with energy resolution using 5.9 keV X-ray source in a quadruple S-LP-LP-S GEM in Ne:CO$_2$:N$_2$ (90:10:5) for various settings of voltage across 2^{nd} GEM foil. The voltage on 1^{st} GEM foil increases for a given setting between 225 and 315 V from left to right. The voltages on 3^{rd} and 4^{th} GEM foils are adjusted to achieve a total effective gain of 2000, while keeping their ratio fixed. The three transfer fields and the induction field are 4, 2, 0.1 and 4 kV/cm respectively.

GEM foils of standard pitch (S) and two foils with large pitch (LP). The combination abbreviated as S-LP-LP-S with Ne:CO_2:N_2 in 90:10:5 ratio is chosen to operate GEM based TPC at a gain of 2000 with IBF about 0.7 % and an energy resolution of $\sim 12\%$ at 5.9 keV X-ray [25].

2.1.7 Spark probability

When the number of electron-ion pairs exceeds a critical value, called Raether's limit [26], the electric field in front of and behind the primary avalanche is enhanced and it induces fast growth of a filament-like streamer followed by breakdown. Sometimes there might be permanent damages. Depending on the detector type and gas mixture the Q_{crit} is about 10^7-10^8 electron-ion pairs. The detector is practically dead until the spark is completely collected at the copper plane. The spark in the detector is characterised by the abrupt increase of anode current or the absence of signal. The absence of signal is reflected in the sharp decrease of count rate of the signal. In the laboratory, the discharge probability can be measured using X-ray source, neutron beam or hadron beam having a high flux of particles. The spark probability of a triple GEM detector with Ar:CO_2 70:30 ratio has been found to be negligible (about 10^{-7} at a gain of 5×10^4) [27, 28, 29].

2.1.8 Radiation hardness

Many GEM based detectors have to work in a harsh radiation environment of high flux of neutrons, so the detector needs to be radiation hard. Radiation hardness of a prototype triple GEM detector has been tested for the CBM experiment [30]. As per FLUKA [31] calculations, the estimated neutron dose at the 1^{st} detector station of muon chamber detector will reach of the order of 10^{12} n_{eq}/cm^2/year [35]. The experimental arrangement for testing radiation hardness is shown in Fig. 2.10.(a). A 40 MeV α beam is falling on a

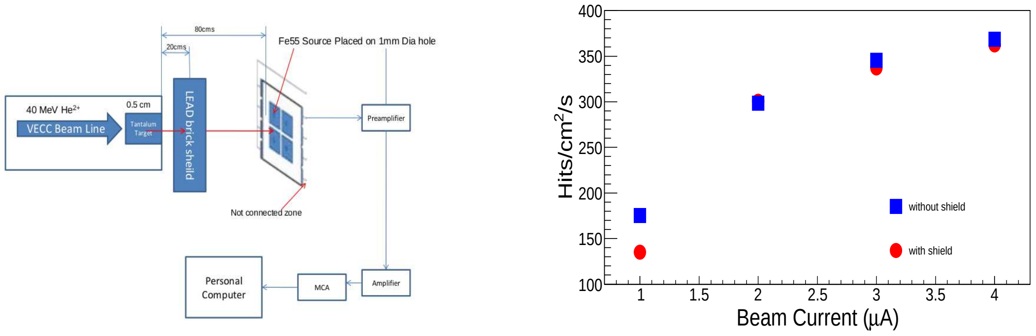

(a) (b)

Figure 2.10: (a) Experimental setup for radiation hardness test, (b) Variation of the hits with the beam current.

0.5 cm tantalum target, producing a large number of neutrons and gamma. A lead shield of 30 cm is placed after the target to screen the gamma particles. A 10 cm × 10 cm triple GEM detector is placed about 80 cm away from the tantalum target. The ΔV_{GEM} across all the GEM foils are kept at 340 V. A premixed gas of Ar:CO_2 is used inside the chamber. The signal from the detector is connected to standard NIM electronics and next fed to a MCA. The response of the detector for different beam currents corresponding to different neutron intensities is studied with and without the lead shield. The neutron flux is measured with a Boron tri-Fluoride (BF_3) neutron detector for beam current of 50-500 nA. The highest neutron flux is 10^5/cm^2/s for a beam current of 4 μA. The number of hits in the GEM detector due to neutron is shown in Fig. 2.10.(b). For the highest neutron flux of 10^5/cm^2/s, there are about 350 hits/cm^2/s in the detector [30]. This indicates that the number of hits due to background neutrons is not significant in the CBM experiment where the maximum hit density at the first GEM detector station will reach 0.4 MHz/cm^2 for Au + Au collision at a E_{lab} = 25 AGeV [35]. So these background hits will not affect the reconstruction of the tracks of the particles in the muon chamber detector of CBM experiment.

2.2 Application of GEM detector

As the accelerator technologies are being developed to deliver a beam of extremely high energy about several TeV per nucleon, the detector technology has to be developed to handle the high flux of particles in a heavy-ion collision experiment. The conventional detectors such as MWPC, are not capable of handling such a high rate of particles. The GEM detector is capable of handling high rate of particles up to several MHz/cm^2. Also the GEM detector has excellent time and space resolution. So they are being used in many experiments, such as at HERA-B as a preamplifier above the MSGC [33] and at LHC-b as a triggering device [34]. The GEM detectors are widely used as a tracker detector at COMPASS [35], TOTEM [36, 37], CMS [38, 39, 40], ILC [41, 42], NA61 [43, 44], KLEO [45, 46], PHENIX [47], STAR [48] experiments. The ALICE experiment will replace MWPC of its time projection chamber by the quadruple GEM detector after Long Shutdown-II (LS-II) to handle the event rate of 50 kHz in Pb + Pb collisions [49, 25, 50]. The CBM experiment at FAIR will use triple GEM detector for the construction of the muon chamber detector to handle high flux of particles.

2.3 Summary

Invented by F. Sauli in 1996, the GEM is a widely used technology to build gaseous detectors in the field of experimental high-energy and nuclear physics. The GEM detector has excellent position and time resolution so that it can be used as a tracker as well as triggering device. The detector can be operated at a relatively low voltage for high efficiency ($<$98%) and moderate gain, so the discharge probability is also small. The detector can sustain in a harsh radiation environment and the performance of the detector is stable for long-term operation. The rate handling capability of the detector is about 3 MHz/cm^2. Considering these facts and figures GEM based detectors are not only being used in several ongoing experiments, it will also be used for future experiments such as CBM at FAIR.

Bibliography

[1] G. Charpak et al., Nucl. Instr. Meth. A **62** (1968) 262.

[2] A. Oed, Nucl. Instr. Meth. A **263** (1988) 351.

[3] DuPont, Kapton Polyimide films.

[4] M. Villa et al., Nucl. Instr. Meth. A **628** (2011) 182.

[5] F. Mammoliti et al., EPJ Web of Conferences **96** (2015) 01023.

[6] M. Alfonsi et al., Nucl. Instr. Meth. A **617** (2010) 151.

[7] J. Benlloch et al., Nucl. Instr. Meth. A **419** (1998) 410.

[8] M. Inuzuka et al., Nucl. Instr. Meth. A **525** (2004) 529.

[9] T. Tamagawa et al., Nucl. Instr. Meth. A **560** (2006) 418.

[10] A. Badertscher et al., Nucl. Instr. Meth. A **617** (2010) 188.

[11] A. Bondar et al., Nucl. Instr. Meth. A **556** (2006) 495-497.

[12] C. Buttner et al., Nucl. Instr. Meth. A **409** (1998) 79.

[13] A. Bressan et al., Nucl. Instr. Meth. A **425** (1999) 262.

[14] A. Bondar et al., Nucl. Instr. Meth. A **496** (2003) 325.

[15] K. Dehmelt et al., IEEE Transction on Nuclear Science **62** (2015) 6, arXiv:1501.03530v3, [physics.ins-det].

[16] Thesis by Bryant Joseph Benson.

[17] RD51-Note-2011-004.

[18] L. Franconi et al., Status of no-stretch no-spacer GEM assembly, the NS2 technique method and experiment result, 2012.

[19] You Wen-Hao et al., arXiv:1405.1872 [physics.ins-det].

[20] M. Alfonsi et al., IEEE Transactions on Nuclear Science NS52 (2005) 2872.

[21] Y. Assran, A. Sharma, arXiv:1110.6761 [physics.ins-det].

[22] M. Ball et al., JINST **9** (2014) C04025.

[23] P. Graos et al., JINST **8** (201) C11023.

[24] A. Bondar et al., arXiv:physics/0208017v1.

[25] ALICE Collaboration, Technical Design Report for the Upgrade of ALICE Time Projection Chamber.

[26] H. Raether, Electron avalanches and breakdown in gases, Butterworths advanced physics series, 1964.

[27] S. Bachmann et al., Nucl. Instr. Meth. A **479** (2002) 294.

[28] G. Croci et al., Nucl. Instr. Meth. A **712** (2013) 108-112.

[29] S. Biswas et al., Nucl. Instr. Meth. A **800** (2015) 93-97.

[30] A. K. Dubey et al., Proceedings of DAE Symp. on Nucl. Physics **58** (2013).

[31] A. Ferrari et al., CERN-2005-010, SLAC-R-773, INFN-TC-05-11.

[32] Technical Design Report for the CBM Muon Chambers (2015) GSI, Darmstadt.

[33] T. Zeuner, Nucl. Instr. Meth. A **446** (2000)324-330.

[34] M. Alfonsi et al., IEEE Transactions on Nuclear Science **53** (2006) 1.

[35] C. Altunbas et al., Nucl. Instr. Meth. A **490** (2002) 177–203.

[36] T. Hilden, JINST 4 P11020 (2009).

[37] S. Lami, Nucl. Phys. B **172** (2007) 231-233.

[38] I. Vai, Nucl. Instr. Meth. A **824** (2016) 586-588.

[39] C. Calabari, Nucl. and Part. Phys. Proceedings **273–275** (2016) 1042–1047.

[40] CMS Collaboration, Technical Design Report for the CMS Endcap GEM Upgrade.

[41] D. Tsionou et al., Nucl. Instr. Meth. A **845** (2017) 309-312.

[42] A. Munnich et al., IEEE Transactions on Nuclear Science **N17** (2005) 929-931.

[43] The NA61 Collaboration, CERN.

[44] http://gdd.web.cern.ch/GDD/cylindrical.html.

[45] P. Franzini, Ann. Rev. Nucl. Part. Sci., **56** (2006) 207-251.

[46] A. Balla, Physics Procedia, **37** (2012) 522–529.

[47] W. Anderson et al., Nucl. Instr. Meth. A **646** (2011) 35-58.

[48] F. Simon et al., arxiv:0811.2432v1 [physics.ins-det].

[49] F. Reidt et al., arxiv:1411:1802v2 [physics.ins-det].

[50] B. Ketzer, Nucl. Instr. Meth. A **732** (2013) 237-240.

Chapter 3

The CBM experiment at FAIR

The heavy-ion experiments are devoted to the study of the phase diagram of the strongly interacting nuclear matter. Several theoretical and experimental studies have been done or are continuing to explore the phase diagram of the strongly interacting matter. The phase diagram of the strongly interacting nuclear matter is shown in Fig. 3.1 in a temperature versus net baryon density diagram. The theory of strong interaction, Quantum Chromo Dynamics (QCD) predicts that at the extremely high temperature or at extremely high baryon density the hadrons are deconfined into their constituent quarks. At low net baryon density, when the baryon and anti-baryon are almost equal in number, QCD predicts a temperature of about 160 MeV [1, 2] above which hadrons are melted into quarks and gluons. The inverse process of confinement of the quarks and gluons into hadrons occurred after few microseconds during the big-bang. The deconfined state of strongly interacting quarks and gluons is called Quark-Gluon-Plasma (QGP). Heavy ion collision experiments at extremely high collider energies those are available at Large Hadron Collider (LHC), the hadronic matter dissolve into quark matter at extremely high temperature and zero net baryon density. The lattice QCD calculations simulation shows that this transition from hadronic matter to QGP at extremely high temperature and zero net baryon density is a smooth crossover with out any critical point [3]. At moderate temperatures and densities, the transition of hadronic phase to quarkonium phase is believed to be a first order phase transition followed by a critical endpoint where first order phase transition ceases to exist [4, 5, 6]. At a relatively larger value of net baryon density at low temperature, there is a region where the two phases co-exist. A new phase of so-called quarkyonic matter has also been proposed to exist beyond the first order phase transition at moderate temperatures and at large net baryon density [7]. The density at the interior of the neutron star at very low temperature is about several times the normal nuclear density. At extremely high density correlated quark-quark pairs are believed to be created in the colour superconducting phase [8, 9, 10]. The phase diagram at finite net baryon density in the moderate temperature region is of prime interest because one can study the characteristic of the transition of phase from hadronic matter to quark-gluon-plasma, the position of the critical point, chiral symmetry restoration etc.. Many heavy-ion collision

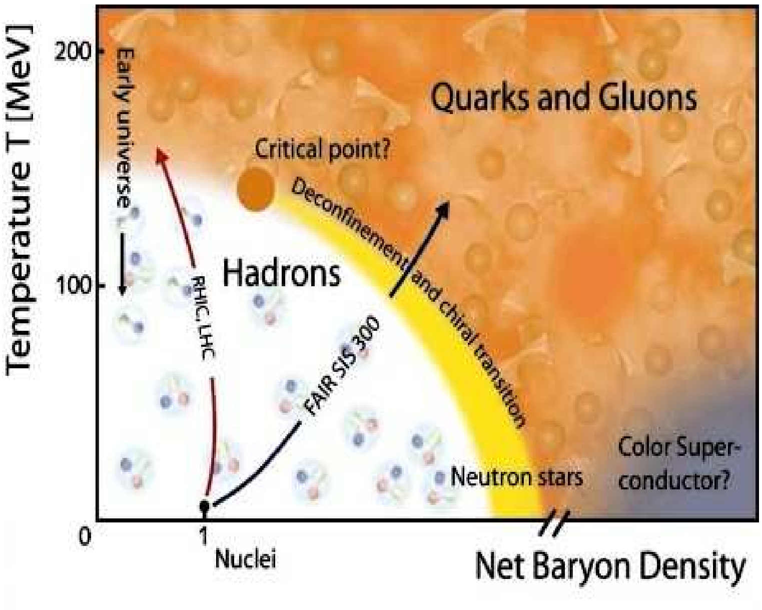

Figure 3.1: The phase diagram of nuclear matter in temperature and net baryon density plane.

experiments are devoted to studying the phase diagram of matter. The Large Hadron Collider (LHC) at CERN and RHIC at BNL are colliding heavy-ion at extremely high energy to explore the region of the high temperature and zero net baryon density. A high dense medium can be created in the laboratory by colliding heavy-ion at relatively low energy. The STAR beam energy scan (BES) is scanning the lower energy regions to search for the critical point and to study the phase transition [11]. The NA-61 SHINE experiment [12] at SPS-CERN has the goal to study the properties of the onset of deconfinement and search for the critical end point of strongly interacting matter which is pursued by investigating p+p, p+Pb and nucleus-nucleus collisions. The heavy-ion collider, NICA project at Joint Institute for Nuclear Research (JINR) at Dubna [13] is designed to study the coexistence of phases of strongly interacting matter. In most of the experiments, due to the limitation in the luminosity, only particle with higher multiplicity are detected. The Compressed Baryonic Matter Experiment (CBM) [14, 15, 16] at FAIR has a special feature to measure different types of particles including the rarely produced particle which carries valuable information of the early dense fireball. The experimental discovery of the prominent landmarks of the QCD phase diagram would be a major breakthrough for understanding of the properties of strongly interacting nuclear matter. Equally important is quantitative experimental information on the properties of hadrons in the dense matter which may explain chiral symmetry restoration and the origin of hadron mass. According to the statistical model calculations, maximum net baryon density at freeze out can be reached at SPS-CERN and at FAIR at relatively low energy collision of beam energy between 30 AGeV to 40 AGeV (for fixed-target) or between $\sqrt{s}$ =6 to 10 GeV [17]. The maximum net baryon density created at freeze out for different energies is shown in Fig. 3.2. The numbers refer to either laboratory kinetic energies for fixed-target experiments (from 5 to 40 AGeV), or to the total collision energy (from 2+2 to 100+100 AGeV)). The evolution of various particles species of a heavy-ion collision at FAIR energies is shown in Fig. 3.3. As the particles containing charm quarks are heavy, they are created at the very early stage of the reaction. The low massive vector mesons like $\omega,\ \rho$ and ϕ mesons are produced continuously via $\pi^+\ +\ \pi^-$ annihilation during the course of the reaction, and decay either again into mesons, or into a dilepton pair. The dilepton decay channel is suppressed with respect to the meson decay by about 4 orders of magnitude (corresponding to the square of the electromagnetic coupling constant $(\frac{1}{137})^2$). As the leptons are not affected by final-state interactions, this decay offers the possibility to study the properties of the early stage of the fireball. In particular, the short-lived ρ meson is a promising probe of the dense and hot nuclear matter. The hyperons and ϕ mesons have small hadronic cross sections, they carry valuable information of the high-density matter of the collision via their collective flow. The particles freeze out when density is below the saturation density. In heavy-ion experiment, these freeze-out probes are measured at beam energies between 2 to 40 GeV (for fixed target). The CBM experiment is designed to detect rarely produced particles from the high density phase. The interacting cross-section or the branching ratio of the decay channel is small. A substantial amount of data is required for the detection of the rare probes. The FAIR will provide the facilities for this experiment.

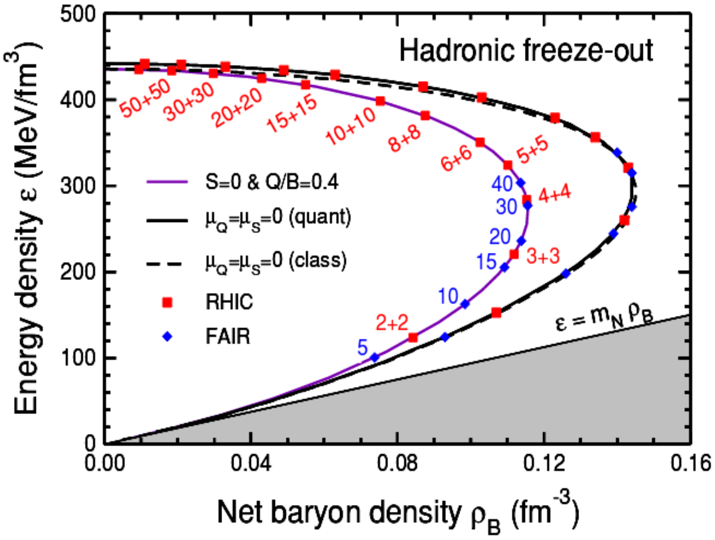

Figure 3.2: The variation of the net baryon density created in different energy of the Au + Au beam as calculated from the model. The model uses the value of net baryon density μ_B and freeze out temperatures, extracted from experimental data [18]. The symbols represent the beam energies at RHIC (total energy in each beam) of FAIR (kinetic energy of the beam for a fixed target).

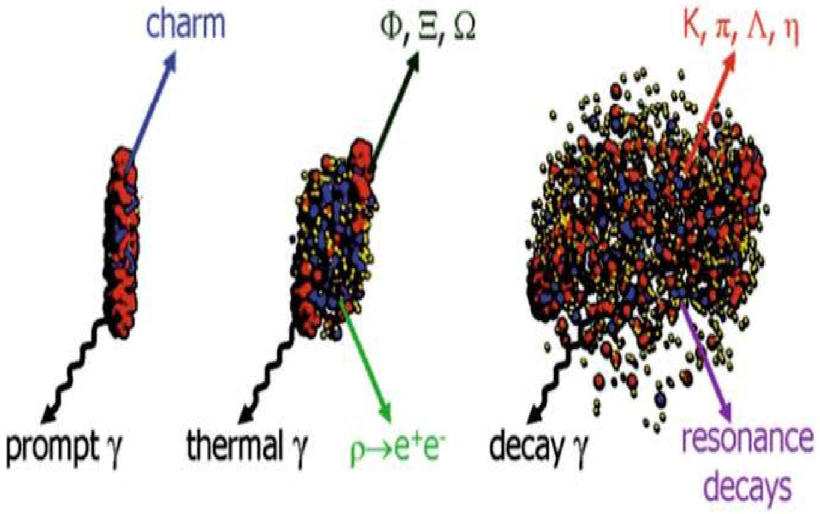

Figure 3.3: A sketch of the expansion phase of a U+U collision at a laboratory beam energy of 23 AGeV at different time steps: initial stage when the two Lorentz-contracted nuclei overlap (left), high density phase (middle), and final stage ("freeze-out") when all hadrons have been formed (right). Different particles are created in different times after the collisions. The charge particle multiplicity is about 1000, most of them are pions.

3.1 The facility of anti-proton and ion research

The international Facility for Antiproton and Ion Research (FAIR), the future accelerator facility coming up in Darmstadt will provide unique research opportunities in the research fields of nuclear, hadron, atomic and plasma physics [19]. A layout of the FAIR facility is shown in Fig. 3.4. All ions starting from protons (also anti-protons) up to the heaviest element, uranium will be accelerated in the proposed FAIR facility. This will provide the necessary broad basis for the multi-disciplinary research program proposed for the new facility. The existing accelerator facility of GSI consists of the UNIversal Linear ACcelerator UNILAC, the heavy-ion synchrotron (SIS18), and the Experimental Cooler Ring (ESR). The UNILAC with its three injectors probably is the most versatile and powerful heavy-ion LINAC in the world. With SIS18, stable nuclei of all elements in the periodic system, from hydrogen to uranium, can be accelerated to more than 90% of the speed of light. At the ESR, innovative techniques such as electron cooling and stochastic cooling have been developed and used in experiments with high-energy heavy-ion beams for the first time. In particular, the application of the beam cooling techniques to secondary beams of unstable nuclei, produced by fragmentation or fission reactions, are collected and stored, has produced seminal results. Through these techniques unprecedented beam qualities could be achieved, opening new areas of research. The SIS18 will act as the injector for the new facility. There will be two synchrotrons, namely heavy ion synchrotron 100 (SIS100) and heavy ion synchrotron 300 (SIS300) with bending powers

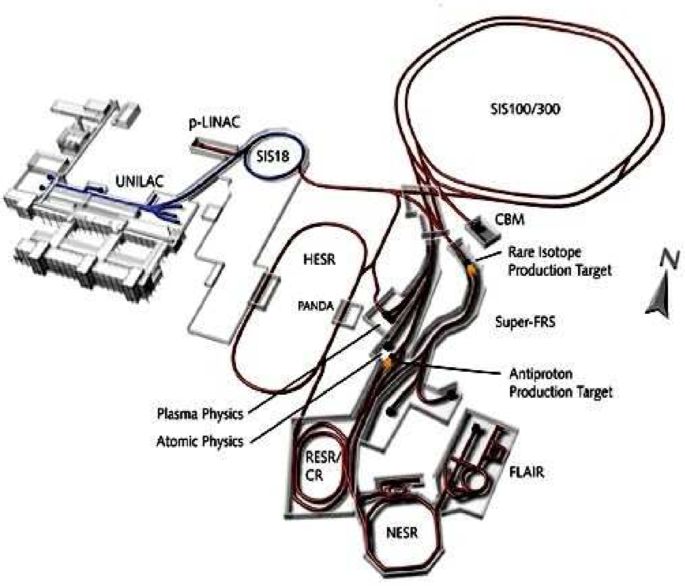

Figure 3.4: The layout of the FAIR facility along with the accelerators and the experimental facilities.

of 100 and 300 Tm respectively. The bending power or beam rigidity is defined as the product of magnetic intensity (B) and the radius of curvature (r). FAIR research program devoted to the study of dense baryonic matter will start with the collisions at low energies with primary beams from the SIS100 synchrotron (protons up to 29 GeV, Au up to 11 AGeV, nuclei with Z/A = 0.5 up to 14 AGeV), and will be continued with beams from the SIS300 synchrotron (protons up to 90 GeV, Au up to 35 AGeV, nuclei with Z/A = 0.5 up to 45 AGeV). FAIR has several experimental facilities such as Compressed Baryonic Matter (CBM) experiment, Proton and Anti-proton at DArmstadt (PANDA) experiment [20], the Nuclear Structure and Astrophysics Research (NuSTAR) experiment [21] and experimental setup for Atomic Physics and Plasma Physics (APPA) [22]. The available kinetic beam energy per nucleon depends essentially on the beam rigidity (B·r) provided by the dipole magnets:

$$\frac{E}{A} = \sqrt{(0.3\ .\ B\ .\ r\ .\ \frac{Z}{A})^2 + m^2} - m \tag{3.1}$$

with Z and A being the charge and atomic number of the ion, and m the mass of the nucleon. The beam energies for different ion species obtained for the maximum beam rigidity at SIS300 are given in Table. 3.1. The minimum available ion beam energy is about 2 AGeV.

Beam	Z	A	E/A GeV SIS100	E/A GeV SIS300
p	1	1	29	89
d	1	2	14	44
Ca	20	40	14	44
Ni	28	58	13.6	42
In	49	115	11.9	37
Au	79	197	11	35
U	92	238	10.7	34

Table 3.1: Different ion species and their energies at SIS100 and in SIS300 synchrotrons at FAIR.

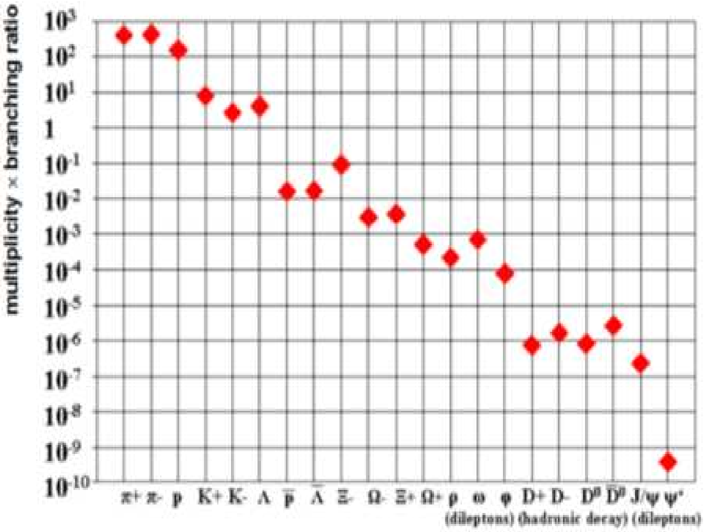

Figure 3.5: Particle multiplicities times branching ratio for central Au+Au collisions at 25 AGeV for the vector mesons (ρ, ω, ϕ, J/ψ, ψ) the decay into lepton pairs and for D mesons the hadronic decay into kaons and pions.

3.2 Probe of the dense nuclear matter

The promising diagnostic probes of the early stage of the fireball such as multi-strange baryons, dilepton pairs and charmed particles will be measured for the first time by the CBM experiment in this low beam energy ranges available at SIS100 and SIS300. As the diagnostic probes have very low production cross section and the branching ratio of decay into dilepton channel is also low, the particles such as multi-strange (anti-) hyperons, particles with charm have to be measured with unprecedented precision. One of the main challenges of the CBM experiment is to detect them. The product of multiplicity times branching ratio for various particle species produced in central Au+Au collisions at 25 AGeV is shown in Fig. 3.5. The points in the figure are estimated from either the HSD transport code [23] or the thermal model based on the corresponding temperature and net baryon density [24]. Obviously, pions are the most abundant particles. The charm mesons are suppressed by the medium produced by the collision. The suppression factor for the charm mesons are 9 orders of magnitude lesser than for the pions. In order to produce sufficient data for the rarely produced particles in a reasonable run time of the experiment, the CBM experiment is optimised to run in the high reaction rate 100 kHz to 1 MHz for the detection of low mass mesons decaying into dilepton. For the rare probes like charmonium, a reaction rate up to 10 MHz will be envisaged.

3.3 CBM experiment

The CBM experimental strategy is to perform systematically both integral and differential measurements of almost all the particles produced in nuclear collisions (i.e. yields, phase-space distributions, fluctuations and correlations) with unprecedented precision and statistics. These measurements will be performed in nucleus-nucleus, proton-nucleus, and - for baseline determination - proton-proton collisions at different beam energies. The identification of multi-strange hyperons, hypernuclei, particles with charm quarks and vector mesons decaying into dilepton requires efficient background reduction and very high interaction rates. For the detection of the rare observables, all the tracks of each collision have to be reconstructed and filtered online with respect to physical signatures. The CBM experiment will run without hierarchical trigger system. A good fraction of events is likely to be missed during trigger selection in high reaction rate. To accomplish this, self-triggered read-out electronics, a high-speed data processing and acquisition system, fast algorithms, and, last but not least, radiation hard detectors are essential requirement for a successful operation of the experiment.

3.4 Physics of CBM and observables

The CBM experiment is focused mainly on the physics involved in high density nuclear matter. The following topics are to be studied here :
(i) The equation-of-state of baryonic matter at neutron star core densities
The study of the following topics are to be done.

- The excitation function of the collective flow of the produced hadrons driven by the pressure created in the early fireball;

- The excitation functions of multi-strange hyperon production in Au+Au and C+C collisions at energies from 2 to 11 AGeV using SIS100 synchrotron. The production of the Ξ and Ω in sequential collisions concerning kaons and Λ’s, are sensitive to the density of the initial fireball.

(ii) In-medium properties of hadrons

The properties of the hadrons will be modified due to the restoration of the chiral symmetry in dense medium. The related measurements involved here are:

- The in-medium mass distribution of vector mesons decaying into dilepton in heavy-ion collisions at low energies (2 - 45 AGeV), and for a variety of collision systems. The leptons, having low interaction cross section, are penetrating probes giving information out of the dense fireball (SIS100/300);
- The production and transverse mass distribution of charmonia in heavy-ion as a function of collision energy (SIS100/300).

(iii) The transition of phase from hadronic matter to partonic matter at high net-baryon densities

The energy density up to 7 times the normal nuclear density can be achieved in central collision of heavy-ion at SIS100 energies. The signatures of the phase transition is experienced by the abrupt change or discontinuity in the excitation functions of the sensitive observables. In this regard measurement will be done for:

- The excitation function of yields, spectra, and collective flow of strange particles in heavy-ion collisions from 6 - 45 AGeV (SIS100/300);
- The excitation function of yields, spectra, and collective flow of the particles containing charm quarks in heavy-ion collisions from 6 - 45 AGeV (SIS100/300);
- The excitation function of yields and spectra of lepton pairs decayed from mesons in heavy-ion collisions at 6 - 45 AGeV (SIS100/300);
- Event-by-event fluctuations of conserved quantities like baryons, strangeness, net-charge among other observables in heavy-ion collisions with high precision as function of beam energy from 6 - 45 AGeV (SIS100/300).

(iv) Hypernuclei, strange dibaryons and massive strange objects

Single and double hypernuclei, strange dibaryons and heavy multi-strange short-lived objects are produced via coalescence in heavy-ion collisions in the region of SIS100 energies. The planned measurements include:

- The decay chains of single and double hypernuclei in heavy-ion collisions at SIS100 energies;
- Investigate for strange dibaryons and short-lived multi-strange objects. The multi-strange particles can be detected via their decay into charged particles.

(v) Measurement involving charm particle

The relevant measurements are:

- Estimate the cross sections and momentum spectra of open charm (D-mesons) in proton-nucleus collisions at SIS100/300 energies. The transparency ratio $T_A = (\sigma_{pA} \rightarrow DX)/(A \times \sigma_{pN} \rightarrow DX)$ measured for different size target nuclei can be used to study the in-medium properties of D mesons.
- Cross sections, momentum spectra, and collective flow of open charm (D-mesons) and charmonium (J/ψ) in nucleus-nucleus collisions at SIS300 energies;

3.5 CBM detector concept

The CBM experiment will measure charge particle multiplicities, phase-space distributions and flow of protons, pions, kaons, hyperons, hadronic resonances, light vector mesons, charmonium and open charm including correlations and event-by-event fluctuations in heavy-ion collisions. The main challenge of the CBM experiment is to detect a huge number of particles including hadrons and leptons and to reconstruct the primary particle by reconstructing track of each particle at the reaction rates up to 10 MHz with charged particle multiplicities up to 1000 per event. Measurements at these high rates can not be accomplished with slow detectors like Time Projection Chambers (TPC). Operation of detectors at high interaction rate requires fast and radiation hard detectors. The electronics and the data acquisition system (DAQ) should be fast enough to record all the events. The identification of the particles will be done via their decay into dilepton channel, mainly via muon (muon mode) and electron decay channel (electron mode). So the final results from the two measurements should agree with each other to provide reliable results. But the detector system and the background are different for the two modes of operation of the CBM experiment. The CBM detector system for electron measurement with Ring Imaging Cherenkov detector (RICH mode) is shown in Fig. 3.6. Another mode of operation of CBM experiment is muon mode where the particles will be detected via their decay into muons. The CBM experimental arrangement for muon detection is shown in Fig. 3.7. The Muon Chamber (MUCH) detector consists of several hadron absorbers segments with detector station, placed between two consecutive absorber segments. The numbers and the positions of the absorbers and detector stations depend on the various MUCH configurations in SIS100 and SIS300. The CBM detector system consists of the following detector components :

3.5.1 Super conducting magnet

The central part of the CBM detector system is the superconducting dipole magnet. The target station and the silicon tracking system and micro vertex detector are placed in the magnet gap. The magnet has to provide a vertical magnetic field with a bending power of 1 T.m over a length of 1 m from the target. The magnet gap has a height of 140 cm and a width of 250 cm in order to accommodate the silicon tracking stations with a

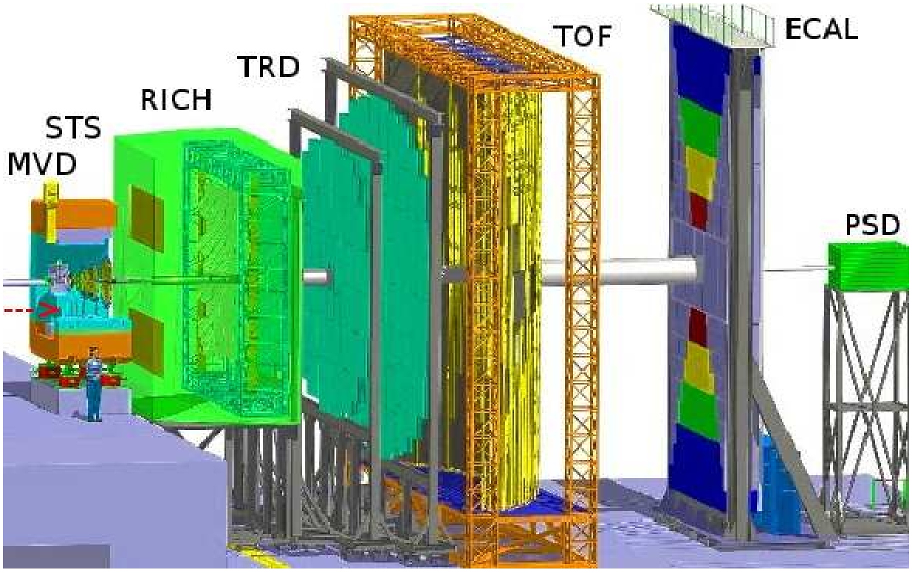

Figure 3.6: The CBM detector system for the measurement of electrons (electron mode). The experimental setup consists of a large acceptance dipole magnet, Silicon Tracking Stations (STS), Micro Vertex Detector (MVD), Ring Imaging Cherenkov detector (RICH), Transition Radiation Detector (TRD), Resistive Plate Chambers (RPC), an Electro-magnetic Calorimeter (ECAL) and a Particle Spectator Detector (PSD).

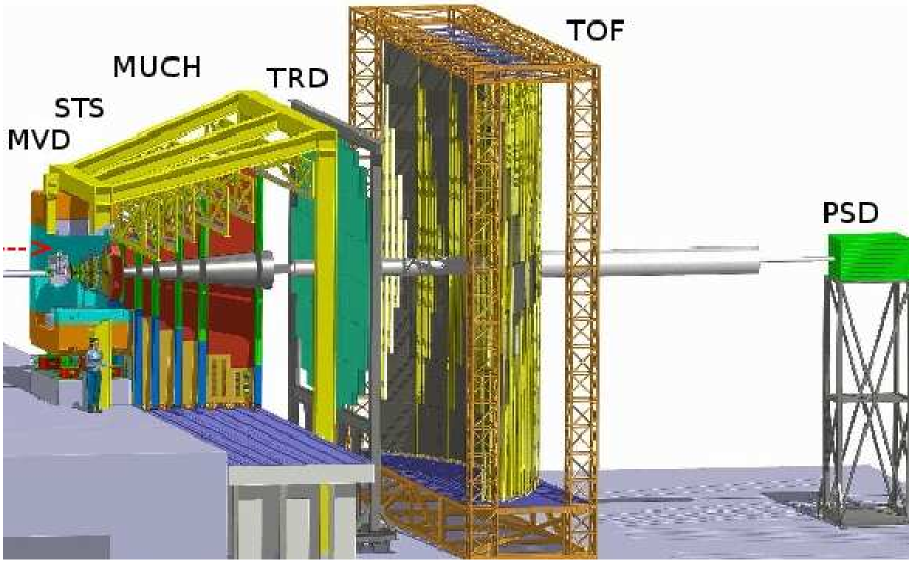

Figure 3.7: The CBM detector system for the measurement of muons (muon mode). Its components are a large acceptance dipole magnet, Silicon Tracking Stations (STS), Micro Vertex Detector (MVD), Muon Chamber detector (MUCH), Transition Radiation Detector (TRD), Resistive Plate Chambers (RPC), an Electro-magnetic Calorimeter (ECAL) and a Particle Spectator Detector (PSD).

polar angle acceptance of ±25° and a horizontal acceptance of ±30°. The Magnet has superconducting cylindrical coils and is of H-type in an iron yoke.

3.5.2 Silicon tracking station

The silicon tracking station is designed for the reconstruction of the tracks and determination of the momentum of the charged particles. It is placed inside the dipole magnet and consists of 8 tracking layers of silicon detectors. The layers are located downstream the target at a distance between 30 and 100 cm from the interacting point inside the dipole magnet. The multiplicity of the charged particle in STS is up to 600 per event. The necessary momentum resolution is of the order of $\Delta p/p = 1\%$. Such performance can be obtained only with ultra low material budget of the stations, imposing particular restrictions on the position of the power-dissipating front-end electronics in a small volume. The STS stations are based on the silicon micro-strip detectors on lightweight ladder-like mechanical supports. There will be micro-cables connected to fast electronics for reading out the signals from the sensors. The read out sections will be placed at the periphery of the stations where cooling lines and other infrastructure can be placed. The sensors will be double-sided with a stereo angle of 15° and strip pitch is 58 μm. The length of the strips is between 20 and 60 mm and a thickness of 300 μm. The micro-cables will be built from sandwiched polyimide-aluminium layers of several 10 μm thicknesses. As by design, the momentum resolution is dominated by multiple scattering, the material budget of the STS has to be kept as small as possible. The total material budget including support structures and cables may amount to about 400–800 μm silicon equivalent, but is not homogeneous. The hit density at 1^{st} layer will reach up to 10 MHz/cm^2 as obtained from simulation using minimum-bias Au+Au collisions at 25 AGeV. The track finding in the STS detector system, operated in an inhomogeneous magnetic field, is based on the cellular automaton method [25]. Subsequent track and vertex fitting make use of a Kalman filter. The typical hit resolution of the order of 25 μm will be achieved. The read-out chip, named STS-XYTER, is for signal detection from the double-sided silicon micro-strip sensors in the CBM environment. This self-triggering ASIC based on nXYTER chip [26] provides both timing and energy information for each incoming signal in its channels.

3.6 Micro-Vertex Detector (MVD)

The identification of D mesons via their weak hadronic decay into pions and kaons requires a dedicated detector for vertex reconstruction in addition to the STS. The lifetime of D^0 meson and D$^\pm$ are $\tau = 123$ μm/c and $\tau = 314$ μm/c respectively. The secondary decay vertices of the D mesons have to be reconstructed in order to suppress the background of promptly emitted pions and kaons with high precession. The MVD will also measure the electrons where close pairs will be rejected to reduce combinatorial background. The information recorded in MVD will be used to improve the hyperon identification. The detector should have high position resolution for this and also a low material budget to reduce multiple scattering. The Monolithic Active Pixel Sensors (MAPS) will be used for this measurements. The size of this pixel sensors will be between 25×25 μm^2 and 40×40 μm^2. A position resolution of $\sigma = 3$ μm can be achieved with the pixel sensor of size 40×40 μm^2. The aim of the R & D is to build MAPS detector stations with a total material budget of about 300 μm silicon equivalent for the sensors and the support structures. A material budget of about 500 μm silicon equivalent might be more realistic for the larger MAPS stations. The MVD has 2 layers of MAPS sensor located at 10 and 20 cm downstream the target. Another station may be placed at 5 cm downstream the target. All the stations will be very thin due to restriction in the material budget. As per simulation, the MVD is capable of determining the secondary decay vertices of the D mesons with a resolution of about 50-100 μm along the beam axis. The resolution strongly depends on the thickness of the 1^{st} MAPS station and its distance from the interaction point. The detector should be radiation hard. The R & D is focused on the development of a detector of radiation hardness 10^{13} n_{eq} which is corresponding to 10^{12} minimum bias Au + Au collision at 25 AGeV. The readout speed of MAPS is 10 μs. During the operation with SIS300 synchrotron, a few events will pile up randomly in one readout frame of the MAPS when operated in 100 kHz interaction rate. A pile up of 10 events in the MAPS can be tolerated with a small decrease in performance of the detector as obtained from simulation. The inner part of the 1^{st} detector can run about 4 months at this interaction rate; after that the part has to be replaced.

3.6.1 Ring Imaging Cherenkov Detector

Another mode of operation of CBM experiment is the electron mode of operation. In this mode, the particles will be reconstructed via their decay into a electron-positron pair. The Ring Imaging Cherenkov (RICH) [27, 28] will be used for this purpose. The electrons of momenta up to 8 GeV/c will be detected in RICH. In case of SIS100 operation, the RICH detector will be supplemented by 4 layers of Transition Radiation Detector (TRD). The RICH detector will use CO_2 as a radiator gas at 2 mbar overpressure with a pion threshold of 4.65 GeV/c. The dipole magnet bends the charged particle track horizontally, so the RICH geometry foresees two mirror halves. The two halves are tilted by an angle of 10° against the horizontal plane. The mirrors will focus the Cherenkov rings on photodetector planes that are located behind the yokes of the magnet and shifted upwards or downwards in the stray field. The mirror covers a total area of 12 m^2. Each mirror consists of 40 single trapezoidal mirror tiles. Each tile has a radius of curvature of 3 m and 6 mm glass thickness with a reflective and protective Al + MgF_2 coating. Each half of the photo-detector plane is split into two wings made by 250 Mono-Anode Photo-Multiplier

Tube (MAPMT) Hamamatsu H12700. They provide sufficient granularity, very good noise performance, stable operation and high rate capability up to highest interaction rate of 10 MHz. The MAPMTs will be read out by fast self-triggered readout electronics based on the TRB3 development for HADES [29]. The number of measured photons in a ring is about 20. The number of rings increases to 100 due to pair conversion of gamma rays in the material in front of the RICH per central Au + Au collision at 25 AGeV. A pion suppression of the order of 500-1000 is achieved for $p< 10$ GeV/c [30]. The factor could be up to 10^4 including Transition Radiation Detector (TRD) and Resistive Plate Chamber (RPC).

3.6.2 Muon Chamber Detector (MUCH)

A conventional muon chamber detector consists of a thick hadron absorber to stop the hadrons, photons, electrons and low momentum muons. The high momentum muons can pass through the absorbers and are detected after the absorber. The main goal of the MUCH detector is to reconstruct the mass of different particles over a broad region of mass starting from the low mass vector meson, like ρ to heavy massive particles like J/ψ via their decay into dimuon. At the low mass region (up to 1 GeV/c^2), the signature of the modification of the vector meson spectral functions in the dense medium can be addressed. The information of the thermal radiation from the hot fireball can be extracted from the intermediate mass region. The suppression of particles like J/ψ, indicates production of a deconfined state of nuclear matter in this FAIR energy region [31]. The muon detection system, MUCH, will use segmented absorbers to identify muons by detectors placed in between two absorbers. The detailed study and the simulation results are reported in [14]. To optimise the total width of the absorber, simulations has been done using UrQMD event generator [33] and GEANT3 [34] for Au + Au collisions at 25 AGeV. The fraction of the surviving particles vs. the length of the absorber is shown in Fig. 3.8. A total thickness of 1.5 m of the iron absorber is necessary for detection of the low mass vector meson; for the detection of the muons from the heavy massive particles like J/ψ an additional length of 1 m is necessary. As MUCH detector will use segmented absorbers, so the length of the individual absorbers and their positions have to be optimised. Due to multiple scattering inside the 1^{st} absorber, the number of hits in the 1^{st} detector increases abruptly. Hence the rate of particle on the 1^{st} detector station increases and there may be a mismatch to reconstruct tracks leading to an increase in the background. So there would be a compromise between the hadron absorption and multiple scattering. Simulation studies have been performed with the 1^{st} absorber as iron and as carbon. The χ^2's of the reconstructed tracks taking 4 STS hits and 2 MUCH hits are shown in Fig. 3.9 with two sets of the absorber, 20 cm iron and 60 cm carbon as the 1^{st} absorber. The χ^2 for the muons from the low mass vector meson are similar for the two set-ups but in case of carbon the background is one order of magnitude lower.

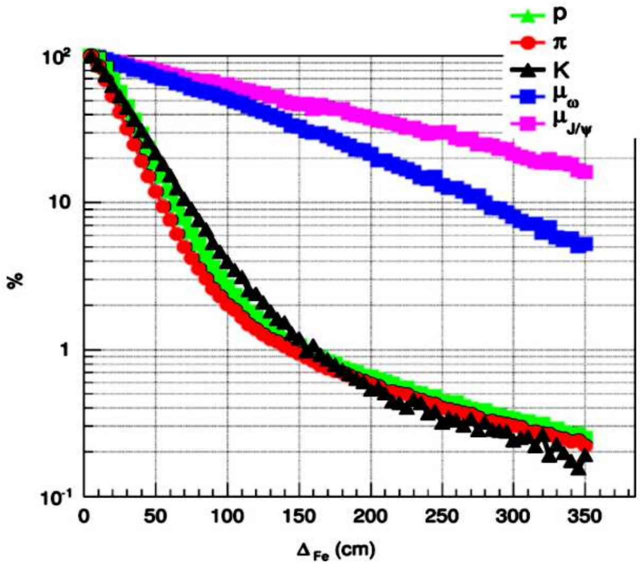

Figure 3.8: Fraction of different types of surviving particles as a function of the transverse length in iron absorber.

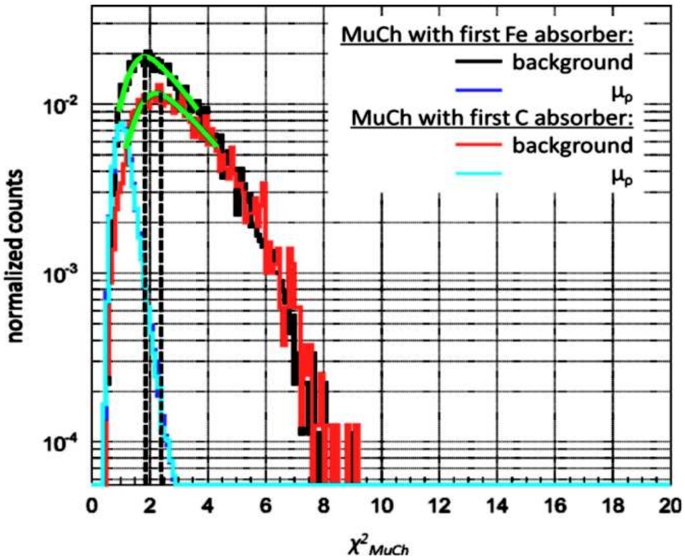

Figure 3.9: The distribution of signal from muons and background for two setup with 20 cm iron and 60 cm carbon respectively.

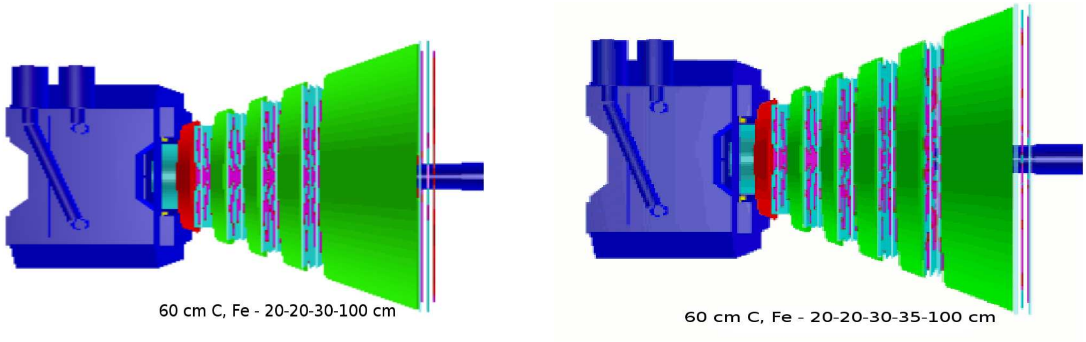

(a) (b)

Figure 3.10: The layout of the MUCH detector (a) SIS100 configuration with 60 cm carbon, iron of 2×20 cm, 30 cm, 100 cm, (b) SIS300 mode of operation with 60 cm carbon, iron of 2×20 cm, 30 cm, 35 cm, 100 cm

So, 60 cm carbon is suitable as the 1^{st} absorber. Also, carbon as the 1^{st} absorber has an added advantage of placing it inside a magnet. The total length of the absorber is 265 cm which is 13.5 times the hadronic interaction length for the detection of the muons from the charmonium. The absorbers are 60 cm carbon, iron absorbers of length 2×20 cm, 30 cm, 35 cm, 100 cm for its operation in SIS300 configuration. For the measurement of the low momentum muons from the decay of the low massive vector meson like ρ, ω, ϕ, five absorbers - 60 cm carbon, iron of 2×20 cm, 30 cm, 100 cm will be used as the start version of the CBM Experiment. The SIS100 and SIS300 configuration of the MUCH layout are shown in Fig. 3.10. The absorbers are placed with a gap of 30 cm between them. There is a gap of 30 cm between two absorbers for the detectors. The angular acceptance of MUCH is $\pm 5°$ to $\pm 25°$. The lower limit is fixed by the beam pipe and the upper limit is the opening of the dipole magnet. Each detector station consists of 3 layers of detector planes. The gap between the absorber and the detector layer is 10 cm and the layers are separated by a gap of 5 cm. The 1^{st} absorber will be placed at a distance 120 cm from the interaction point. The rate of particle at the 1^{st} detector station after the 1^{st} absorber will reach up to 1 MHz/cm^2 as per simulation performed using UrQMD event generator and GEANT3 simulation for Au + Au collisions at 25 AGeV [35]. So the detector at the 1^{st} detector station should be capable of handling high rate of particles and it should be radiation hard to work efficiently in a harsh radiation environment. Out of the presently available detector technologies, Gas Electron Multiplier (GEM) based detectors will be used at the first two detector stations of MUCH. The particle rate at the rest of the stations are relatively low, so RPC and straw tube based detectors will be used. Trapezoidal shape large GEM modules will be used to cover the acceptance of the detector. For the 1^{st} detector station, a total of 16 large GEM modules is necessary. 24 such modules are required for the 2^{nd} detector station [14]. For detection of the muons efficiently for the reconstruction of the tracks, an efficiency of the detector $> 90\%$ is an essential condition. The GEM detector has been tested with an efficiency $> 95\%$ with high intensity beam [36, 37]. Research and development of the GEM detector for use in MUCH will be discussed in Chapter-4 in detail.

3.6.3 Transition Radiation Detector (TRD)

The transition radiation detector will be used for particle tracking and for the identification of electrons and positrons with momentum p>1.5 GeV/c ($\gamma \ \geq$1000). TRD has 3 detector layers located at a distance of about 5 m, 7.2 m and 9 m respectively, downstream the target with a total active area of 1100 m^2 for SIS300 configuration. The particle rate at the 1st layer will reach 100 kHz/cm^2 for an interaction rate of 10 MHz for minimum bias Au + Au collision at 25 GeV. Thus the detector development aims to improve the electron identification performances and development of a high granularity, fast detector specially for the inner region of the detector. In a central collision, the particle density at the 1st layer will reach up to 0.05/cm^2. The minimum size of a cell should be 1 cm^2 to keep the occupancy below 5%. The readout pads of the TRD detector are the rectangular pads giving a position resolution of 300-500 μm across and 3-30 mm along the pad. The consecutive TRD layers are rotated from the previous one by an angle of 90°. Micro-Wire Proportional Chamber (MWPC) and GEM based gas detectors have been tested with a particle rate of 400 kHz/cm^2 without any loss of efficiency. The pion suppression ratio tested with 12 TRD layers is found to be above 100 with an electron efficiency of 90%. During the operation of SIS100, one TRD station with 3 detector layers will be used as an intermediate tracker between the STS and the Time Of Flight (TOF) wall.

3.6.4 Timing Multi-Gap Resistive Plate Chamber (MRPC)

An array of MRPC will be used for the identification of the hadrons via TOF measurements. The total area of the TOF wall will cover about 120 m^2. The TOF is located at 6 m downstream of the target in case of measurement at SIS100 and at 10 m for the case of SIS300. The time resolution of the MRPC will have to be $\sim$ 80 ps for the identification of the hadron. The R & D on timing MRPCs is focused on excellent time resolution, high rate capability, low resistivity material and long-term stability. The particle rate at the inner part of the TOF for the 10 MHz interaction rate at Au + Au collisions will be 20 kHz/cm^2. The time resolution for a prototype low-resistivity glass MRPC has been found to be 40 ps at 20 kHz/cm^2. The readout pad size is 5 cm^2 at small deflection angle at an occupancy below 5% for central Au + Au collisions at 25 AGeV.

3.6.5 Electromagnetic Calorimeter (ECAL)

A “shashlik” type calorimeter as installed in the HERA-B, PHENIX and LHCb experiments, will be used to detect direct photons and neutral mesons ($\pi_0, \ \eta$) decaying into photons. The ECAL will be built using 140 layers of 1 mm lead and 1 mm scintillator, with cell sizes of 3 × 3 cm^2, 6 × 6 cm^2 and 12 × 12 cm^2. The shashlik ECAL modules can be arranged as a wall or in a tower type geometry with variable distance from the target.

3.6.6 The Projectile Spectator Detector (PSD)

The collision centrality and orientation of the reaction plane will be determined by the PSD [38]. A very precise characterization of the event class is very important for the analysis of event-by-event observables. The detector will measure the non-interacting nucleons that are not involved the nuclear collisions. The reaction plane has to be well defined in case of study of collective flow of the particles. The PSD consists of a full compensating lead-scintillator calorimeter that will provide good and uniform energy resolution. The PSD consists of 12 × 9 individual modules of calorimeter. Each module has 60 lead-scintillator layers of are 10 × 10 cm^2. The light from the scintillator is read out via wavelength shifting fibers connected to the Multi-Avalanche Photo-Diodes (MAPD) with an active area of 3 × 3 mm^2 and a pixel density of $10^4/\text{mm}^2$.

3.6.7 Online event selection and data acquisition

The measurement of the rare probes needs high interaction rate of the particle for enough statistics for the operation of the detector for a reasonable run time. The online event selection and the data acquisition for the CBM experiment will be designed for operation at an interaction rate of 10 MHz. The beam intensity corresponding to 10 MHz beam is 10^9 ions/s and a 1% target interaction. Assuming a data volume of 40 kB for minimum bias Au + Au collision, the data collection rate will be 1 Gb/s. Under this situation, the data acquisition system can accept an event rate of 25 kHz. Therefore, for the operation of CBM experiment at the highest interaction rate of 10 MHz, an on-line event algorithm (also hardware) is required which will reject the background by a factor of 400 or more. A fast on-line event reconstruction algorithm based event selection system will be used for this purpose. The system will be equipped with PC farm with many-core CPUs and GPUs. In this regard, many-core fast architectures are under investigation from the leading companies like - Intel, IBM, NVDIA and AMD. For the track reconstruction of the muons, cellular automaton and Kalman filter technique will be used. Advanced languages like - CUDA, Ct, OpenGL using parallel programming code will be used for faster performance. The trigger selection for the open charm production is based on the selection of the secondary vertices from the STS and MVD. The suppression factor for J/ψ will be highest when high energetic electron-positron pairs or dimuon are detected in TRD or in the MUCH. No on-line selection is possible for the low-mass electron pairs because there are large numbers of rings/event in the RICH detector caused by the material budget of the STS. In this case, some background rejection on the trigger level is feasible.

3.6.8 Dilepton measurement in CBM experiment

The measurement of the dilepton from the decay of the rare probes is difficult for their low multiplicity and large background due to other charged particles. For the measurement of dimuon, the combinatorial background is composed of the weak decay mesons and misidentified hadrons and the background from the physical dimuon sources. The dilepton measurement is an interesting tool to study the properties of the nuclear matter created in heavy-ion collision. The dimuon from the decay of ρ indicates the in-medium modification of its mass. The in-medium modification of the properties of the ρ meson is observed when chiral symmetry is restored. The dimuons from the thermal radiation is continuously created; these dimuons reflect the temperature of the fireball. The suppression of the J/ψ due to colour screening, is a signature of the QGP [39]. No dilepton measurement has been done below the top SPS energy (158 GeV). The CBM experiment will measure the dilepton in the energies between 2 GeV and 40 GeV. So, dilepton measurement in this region of energy where highest net baryon density will be created, will open a new era of dilepton measurement. The CBM experiment will systematically measure both dielectron and dimuon in p+p, p+A and A + A collisions for different beam energies and sizes of the collision system. The dielectron and dimuon high-precision data will complement each other, and will provide a complete picture of dilepton radiation from dense baryonic matter. The identification of the muons with the segmented absorber allows us to identify muons over a wide range of momentum depending on the number of absorbers it passes through. But this system is well suited for the high momentum muons; the soft muons will be absorbed. The concept of the CBM muon detection is to detect muon by instrumented absorbers for momentum dependent identification of the muons. The reconstructed track which passed a certain amount of absorber material will be considered as the muon if the hadrons with the given momentum should have been absorbed. The main challenge of dilepton measurement is to reconstruct the tracks within a high hit density mainly due to charged particles punching through the absorber, and by muons from the decay of pions or kaons in the trackers. In case of identification of the electron pairs in the RICH detector, there is a huge background due to the electron pairs from the γ conversion in the target and from the π_0 and η Dalitz decays. In central Au + Au collision at 25 AGeV, simulation results of production of 365 π_0 which leads to 7 electron-positron pairs; 3 from γ conversion, and 4 from π_0 Dalitz decay in the target [40]. The major part of the combinatorial background comes from the pions misidentified as electron due to limited e-π separation in the detector.

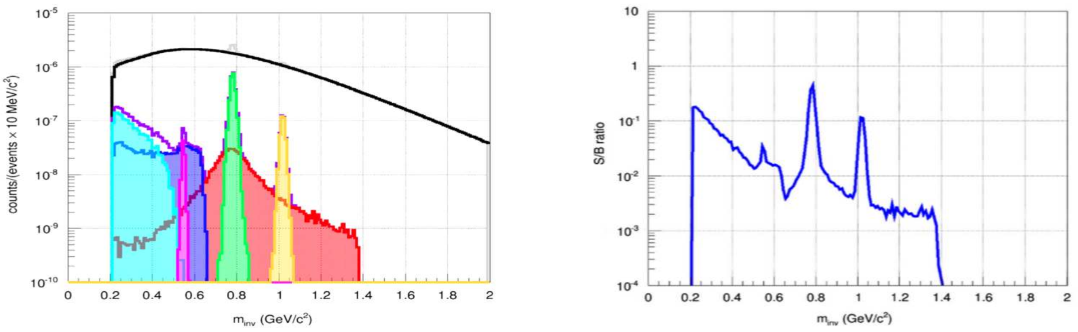

(a) (b)

Figure 3.11: (a) Invariant mass distributions of reconstructed dimuon from decaying low mass vector mesons along with the combinatorial background simulated for central Au + Au collisions at 25 AGeV, (b) S/B ratio of the low mass dimuon invariant mass spectra.

3.6.8.1 Low mass vector meson (LMVM) simulation

For the simulation of the detection of the dimuon in the MUCH detector, the PLUTO [41] and UrQMD event generators are used to generate the input signal to the detector. The signal multiplicity has been taken from the HSD model [23]. The PLUTO generates the phase space distributions and decay of muons. The temperatures (slope parameters) for the generation of low-mass vector meson and J/ψ are taken as 140 MeV/c and 170 MeV/c respectively [14]. The following decay channels are considered for low mass vector meson, $\omega \rightarrow \pi_0\mu^+\mu^-$, $\omega \rightarrow \mu^+\mu^-$, $\eta \rightarrow \mu^+\mu^-$, $\eta \rightarrow \gamma\mu^+\mu^-$, $\rho^0 \rightarrow \mu^+\mu^-$, $\phi \rightarrow \mu^+\mu^-$. The background is estimated from the invariant mass spectra from the muons from the UrQMD events only. The super-event technique was applied to increase the statistics in the background. In super-event technique method, the reconstructed tracks from large central UrQMD events are mixed and they are used to calculate the combinatorial background. The signal-particle was reconstructed from the UrQMD events to obtain the signal efficiency. The signal multiplicity and branching ratio were taken into account with proper weight of the normalisation of the background. The distribution of the invariant mass of the LMVM form the reconstructed muon pair is shown in Fig. 3.11.a along with the combinatorial background. The signal to background (S/B) ratio calculated from the Fig. 3.11.a is shown in Fig. 3.11.b. The S/B ratio is comparable or even better than the existing muons system at similar energies. The values of the significance are 214.6, 21.4 and 44.7 for ω, ρ_0 and ϕ respectively. The effective efficiencies are 0.83% for ω, 0.29% for ω Dalitz decay, 1.47% for the ϕ, 0.46% for the η, and 0.22% for the η Dalitz decay. The efficiencies depend on the cuts used during simulation. The set of the cuts is listed in Table. 3.2. It should be mentioned that there is a loss of efficiency due to geometrical acceptance, STS track reconstruction efficiency, STS-MUCH track matching efficiency.

Particle	No. of MUCH hits	No. of STS hits	χ^2 of MUCH track	χ^2 of vertex
J/ψ	17	7	1.5	2.0
ω	14	6	1.5	2.0

Table 3.2: The MUCH and the STS cuts used for the simulation.

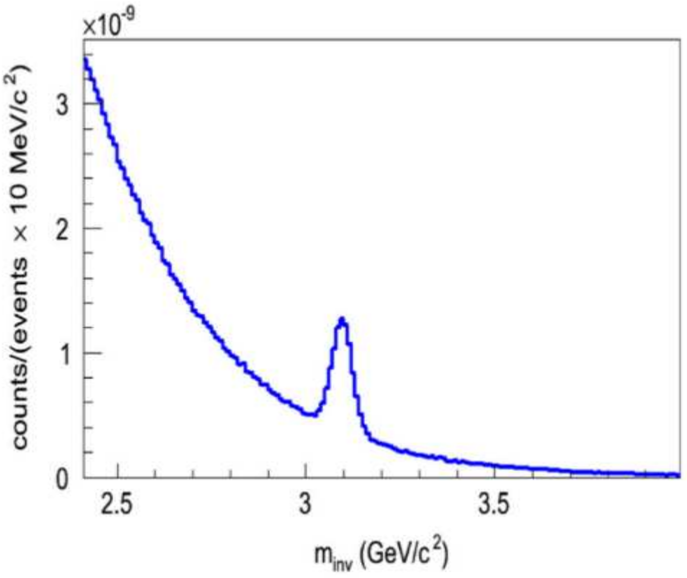

Figure 3.12: The invarient mass spectra of the reconstructed muons from J/ψ with the background.

3.6.8.2 J/ψ simulation

The J/ψ will be measured with the full absorber setup using 6 absorbers because the decayed muons from J/ψ will have enough momentum to pass through the 6 absorbers. The invarient mass spectra of the reconstructed muons is shown in Fig. 3.12 along with the background, simulated using Au + Au collisions at 25 AGeV. The peak of J/ψ is clearly visible over the background. J/ψ is detected with an efficiency of 8.2%. The S/B ratio and the mass resolutions are 0.94 and 29.6 MeV respectively [14]. The significance of the peak is 32.6. The background is mainly dominated by the muons from the decay of pions and kaons.

3.7 Summary

The heavy-ion collision experiments are dedicated to investigating the phase diagram of strongly interacting matter. The CBM experiment at FAIR has a special feature to study the properties of the highly dense nuclear matter. The CBM experiment will collide ions at the energies between 2 AGeV to 45 AGeV (on fixed target). According to theoretical calculations, nuclear matter density will reach up to 7 times the normal nuclear matter at 10 AGeV. The transition of phase from hadronic matter to QGP is expected to be first order phase transition followed by a critical end point where first order phase transition ceases to exist. The main challenge of this experiment is to identify the tracks of the particle in huge hit density. The experiment will acquire data in the self-trigger mode. The CBM experiment will run in two modes of operation, namely - electron mode and muon mode. The particles will be identified by their decay into dilepton. The electron-positron will be detected by a ring imaging Cherenkov detector. The dimuons will be detected by segmented absorber of varying lengths. The tracking detectors are placed in between two absorbers. For the detection of the rare particles like J$/\psi$, the interaction rate has to be $\sim$ 10 MHz for sufficient statistics in a reasonable run time of the experiment. The hit density at the 1^{st} detector station will reach 1 MHz/cm^2 at Au + Au collision at 25 AGeV. So the detector should be fast enough to cope with the rate of the charged particles. Out of the presently available detector technologies, GEM electron based detector is found to be a suitable candidate for this purpose. The GEM based detector has been reported to have high efficiency ($>$ 98%) at comparatively low voltage and can handle high rate of the particle.

Bibliography

[1] S. Borsanyi et al., JHEP **1009** (2010) 073.

[2] A. Basavov et al., arXiv:1111.1710v1.

[3] Y. Aoki et al., Nature **443** (2006) 675.

[4] M. A. Halaz et al., Phys. Rev. D **58** (1998) 096007.

[5] R. Gavai et al., Phys. Rev. D. **71** (2005) 114014.

[6] M. A. Stephanov, Int. J. Mod. Phys. A **20**, (2005) 4387.

[7] A. Andronic et al., Nucl. Phys. A **837** (2010) 65.

[8] D. Bailin et al., Phys. Rep. **107** (1984) 325.

[9] M.G. Alford et al., Phys. Lett. B **422** (1998) 247., arXiv:hep-ph/9711395v4.

[10] R. Rapp et al., Phys. Rev. Lett. **81** (1998) 53., arXiv:hep-ph/9711396v1.

[11] A. Schmah, Cent. Eur. J. Phys., **10** (2012) 1238.

[12] N. Abgrall et al., JINST **9** (2014) P06005.

[13] NICA White Paper, http://nica.jinr.ru/files/WhitePaper.pdf.

[14] T. Ablyazimov et al., Eur. Phys. J. A **53** (2017) 60., arXiv:1607.01487 [nucl-ex].

[15] P. Senger, Journal of Physics: Conference Series **50** (2006) 357–360.

[16] J. M. Heuser, Nucl. Phys. A **830** (2009) 563c-566c, arXiv:0907.2136v3 [nucl-ex].

[17] J. Randrup, J. Cleymans, Phys. Rev. C **74**, 047901 (2006) 852.

[18] J. Cleymans, et al., Phys. Rev. C **73**, 034905 (2006) 852.

[19] J. M. Heuser, Nuclear Physics A **830** (2009) 563-566.

[20] T. Stohlkera et. al., Nucl. Instr. Meth. B **365** (2015) 680-685.

[21] A. Herlert et al., EPJ Web of Conferences, **71** 00064 (2014).

[22] APPA - Atomic, Plasma Physics And Applications..

[23] W. Cassing, E.L. Bratkovskaya, and A. Sibirtsev, Nucl. Phys. A **691** (2001) 753, arXiv:nucl-th/0010071v2, and E.L. Bratkovskaya, priv. comm.

[24] A. Andronic, P. Braun-Munzinger, J. Stachel, Nucl. Phys. A **772** (2006) 167., arXiv:nucl-th/0511071v3.

[25] I. Kisel, Event reconstruction in the CBM experiment, Nucl. Instr. Meth. A **566** (2006) 85.

[26] A. S. Brogna, *et al.*, Nucl. Instr. Meth. A **568** (2006) 301.

[27] C. Höhne et al., Nucl. Instr. Meth. A **595** (2008) 187.

[28] C. Höhne et al., Nucl. Instr. Meth. A **639** (2011) 294.

[29] A. Neiser et al.,JINST **8** (2013) JINST C12043.

[30] Technical Design Report for the CBM : Ring Imaging Cherenkov (RICH) detector, GSI, Darmstadt (2013).

[31] Pratha Pratim Bhaduri et al., **88** (2013) 061902.

[32] S. Ahmad *et al.*, Nucl. Instr. Meth. A **775** (2015) 139-147.

[33] S. Bass et al., Journal of Physics G Nucl. Part. Phys., 25 (1999) 1859-1896.

[34] R. Brun et al., GEANT3, CERN DD/EE/84-1, 1987.

[35] Technical Design Report for the CBM Muon Chambers (2015) GSI, Darmstadt.

[36] A. K. Dubey et al., Nucl. Instr. Meth. A , **718** (2013) 418-420.

[37] A.K.Dubey et al., Nucl. Instr. Meth. A , **755** (2014) 62-68.

[38] Technical Design Report of the CBM Experiment: Projectile Spectator Detector (2015) GSI, Darmstadt.

[39] T. Matsui, H. Satz, Phy. Lett. B, **178** (1986) 416-422.

[40] B. Friman et al.,The CBM Physics Book, Lect. Notes Phys. **814** (2011) 1-980., Spriger, Berlin.

[41] I Fröhlich et al., Journal of Physics: Conference Series, **219** (2010) 032039.

Chapter 4

Research & Development of GEM Detector for MUCH

GEM technology based detectors are being used in many high energy heavy-ion collision experiments such as COMPASS [1], CMS [2, 3], STAR [4]. GEM detector is being used widely because of its excellent time and position resolution. This detector is capable of handling high rate of particles [5, 6, 7]. The time projection chamber (TPC) of ALICE experiment at LHC will upgrade its end plate MWPC detectors to GEM based detectors to handle high collision rate ($\sim$ 50 kHz) in future Run-3 [8]. In CBM experiment the MUCH detector will face high flux of particles (up to 1 MHz/cm^2 for Au+Au collision at $\sqrt{s} = 25$ AGeV in SIS300 configuration). The muon chamber of CBM experiment will use GEM detector to track the dileptons originating from the decay of the charmonium and low mass vector mesons like ρ, ω, ϕ. For efficient operation of the GEM as a tracking device, the efficiency of the detector should be >90%. GEM detector has been reported to perform at an efficiency >98% [9]. The study of rate handling capacity of the GEM detector has not been done for their application in CBM experiment. So application specific research and development are necessary, particularly on rate handling capacity, for making it suitable for MUCH detector in this experiment. In this direction, we started R & D on GEM using a small size triple GEM prototype. After successfully testing the small one, we went on develope an intermediate size GEM prototype. The active area of the readout anode PCB for this GEM was trapezoid shape. Even after successfully testing two prototypes at high efficiency, two important criteria for their use in MUCH remained unfulfilled, i.e. the large size and rate capability. Next, a trapezoid shape full-size triple GEM module suitable for the 1st detector station of MUCH has been tested. In this chapter, the R & D of GEM prototypes will be described in detail along with their performance using X-rays, as well as ion beams.

4.1 R & D on small GEM prototype

4.1.1 Fabrication of the GEM chamber

A small 10 cm×10 cm triple GEM prototype was assembled using standard GEM foils exported from CERN in VECC, India and at GSI, Darmstadt. A schematic diagram of different parts of a GEM prototype is shown in Fig. 4.1. The top drift cathode plane is a Kapton plane of 50 μm thickness with the bottom side coated with copper of 5μm thickness. Three 10 cm×10 cm GEM foils are stretched inside a Flame Retardant (FR4) plastic frame, placed one after another maintaining the gaps. The gaps are maintained using FR4 spacers. The spacers are rings of 0.5 mm thickness. The typical gap parameters of the GEMs are listed in table 4.1.

Gap Name	GEM (VECC)(mm)	GEM (GSI) (mm)
Drift Gap	3	3
Transfer Gap1	1	2
Transfer Gap2	1	2
Induction Gap	1.5	2

Table 4.1: The gap parameters of the GEM detectors assembled at VECC and GSI

So to maintain a drift gap of 3 mm thickness, we need 6 such spacers. At the bottom of the structure, an anode readout Printed Circuit Board (PCB) with one side etched into small square readout pads is placed. The dimensions of the pads are 3 mm×3 mm and 6 mm×6 mm for the GEM prototypes fabricated at VECC and GSI, respectively. The pads are separated from each other by a gap of 0.2 mm. A four layered PCB was used to accommodate the readout channels. The structure is placed inside a G10 housing frame. The frame is made gas-tight using ’O’ ring rubber seal. A voltage divider circuit, made of several resistances, is used to distribute voltages to the foils. For the GEM made at VECC, the resistor values are chosen to supply same voltage drops across each GEM foil (ΔV_{GEM}). The readout anode PCB of VECC GEM has 512 readout pads. The readout channels are guided into four groups, each connected to a 68 pin connector. The connectors are fixed at the edges of the chamber. The Front End Board (FEB), connected to the side of the chamber, is used to read out the signals from each readout pads. A FEB can read two connectors, i.e. 128 readout channels. So four such FEBs are necessary to read 512 channels of the VECC GEM. There is a Read Out Controller (ROC) that can handle 2 FEBs, i.e. 256 channels. A photograph of the VECC GEM chamber is shown in Fig. 4.2.

Another GEM chamber assembled at GSI, Darmstadt, Germany is shown in Fig. 4.3. This chamber is also made using 10 cm×10 cm standard single mask GEM foils from CERN. The drift gap, transfer gaps and the induction gap of this GEM chamber are listed in Table 4.1. The anode readout PCB is segmented into 256 readout pads. The whole structure is placed inside a gas tight perspex box which is larger than the volume of the

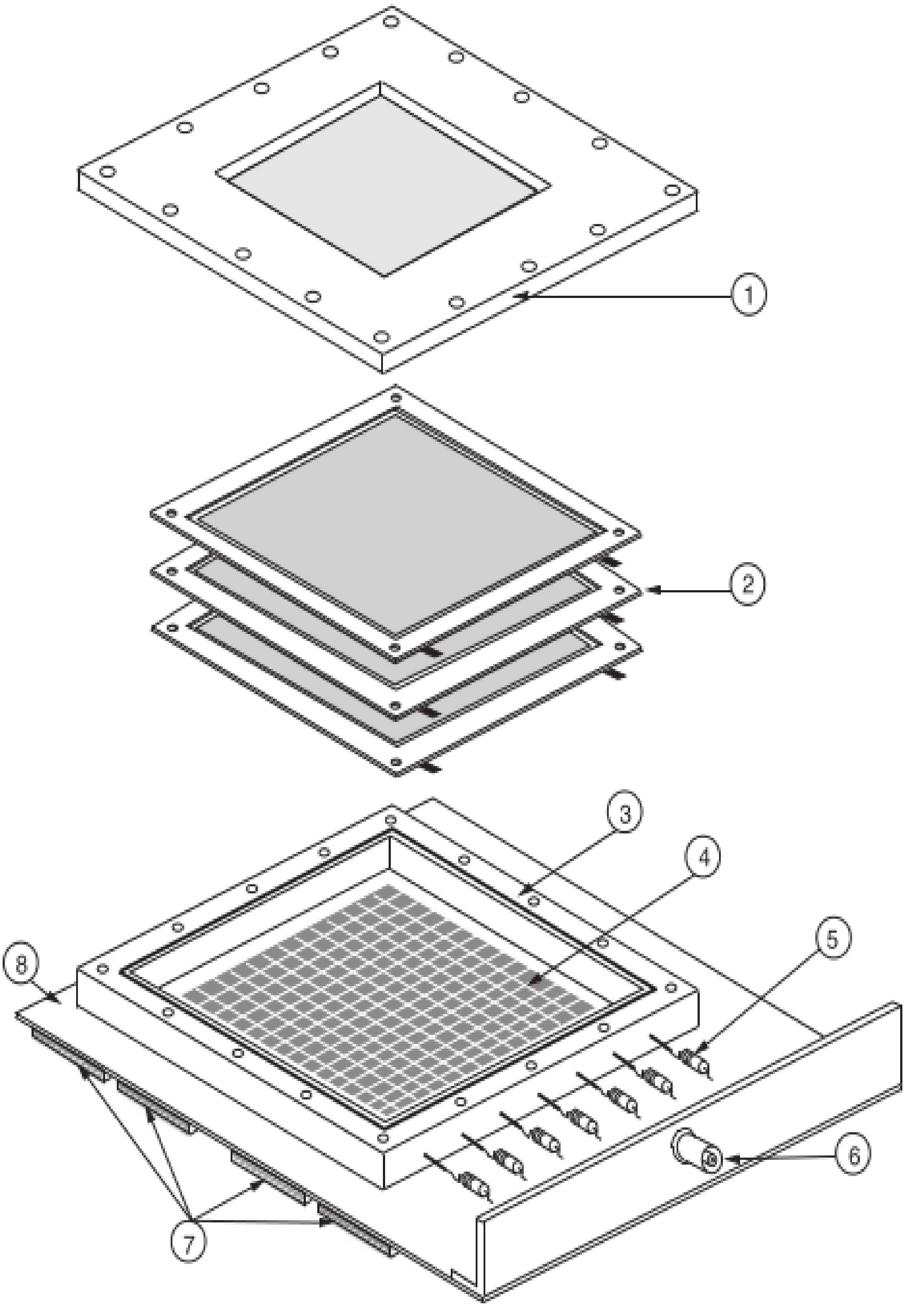

Figure 4.1: Schematic of assembly of a triple GEM chamber (1) top chamber lid with drift plane, (2) triple GEM foils stretched in FR4 frames, (3) gas tight housing frame with ‘O’ ring seal, (4) anode readout pads, (5) resistor chain for distributing the voltages, (6) SHV connector for bias, (7) input connectors to FEB and (8) readout PCB.

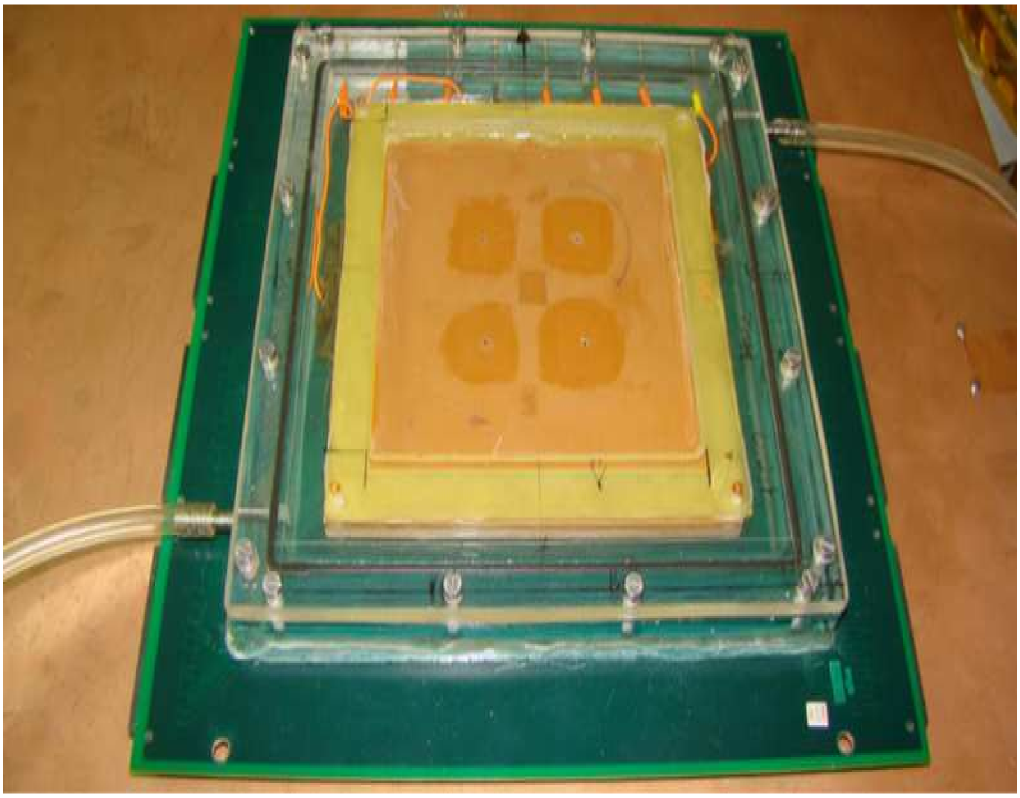

Figure 4.2: A 10 cm×10 cm GEM made at VECC

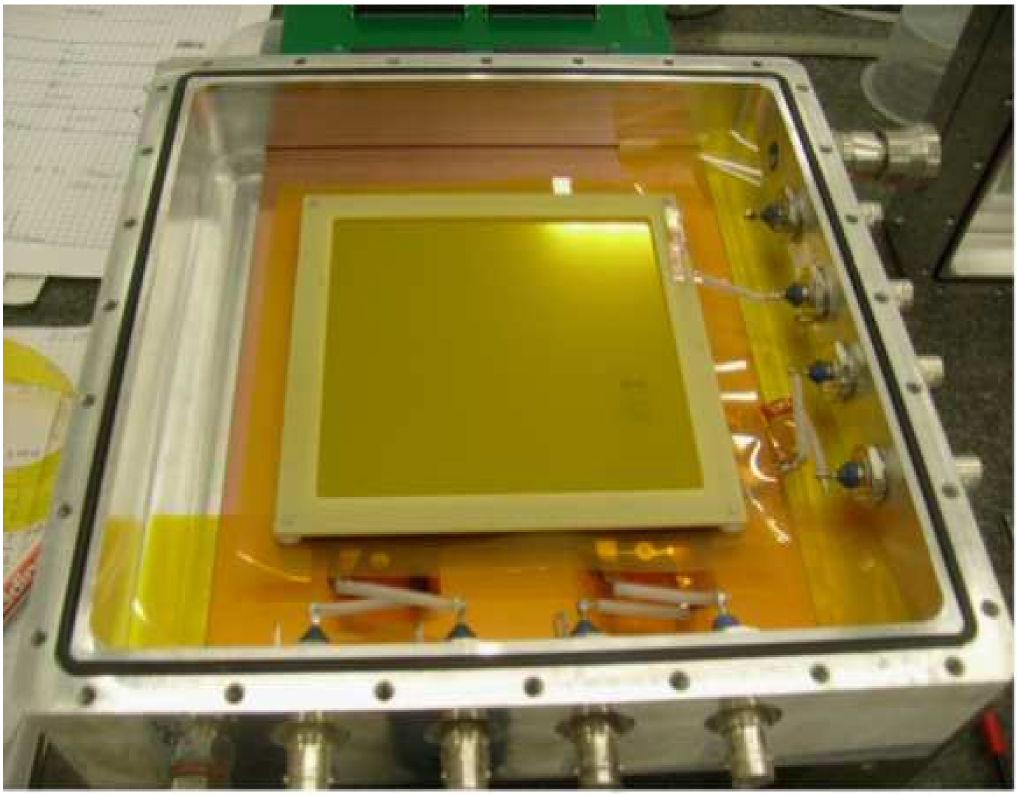

Figure 4.3: A 10 cm×10 cm GEM made at GSI

VECC chamber. The GSI-GEM chamber is powered via a resistor chain of protection resistance of 1 MΩ. The voltages across the three GEM foils (ΔV_{GEM}) are not same. For all the results, the high voltage (HV) for GSI-GEM was kept fixed at 3.7 kV. The voltages across the three GEM foils were 370 V, 336 V and 362 V. The corresponding drift, transfer and induction fields are 2.19 kV/cm, 3.29 kV/cm and 3.29 kV/cm respectively. The efficiency and the gain are measured using different sets of GEM voltages.

4.1.2 Data acquisition system

A good fraction of data might be missed during the selection of triggers during high rate operation of the detector. So the MUCH of CBM experiment will register all the hits above a pre-defined threshold. The threshold is set to avoid the noises due to electronics. So we need a trigger-less data acquisition system. In all test beam experiments using GEM, we have used nXYTER (neutron-X-Y-Time-Energy-Readout) [10] based readout system. nXYTER, a self-trigger readout system based on a 128-channel ASIC, developed as a part of EU-FP6 project DETNI [11]. This ASIC has two independent pulse-processing channels with different peaking times, the fast channel of 18 ns peaking time constant provides the time-stamp of the hit after the discriminator and the slow channel of 140 ns peaking time constant is used for signal amplitude measurement using a peak detection and hold circuit. The ASIC shows a time-jitter smaller than 4 ns for 8×10^3 electron input charge improving to 2 ns at 10^4 electron input. A nXYETR has 12-bit ADC of 25 fC dynamic range. It is placed on the FEB, each of which houses one nXYTER ASIC. The block diagram of the readout system is shown in Fig. 4.4, in which the detector is directly connected to the FEB. The data transfer and control operations are performed by a ROC board. One ROC board can handle at most two FEBs. During test beam, we used 4 FEBs controlled by 2 ROCs for VECC-GEM and 2 FEBs controlled by one ROC for GSI-GEM respectively.

4.1.3 Testing of the GEM prototype at laboratory

The VECC-GEM was tested using 5.9 keV X-ray from ^{55}Fe source at the laboratory. A premixed gas of Argon and CO$_2$, mixed in 70:30 ratio, was used. A spectrum of 5.9 keV X-ray from ^{55}Fe, obtained at the 10 cm$\times$10 cm VECC-GEM at ΔV_{GEM} = 398 V, is shown in Fig. 4.5.

The gain of the detector rises exponentially with voltage across the GEM foils (ΔV_{GEM}) as shown in Fig. 4.6. The gain of the chamber reaches $\sim 7\times10^4$ at $\Delta V_{GEM} = 412$ V.

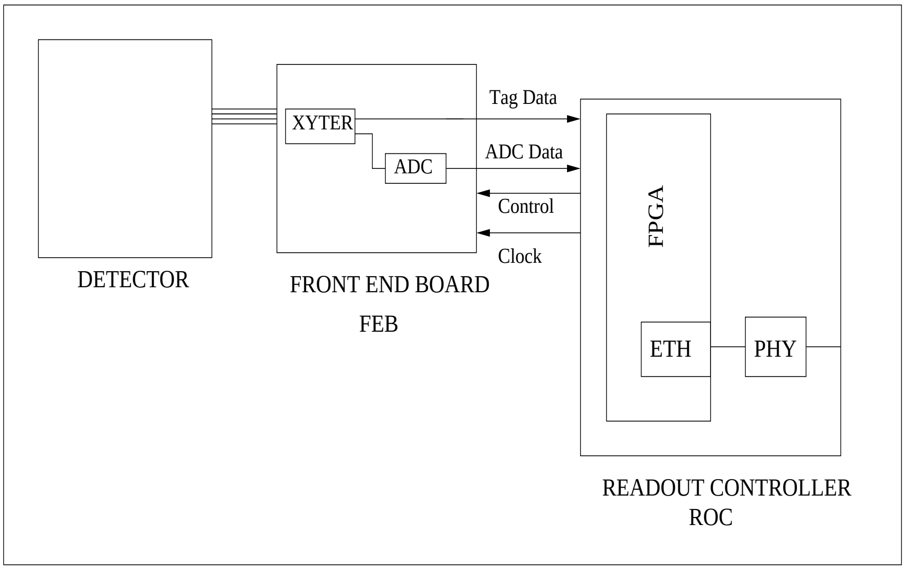

Figure 4.4: Block diagram of a nXYTER ASIC coupled to a detector

4.1.4 Testing of GEM using Pion beams

4.1.4.1 Experimental setup

The small size 10 cm×10 cm GEM prototype assembled at VECC (VECC-GEM) was tested along with four 10 cm×10 cm GEM prototypes made at GSI (GSI-GEM). The detectors were tested using pion beams of momentum 150 GeV/c at CERN SPS H4 beam line in 2012. The experimental setup is shown in Fig. 4.7.

There are five GEM detectors of size 10 cm×10 cm. GEM0 has 512 anode readout pads of dimension 3 mm×3 mm. Other GEMs are assembled at GSI and have 256 readout pads of size 6 mm×6 mm. In this test setup, there are two iron absorbers of width 20 cm and 80 cm at a distance 84 cm and 177 cm from the beam pipe end, respectively. A set of two crossed hodoscope scintillators (one vertically another horizontally) is placed in front of the beam. Another set is placed at the rear side of the setup. There is a finger scintillator before the GEM0 detector. A trigger signal is generated using the combination of the signals from the five scintillators (2 scintillators at the front, one finger scintillator, 2 scintillators at the rear). A GEM detector (GEM4) is placed at a distance 166 cm from the beam pipe end to test the spark-probability of GEM detector. Self-triggered readout system based on nXYTER ASIC was used for data acquisition.

4.1.4.2 Time correlation spectra

The distribution of the time difference between the coincidence trigger signal and hits on GEM prototype is the time correlation spectrum. A time correlation spectrum of GEM0 at a voltage (ΔV_{GEM}) of 300 V is shown in Fig. 4.8. The signals from the GEM detector will be correlated with the trigger but the noise will not be correlated. The shape of

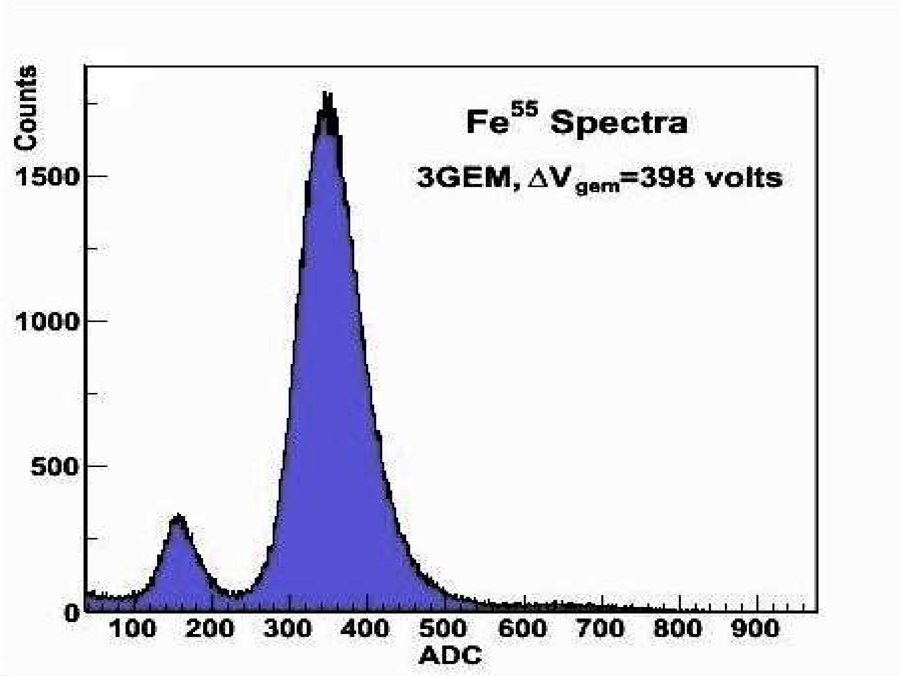

Figure 4.5: Spectrum of 5.9 keV X-ray from ^{55}Fe irradiated on VECC-GEM

the distribution is a Gaussian one. Almost no entries outside the peak region suggest that most of the hits on the GEM0 is related to the coincidence trigger signal. The σ of the distribution is related to the time resolution of the detector. The resolution will be better if we subtract the resolution of the scintillators. The σ of the time correlation are 13.5 ns with a mean value of 330 ns for ΔV_{GEM} = 300 V of the GEM0 detector. The position of the peak depends on the delay introduced by the data acquisition software and the cable delay. It should be noted that the actual time resolution would be better after the subtraction of the time-jitter due to the trigger scintillators. The hits within the time correlation window are taken only for analysis. For this analysis, we choose a time window of 200 ns. This will cover the full spectrum of the time correlation spectrum.

4.1.4.3 Beam spot on GEM detector

The X, Y position of the hits within the time correlation window are plotted to get a 2D beam spot on the GEM0 detector. The 2D distribution of the pion beams on GEM0 and GEM1 detector are shown in Fig. 4.9(a) and Fig. 4.9(b), respectively. The beam spots are clear without any further structures inside the beam. However, due to the narrow profile of GEM avalanche spot coupled to the Gaussian shaped beam profile, the beam spot seen on GEM0 is peaked around a few pads only. The beam seems to be narrowly focused and low lying pedestal corresponds to the overlap region of the trigger scintillators. Additionally, uncorrelated noise within the time-correlation window adds hits to the region beyond the trigger area, making the spread of the grass wider as shown in 4.8.

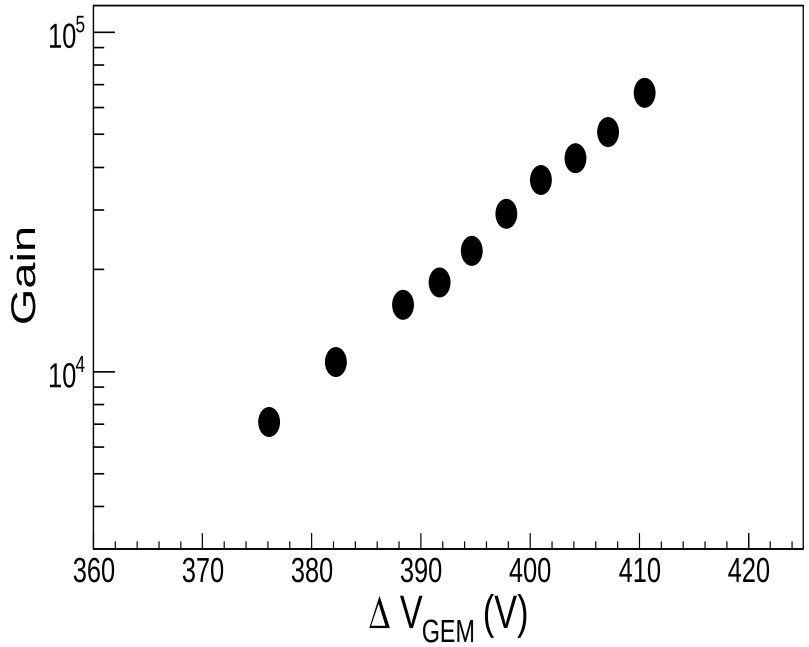

Figure 4.6: The variation of the gain of the VECC-GEM chamber as a function of ΔV_{GEM} using from ^{55}Fe X-rays source.

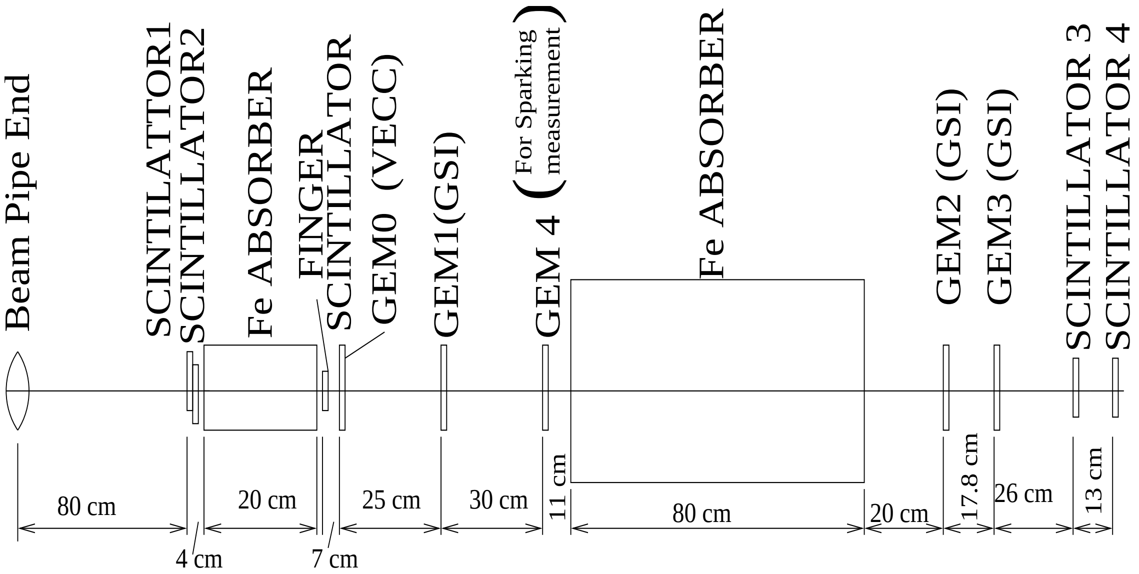

Figure 4.7: Experimental arrangements for testing small GEM prototypes at CERN SPS H4 beam line using pion beams.

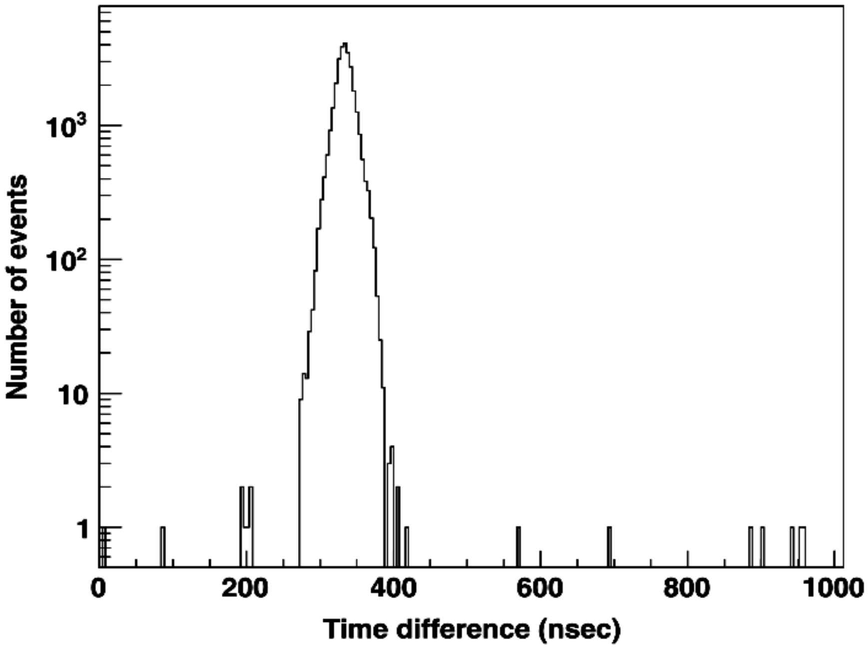

Figure 4.8: The time correlation spectrum of GEM0 at $\Delta V_{GEM} = 300$ V

4.1.4.4 ADC distribution and gain

The pedestal for a particular voltage setting is taken when the beam was switched off. The pedestal includes noises from the detectors and from the electronics. The corresponding ADC distribution is the pedestal distribution. In this test setup, a pedestal value of 2000 ADC has been taken for all the electronics channels included in this analysis. The ADC values of the pads around the pad with maximum hits are summed up to obtain the total ADC of corresponding to a particle for a particular ΔV_{GEM}. The event by event pedestal subtracted ADC distribution is shown in Fig 4.10 for GEM0 (VECC GEM) at $\Delta V_{GEM} =$ 323 V and GEM1 (GSI GEM) at ΔV_{GEM} of 370 V, 336 V and 362 V across the GEM foils, respectively. The distribution is fitted with Landau distribution function to extract the most probable value (MPV). Due to increase of ΔV_{GEM} the ADC distribution starts to saturate due to limited dynamical range of the nXYTER ASIC. The charge corresponding to the MPV value are calculated from the calibration of the nXYTER [12]. The charge is calculated using the charge calibration of the nXYTER and the formula is given by,

$$Q \;=\; 0.2025 + 20.53{\times}10^{-3}{*}A - 6.733{\times}10^{-6}.A^2 + 13.14{\times}10^{-9}.A^3 - 3.566{\times}10^{-12}.A^4 \tag{4.1}$$

where Q is in fC and A is in ADC LSBs. The calibration gives, 1 ADC = 0.025 fC. The gain of the detector is defined as, $\text{Gain} = \frac{Charge\ deposited}{Input\ charge}$,
The input charge is the charge of the primary electrons created in 3 mm drift gap for the minimum ionising particles. From the $\frac{dE}{dx}$ calculation the number of electrons created in Ar:CO_2 gas mixture (70:30 ratio) is found to be 30. The gain of the chamber is calculated

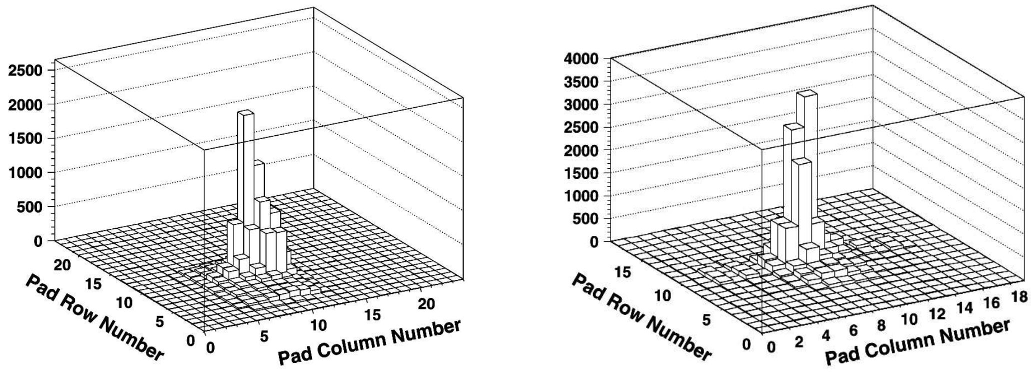

(a) (b)

Figure 4.9: a) Pion beam spot on GEM0 detector with 3 mm×3 mm anode readout pads, b) Pion beam spot on GEM1 detector with 3 mm×3 mm anode readout pads

up to $\Delta V_{GEM} = 350$ V for GEM0 (VECC GEM) as beyond this the ADC spectra became totally saturated. The MPV values at different ΔV_{GEM} are used to obtain the gain at different ΔV_{GEM} of the detector. The variation of the gain of the GEM0 chamber is shown in Fig. 4.11. The gain rises slowly at low ΔV_{GEM}, this may be due to nXYTER threshold and incomplete transition of the avalanche electrons through the holes. Then the gain increases exponentially and reaches 4000 at $\Delta V_{GEM} = 350$ V. With the present setup, an operating voltage corresponding to $\Delta V_{GEM} = 330$ V seems to satisfy the criterion of working GEM detector.

4.1.4.5 Efficiency

The efficiency of the chamber is defined as the number of particles detected at GEM divided by the total number of particles passing through the detector,

$$Efficiency = \frac{N_{Hit}|_{200\ ns}}{N_{Trig}}$$

where $N_{Hit}|_{200\ ns}$ is the number of hits that are recorded at GEM0 within 200 ns time correlation window and N_{Trig} is the number of trigger signals. The variation of efficiency with ΔV_{GEM} is shown in Fig. 4.12. The efficiency rises with ΔV_{GEM} and reaches almost 98 $\%$ at $\Delta V_{GEM} = 340$ V. For the operation of CBM-MUCH, an efficiency of $\sim 95\%$ for MIP is a prerequisite for detecting dimuon efficiently. It is also required that the efficiency should be uniform over the operating range of HV, particle rate and other operating conditions.

4.1.5 Track point resolution of GEM detector

The GEM detector of MUCH will be used for the purpose of tracking the muons. The tracks made by a particle on STS will be projected to MUCH for further extension. So

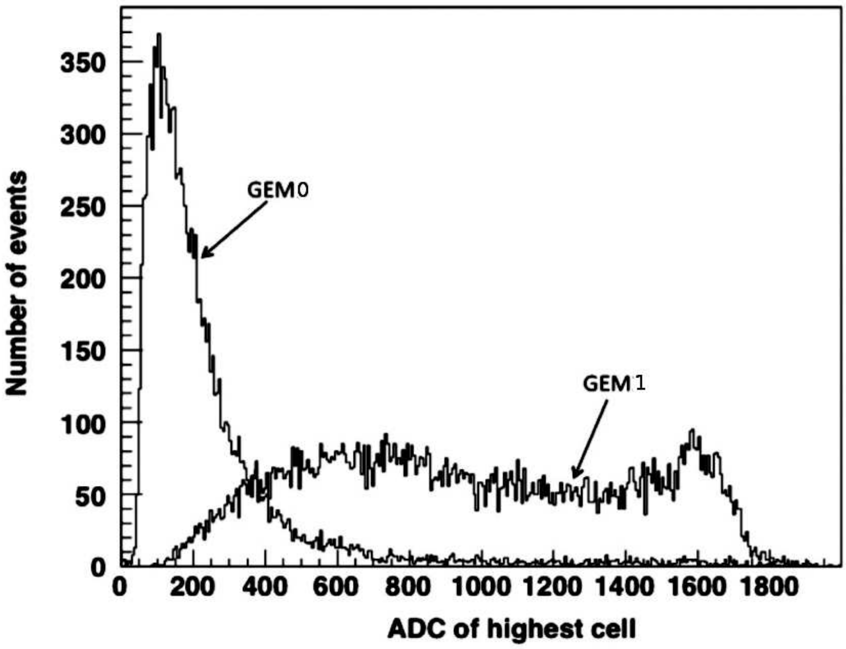

Figure 4.10: Event by event highest ADC spectra for GEM0 at $\Delta V_{GEM} = 323$ V and of GEM1 at ΔV_{GEM} for three gaps of 370 V, 336 V and 362 V.

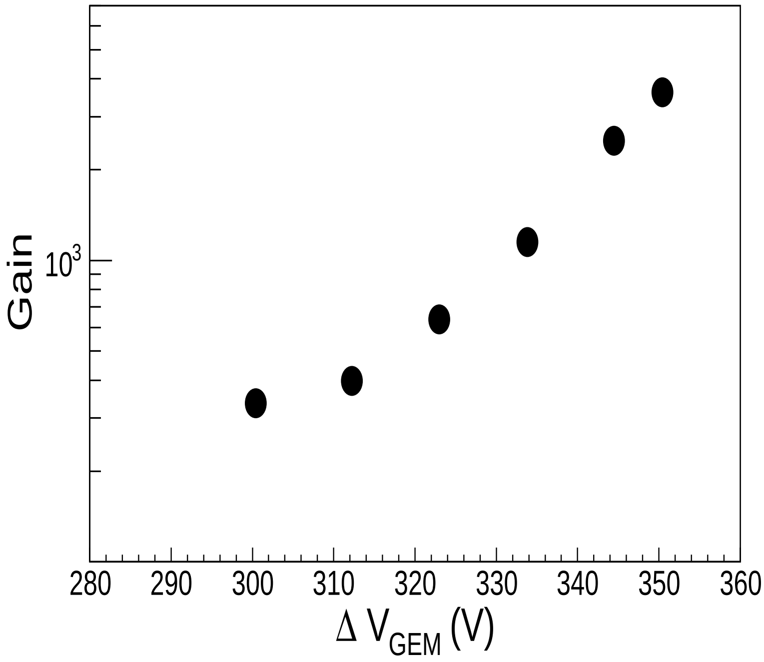

Figure 4.11: Variation of gain of the GEM0 detector with ΔV_{GEM}

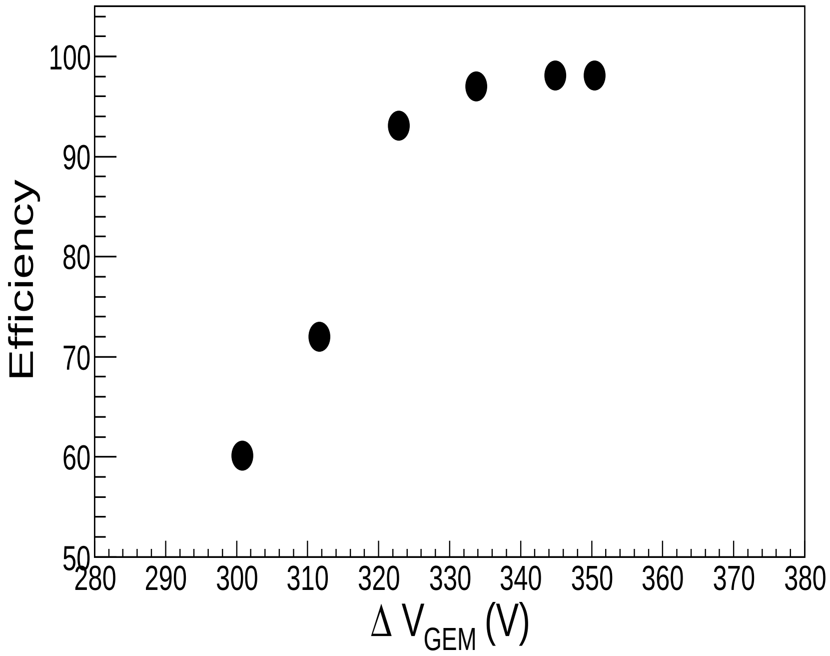

Figure 4.12: Variation of efficiency with ΔV_{GEM}

for this tracking detector, track point resolution or tracking residue is an important factor for reconstructing the track of a particle. The track point resolution is calculated for the GEM1 detector from this setup using the data from GEM0, GEM1 and GEM3. Data from other GEMs are not used for track residue calculations. In this analysis, first, the alignment of the 3 GEMs (GEM0, GEM1 and GEM3) were tested in the following method. A readout pad with maximum ADC in an event is chosen at GEM0. The ADC weighted mean x, y positions are determined from the distribution of the hits from large numbers of events. The mean value is,

$$x_{mean} = \frac{x_1 * ADC_1 + x_2 * ADC_2 + ...}{\Sigma ADC} \tag{4.2}$$

This mean value is subtracted from each hit in an event. This is done for all the GEMs. The events that have hit on the chosen pad at GEM0, GEM1 and GEM3 are used for tracking. As there is no magnetic field the track will be a straight line. So a straight line is drawn connecting the hits at GEM0 and GEM3. Then the corresponding x, y positions at GEM1 are calculated from the fit. The differences between the measured position and the fitted position are plotted for all the hits as shown in Fig. 4.13. The mean of this distribution gives the mis-alignment of the GEM1. The mean of the mis-alignment along X and Y axes are -0.403 mm and 0.019 mm respectively. The corresponding σ's are $\sigma_x = 0.23$ cm and $\sigma_y = 0.23$ cm respectively. The result shows that the mis-alignment is negligible compared to the pad size of the GEM1 (6 mm × 6 mm). Next, we have checked the track point resolution of the GEMs. Considering the nominal resolution of the pads, the position resolution follows $\sigma_{GEM1} = \sqrt{\sigma_{GEM0} + \sigma_{GEM3}}$ cm, where σ_{GEM0}

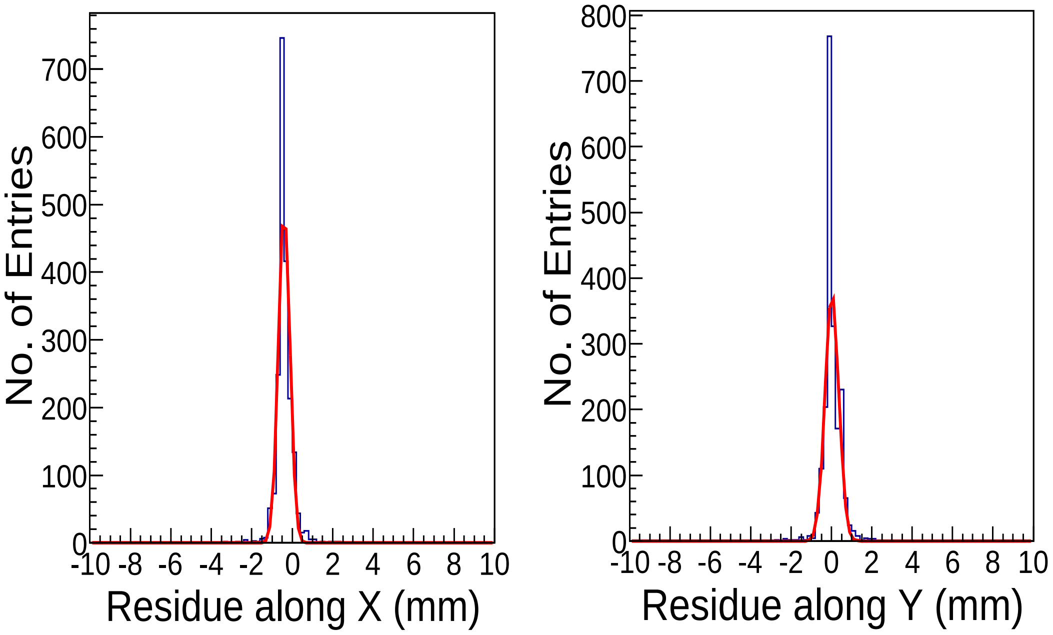

Figure 4.13: Residue of the track along X and Y direction.

and σ_{GEM3} are the the resolution of the GEM0 and GEM3 detectors. GEM0 and GEM3 have square pads of dimensions 3 mm×3 mm and 6 mm×6 mm respectively. Then,

$$\sigma_{GEM1} = \sqrt{\sigma_{GEM0} + \sigma_{GEM3}}\, cm = 0.19\, cm. \tag{4.3}$$

As per Fig. 4.13 and considering the nominal resolution of the pads the track point resolution follows,

$$Track\ Point\ Resolution = \sqrt{(\sigma_{avg})^2 - (0.19)^2}\, cm \ = \sqrt{0.0159}\, cm \ = 0.12\, cm \tag{4.4}$$

The extracted resolution is as per expectation from the pad size of the chamber [13].

4.2 R & D on intermediate size GEM prototype

The detector layers of the MUCH will cover the acceptance from ±5° *to* ±25° surrounding the beam pipe. To cover this acceptance, trapezoid shape GEM detector modules will be used. Within a layer of the detector station of MUCH, alternate GEM modules will be placed back to back to reduce the dead space of MUCH. For the first station of MUCH, 16 such modules will be used to cover the acceptance. For the second station, 24 such modules are needed. In the direction of building trapezoid shape triple GEM detector, we started our R & D using a 31 cm×31 cm GEM prototype. The active area of the detector is a trapezium whose parallel sides have length of 7.5 cm and 23 cm respectively and its height is 31 cm. The overall dimension of the prototype is 50 cm×47 cm. This prototype has 1196 readout pads. There are 23 pads along an annular side and 52 pads along radial side. One such prototype can cover 23° of azimuth. The size of the readout pads are 1° progressively increasing from 2.97 mm×2.97 mm to 11.21 mm×11.21 mm. The size of the pads are arrived at after detail calculations as mentioned in [14]. The readout channels from the readout pads are of different lengths depending on its position on the PCB.

4.2.1 Stretching and framing of the GEM foil

The 31 cm×31 cm GEM foils were stretched by gluing FR4 based boundary frame. Extra precautions were taken during stretching and framing for a precise work. Stretching of GEM foils of larger dimension are more difficult. The foils should be uniformly stretched without any mechanical sag. The edge frame of the detector is 1.5 cm wide and 1 cm thick. A thin supporting cross rib is placed between the foils as spacer. The area of the cross rib is minimized to reduce the dead space. Additional care has been taken so that there is no over-stretching, otherwise the opposite corners will be bent. The foils can be stretched mechanically or using thermal technique. Though this technique is more time consuming, is simple to follow. The GEM foil to be stretched, is sandwiched between perspex frames. The perspex jig is then heated using lamps as shown in Fig. 4.14. A temperature of 45°C with a deviation of 1°C was maintained using an appropriate arrangement of temperature controller. After a few hours, the foil became taut. A mixture of glue is made using Araldite epoxy adhesive and hardner mixed in 2:1 ratio. The glue

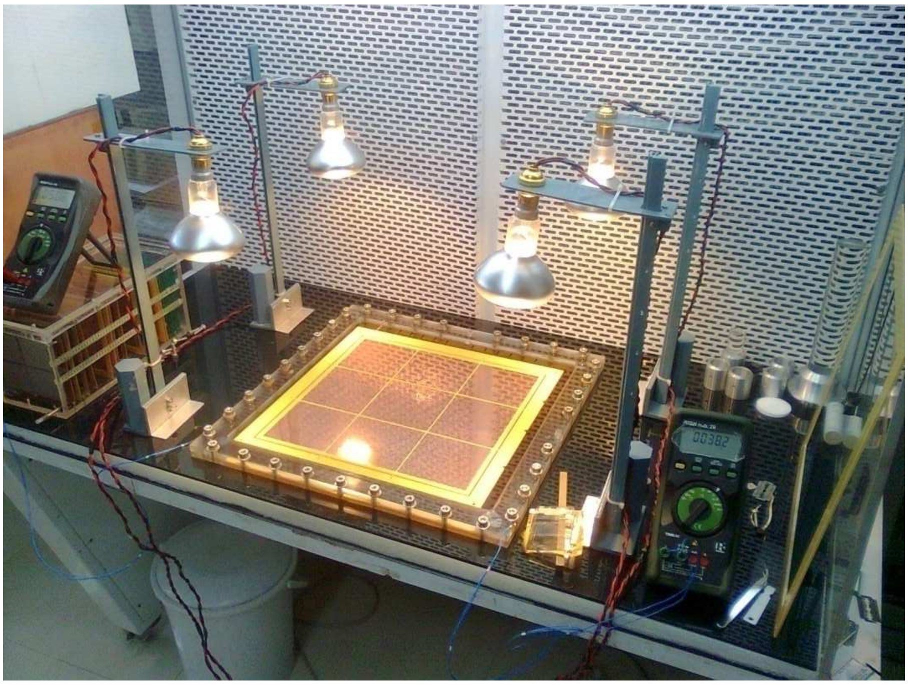

Figure 4.14: A GEM foil is under thermal stretching

is usable for 90 minutes. A thin layer of glue is then applied gently on the surface edge frame. The frame is then glued gently onto the stretched foil. The whole system is left undisturbed for 20 hours for curing.

4.2.2 Experimental setup

A prototype triple GEM detector of dimension 31 cm×31 cm was tested at COSY ion beam facility at Jülich University in Germany. A schematic diagram of the experimental test beam setup is shown in Fig. 4.15. There were two other 10 cm×10 cm triple GEM detectors (GEM1 and GEM2). The intermediate size GEM (GEM3 in the figure) was placed 210.4 cm from the end of the beam pipe. Three GEM detectors are used in this setup, but the main goal of this test was to study the performance of the trapezoidal size GEM (GEM3) for the first time.

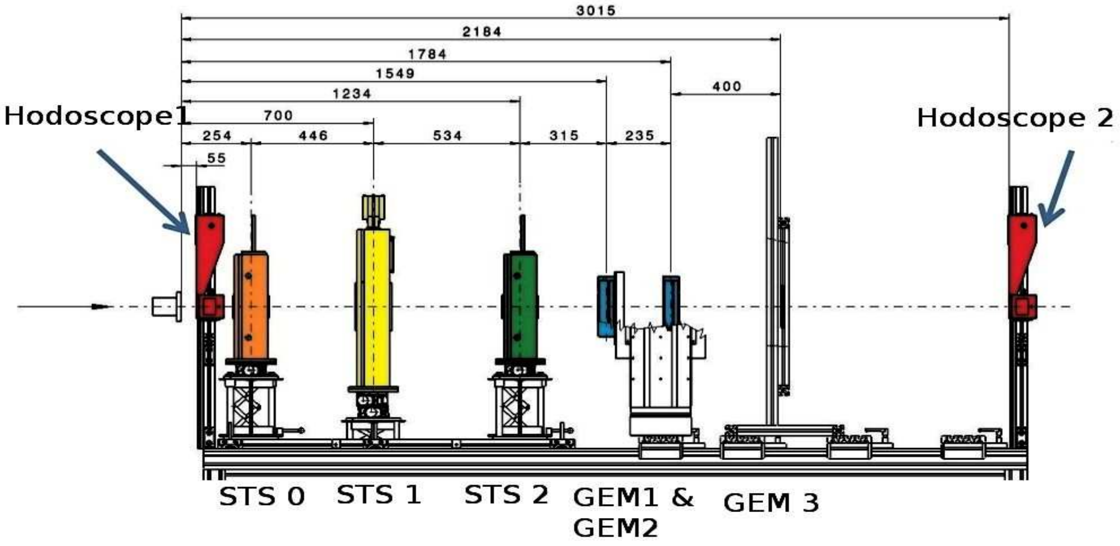

Figure 4.15: Test beam setup of 31 cm×31 cm at COSY in 2013.

A proton beam of momentum 2.36 GeV/c was used to test the performance of the detector. Data from the detectors are acquired using nXYTER based self-triggered readout system. Three prototype silicon tracking detectors (STS0, STS1, STS2) were also kept in the test bench for testing by other group. There was a set of two crossed scintillator hodoscopes in front of the setup. Another set of crossed scintillator hodoscopes was placed at the rear side of the experimental setup. A threefold coincidence of signals from front scintillator hodoscope, GEM2 and rear scintillator hodoscope has been chosen as the trigger signal for the intermediate size GEM. The nXYTER based self-triggered readout system was used to read the data from the detectors. 8 FEBs connected to 4 ROCs were used for acquiring the data from the detector.

4.2.3 Results

A data analysis frame work, GSI On-line Off-line Object Oriented (GO4) framework based on ROOT, was used. The data acquisition was controlled by using GO4 framework. The acquired data is analyzed using GO4 framework as well.

4.2.3.1 Time correlation spectra

In this self-triggered readout system, all the hits above a predefined threshold are digitized and stored. This reduces low voltage noise associated with the signal. The hits on GEM detector will have a definite time correlation with the trigger whereas the noise will not be. The distribution of the difference between the times of the trigger signal and the hits on the GEM detector will be referred as the time correlation spectrum. One such time correlation spectrum is shown in Fig. 4.16. The spectrum is fitted with Gaussian distribution function. The mean and sigma of the fit parameters are 849.5 nsec and 11.41 nsec respectively. A time window of 250 nsec is chosen around the mean value. Only the hits within the time correlation window are used for further analysis. Most of the hits are time correlated as seen in Fig. 4.16. There are few hits outside the fitted area but they are not considered for any calculations.

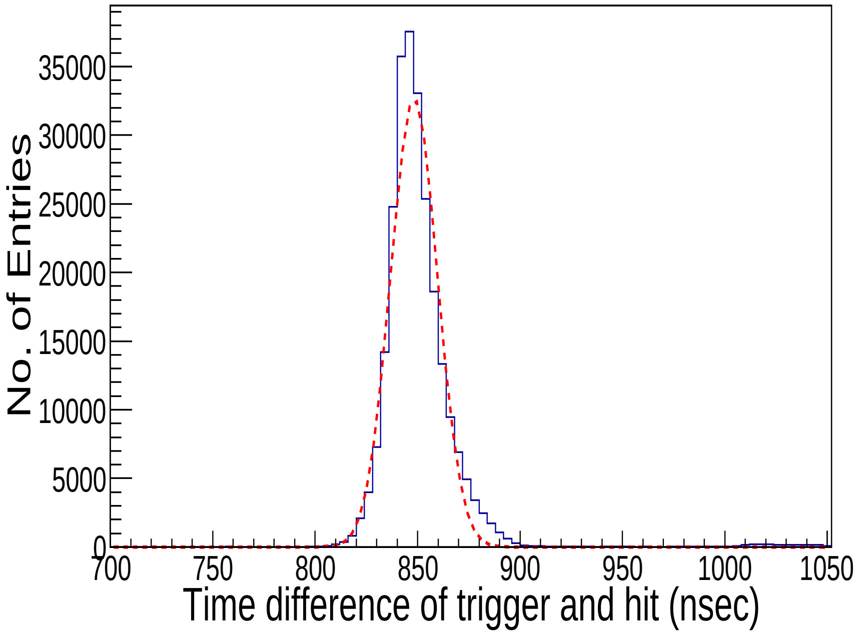

Figure 4.16: Time correlation spectrum of 31 cm×31 cm GEM at ΔV_{GEM} = 366.6 V fitted with Gaussian distribution (dotted line) with mean = 849.5 nsec and σ = 11.41 nsec.

4.2.3.2 Beam spot on GEM detector

The coordinates of the hits within the time correlation window are plotted to get the beam spot of the GEM. One such beam spot on the GEM3 detector is shown in Fig. 4.17. A clear beam spot is seen for the MIP without any structure inside the beam.

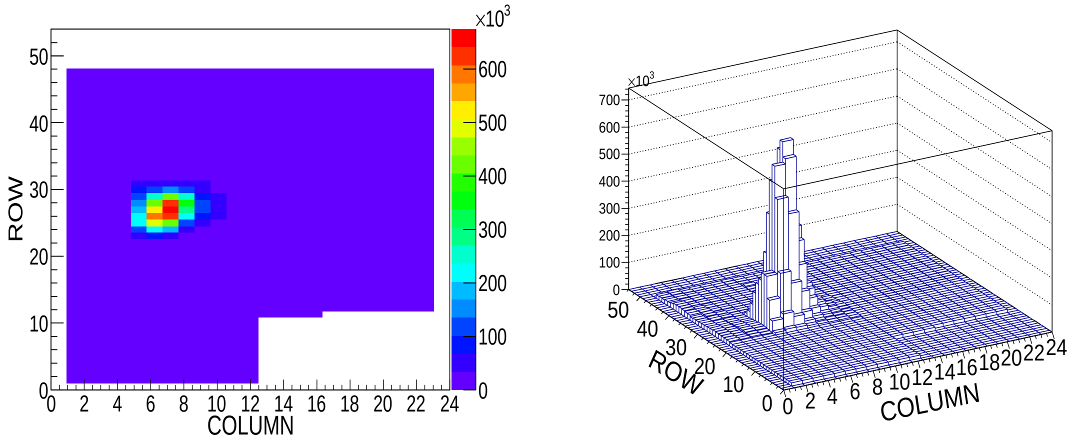

(a) (b)

Figure 4.17: The beam spots on the GEM3 detector (a) 2D beam spot, some region of the detector was not connected with electronics, (b) lego beam spot

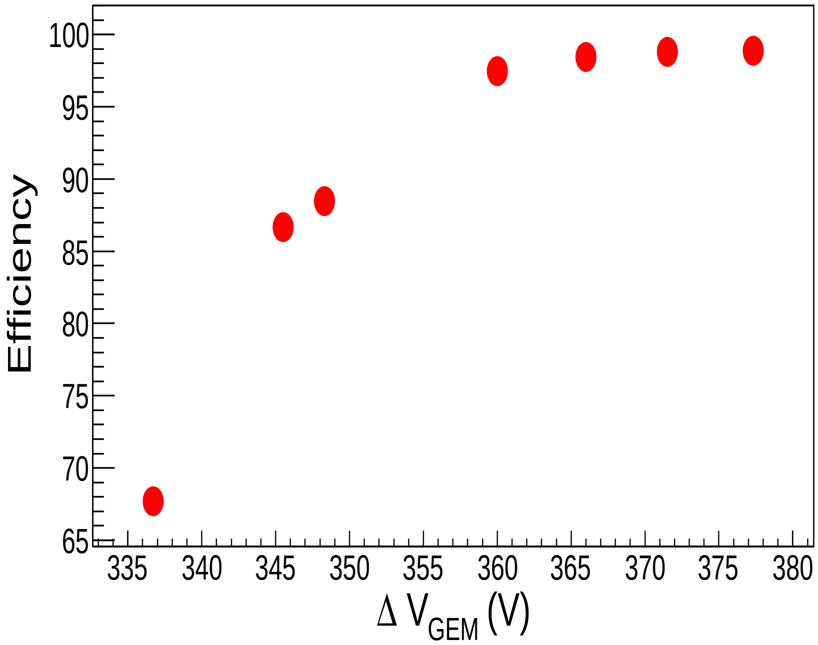

Figure 4.18: Variation of efficiency with ΔV_{GEM}.

4.2.3.3 Efficiency

Only the hits within the time correlation window are considered for efficiency calculation. The particles are considered to be detected if it has at least one hit in intermediate size detector (GEM3) within the time correlation window. The efficiency is defined as,

$$Efficiency = \frac{N_{GEM}}{N_{TRIGGER}} \tag{4.5}$$

where N_{GEM} = number of events having at least one hit at intermediate size GEM detector within the time correlation window and $N_{TRIGGER}$ = number of trigger signals. The trigger signals are the threefold coincidence of the signals from front scintillator hodoscopes, GEM2 and rear scintillator hodoscopes. The variation of efficiency with $\Delta\ V_{GEM}$ is shown in Fig. 4.18. The efficiency reaches >95% at ΔV_{GEM} = 366.60 V [15]. This efficiency is well above the pre-requisite value (>90 %) for the operation of MUCH to detect the muons efficiently.

4.2.3.4 Cell multiplicity

The beam is falling on few readout pads on the anode readout PCB. The number of such pads is called cell multiplicity for that event. The cell multiplicity around a region where readout pads are of dimension 6.92 mm×6.92 mm at ΔV_{GEM} = 366.30 V, is shown in Fig. 4.19.(a). Due to increase of ΔV_{GEM} the avalanche size increases resulting in a slight increase in cell multiplicity of the detector as can be seen from Fig. 4.19.(b).

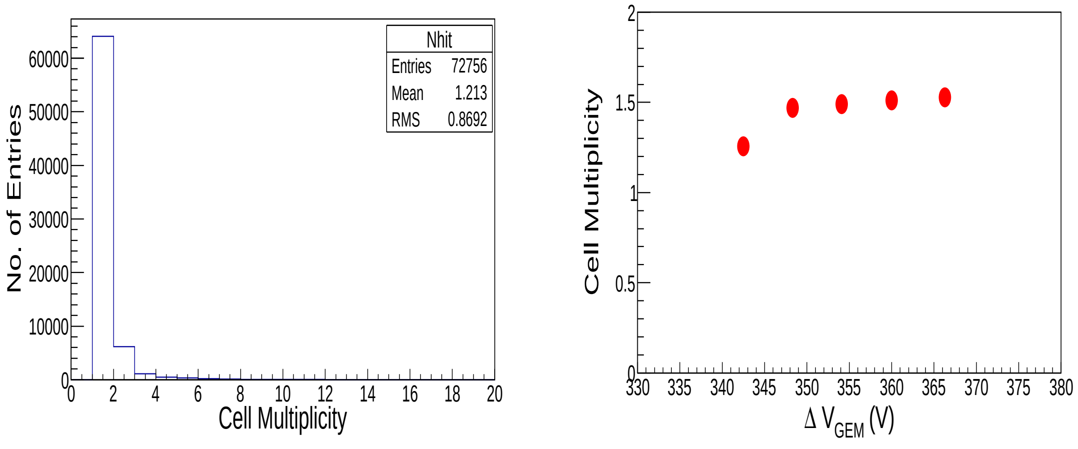

(a) (b)

Figure 4.19: a) Cell multiplicity at a region of pad size 6.92 mm×6.92 mm, average cell multiplicity is 1.20, b) Variation of cell multiplicity with $\Delta\ V_{GEM}$.

4.2.3.5 ADC distribution and gain

The pedestal subtracted event by event ADC distribution for the pad with highest hits fitted with Landau distribution function is shown in Fig. 4.20(a) for GEM3 at $\Delta V_{GEM} =$ 366.30 V. The ADC distributions at different ΔV_{GEM} were fitted with Landau distributions to find the MPV values. As the ΔV_{GEM} increases, the ADC distribution starts to saturate due to limited dynamic range of the nXYTER (25 fC). The calculation of gain is described in Sec. 4.1.4.4. The variation of the gain with ΔV_{GEM} of GEM3 is shown in Fig. 4.20(b). The results have been reported in CBM progress report 2013 [15]. Even after successful operation of the 10 cm × 10 cm and 31 cm×31 cm, two main criteria of their use in MUCH remains incomplete, namely, large size triple GEM detector and the rate handling capability of it.

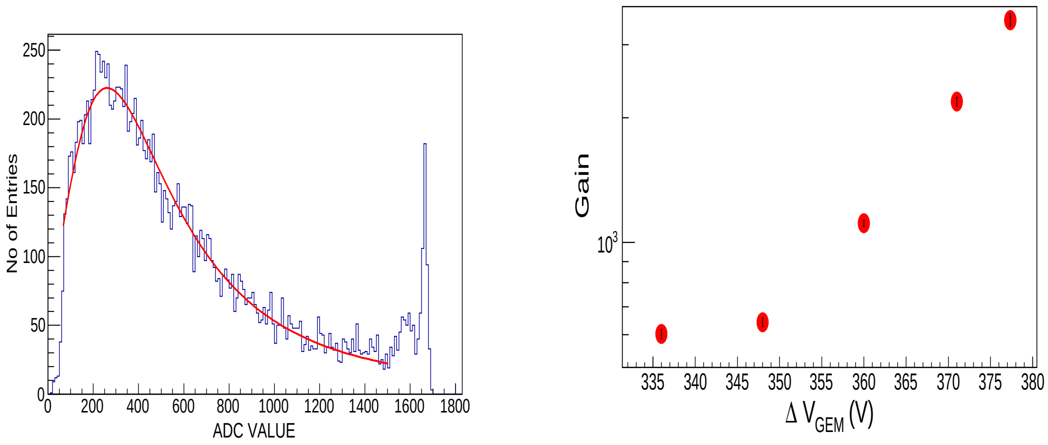

(a) (b)

Figure 4.20: (a) Event by event pedestal subtracted ADC spectrum on the readout pad with highest hits for GEM3 at Δ V_{GEM} = 366.3 V, (b) Variation of gain with Δ V_{GEM}.

4.3 R & D on large trapezoid shape GEM module

A large prototype trapezoid shape triple GEM module suitable for the 1^{st} detector station of MUCH has been assembled. The active are of the prototype detector is 708 mm long along radial side and the inner (outer) ring width is 100.2 mm (381 mm). For stretching the GEM foils, NS-2 technique (No Stress, No Spacer) [16, 17] was used instead of gluing and thermal stretching as discussed earlier. It is a new technique developed at RD51 collaboration, CERN for stretching large GEM foils by mechanical way. The GEM foil is divided into 24 high voltage sections in its upper surface to provide voltage across GEM foil. The high voltage segmentation of the GEM foil is shown in Fig. 4.21. The area of the four inner most sections are 25 cm^2 and the rest have area of 100 cm^2. The

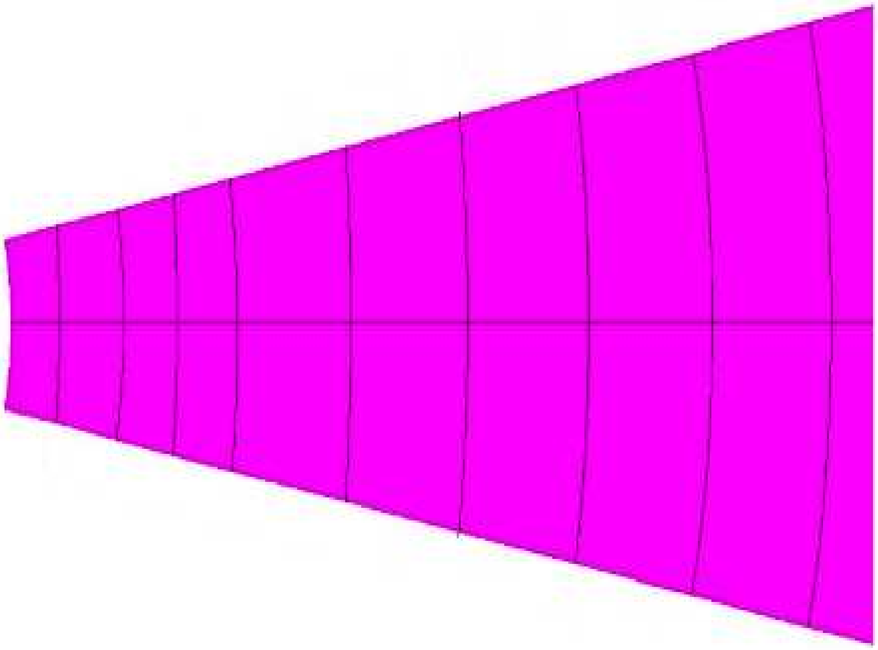

Figure 4.21: HV segmentation of the GEM foil on its top surface, only a part is shown with 20 segments.

sections are connected via surface-mounted protection resistance of 1 MΩ. Four zones are grouped, each having 6 sections. Separate resistance chain was used to power the four zones independently. A voltage divider circuit is used to distribute the voltage across the GEM foil. The resistances are so chosen that the voltage differences between top and bottom copper planes (ΔV_{GEM}) are same for all the three GEM foils. The drift gap, transfer gap and the induction gap of the GEM are 3 mm, 1 mm, 1.5 mm respectively. The readout anode PCB is an eight layered PCB to accommodate the tracks from each readout pads. The size of readout pads are progressively increasing starting from 3.96 mm$\times$ 3.96 mm to highest 16.6 mm $\times$ 16.6 mm at the edge. The way of pad segmentation is chosen so that the readout pad density is higher at the central region where the size of the readout pad is smaller. The multi-hit probability and the cost of detector are reduced drastically in this method. The full size large GEM chamber is shown in Fig. 4.22. This chamber will cover 23° azimuthal angle. To cover the full acceptance, alternative GEM modules will be placed back to back. There will be $\frac{1}{2}^{\circ}$ overlap between two chambers. With 23°, the readout anode PCB has 23 pads along an annular ring and 79 pads in a column. So there are total 1817 pads in the readout PCB. The PCB is divided into 15 readout regions. Each region will be read out by a FEB that can read 128 channels.

4.3.0.6 Assembly of the chamber

Special care has been taken to build the large chamber, particularly for stretching of large size GEM foils and proper layout of the tracks to accommodate the variation in occupancy

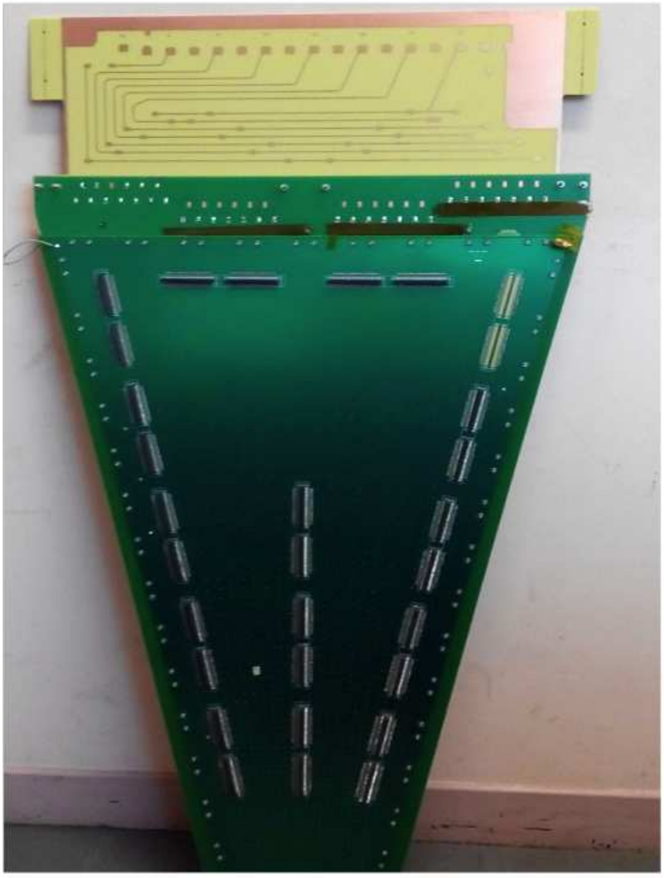

Figure 4.22: The large GEM chamber with the resistances for HV connection.

of the anode readout pads. The NS-2 technique technique of stretching has the special advantages that the damaged foils can be easily replaced, no permanent gluing or thermal stretching is required so the foil could be reused. It also takes less time for stretching. The steps, followed for assembling a large GEM chamber, are shown in Fig. 4.23.

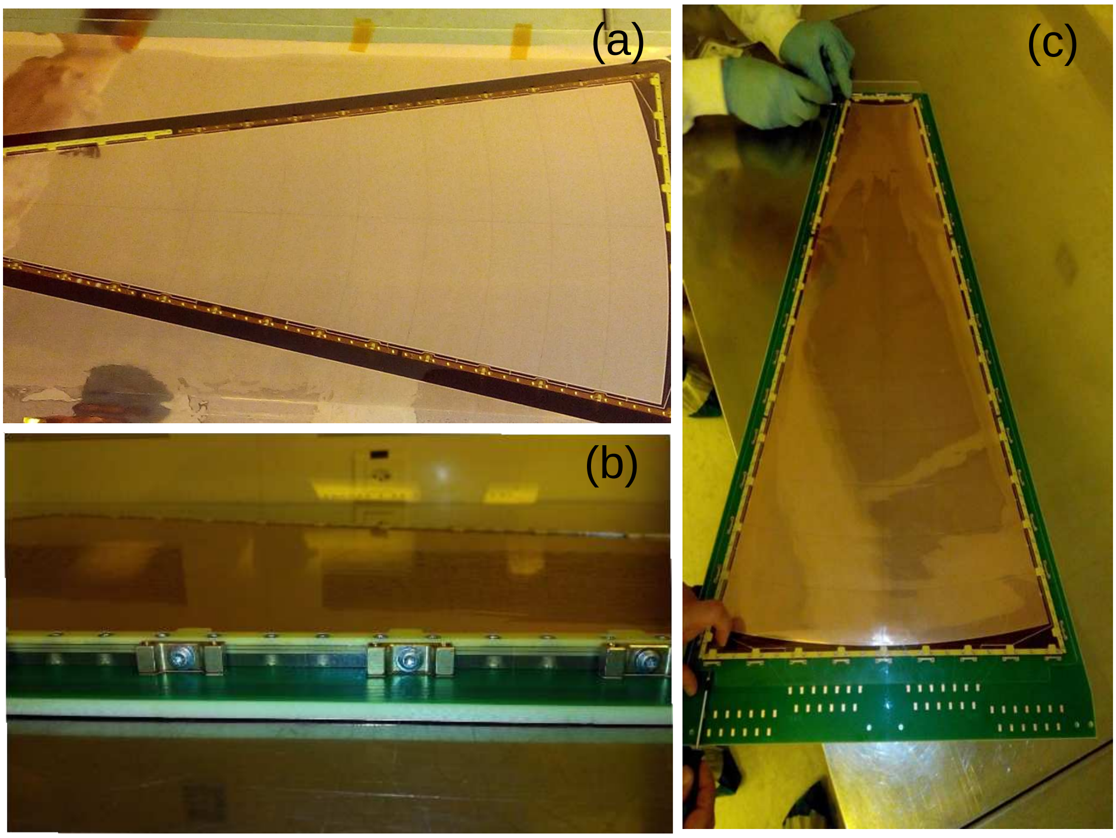

Figure 4.23: GEM foil stretching using NS-2 technique, (a) special inserts (yellow colors) are connected at the sides of the drift foil to create space for assembly of GEM foils (b) brass pins are fixed on the anode readout PCB for support pillars (c) mechanical stretching of the foils by tightening the screws.

First, small brass pieces with holes at prescribed intervals are fixed at the boundaries of the drift plane at regular intervals. The foil will be stretched against this brass pieces that act as the support pillars. A spacer frame of thickness 1 mm, is placed between two foils to provide transfer gap of thickness 1 mm. There are metallic pins soldered on the drift plane and passing through the spacers, make contact with the respective GEM foils. An induction gap of thickness 1.5 mm is made using spacer frame. After this the trapezoid shaped anode readout plane is placed. The chamber is sealed using O rings made of rubber. The mechanical stretching is done by making the screws tight with screw-driver. In the same way, all the screws inside pins are tightened to make the GEM foils taut. The screws are pulled out the foils against the support pins and the GEM foils became taut under this tension [18]. After this the chamber is cleaned in an ultrasonic bath for some minutes. The chamber is dried using an oven and put under Ar:CO_2 gas flow.

4.3.1 Experimental setup

The large triple GEM prototype was tested along with 3 STS detectors at COSY, Jülich University, Germany using proton beam of momentum 2.36 GeV/c. A premixed gas of Ar:CO_2 in 70:30 ratio is used. The intensity of the beam was regulated by adjusting the collimator window. The broadening of the beam size was done in some of the runs by using a wire mesh in front of the beam. A schematic diagram of the setup of the experiment is shown in Fig. 4.24.

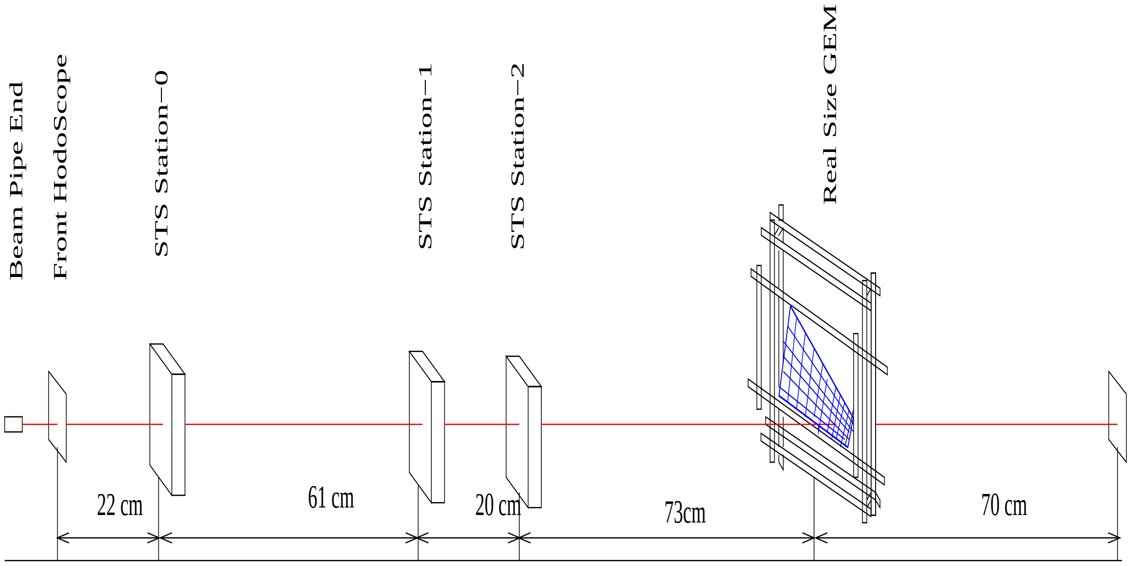

Figure 4.24: A schematic diagram of the test set at COSY using large GEM detector module.

4.3.2 Results

4.3.2.1 Time correlation spectra

A coincidence between the signals from front and rear hodoscopes is chosen as the trigger signal to the GEM detector. Data were acquired in self-triggered mode using nXYTER based electronics. A noise threshold corresponding to 1 fC is used for an optimised signal in the detector. All the hits above a predefined threshold are considered for analysis. The beam particles detected at the GEM detector must have a time correlation with the trigger signal. The distribution of the time difference between the time-stamps of the trigger signal and the hit, is the time correlation spectrum. A time correlation spectrum for $\Delta V_{GEM} = 371.8$ V is shown in Fig. 4.25(a). The spectrum is fitted with Gaussian distribution with a mean at 990.0 nsec and $\sigma = 13.71$ nsec. The position of the mean depends on the delay introduced by the electronics and the delay due to cables. It is clear from

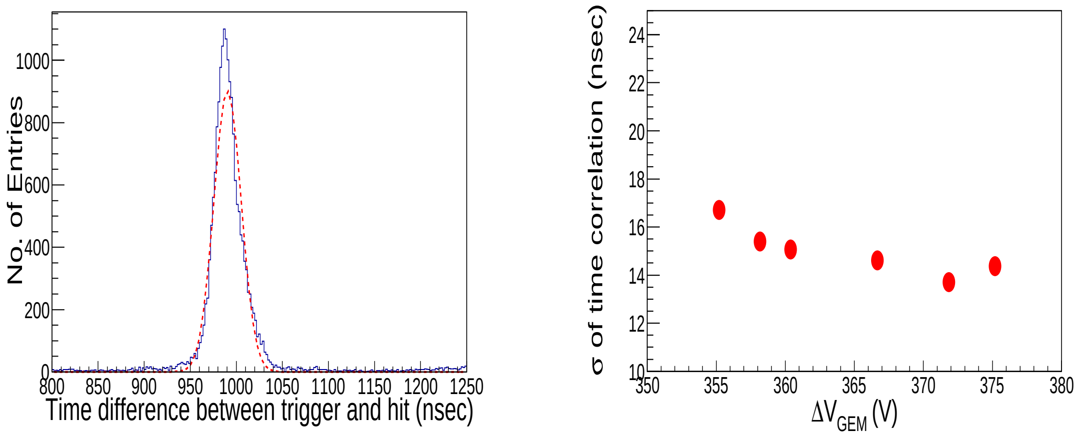

(a) (b)

Figure 4.25: (a) Time correlation spectrum of trigger signals and hits on GEM detector (solid line), the histogram is fitted with a Gaussian distribution function (dotted line), (b) Variation of σ of time correlation with ΔV_{GEM}.

the figure that most of the hits on GEM are correlated with the beam particles, though there are few hits outside the correlation peak. The σ of the distribution is related to the time resolution of the detector folded with the resolution of the scintillator hodoscopes. Since the time resolution of the hodoscopes is better than 5 ns, the contribution from the hodoscopes are negligible. The variation of the σ of the time correlation with ΔV_{GEM} is shown in Fig. 4.25(b). The value of σ reaches a minimum of 13.71 nsec at ΔV_{GEM} = 371.8 V.

4.3.2.2 Proton beam spot

The distribution of the hits on the large GEM is shown in Fig. 4.26 for $\Delta V_{GEM} = 371.8$ V at a region where the dimension of the pads are 7.39 mm×7.39 mm. The distribution of hits is confined within few pads only.

4.3.2.3 Beam Spot on Hodoscope

The beam spot at the rear hodoscope is shown in 4.27. The size of the beam is determined from its size on hodoscopes. The X and Y projection of the beam spot are shown in Fig. 4.28. The 1D projections are fitted with Gaussian distribution function. From the fit parameters, we get σ of the X, Y projections from the fitting. The σ values are $\sigma = 2.15$ mm, $\sigma = 7.58$ mm for X, Y projections ,respectively. The average σ is 3.52 mm, so the area of the beam is 12.42 mm^2. The average rate of the beam particles is estimated by calculating average time from first 100 aux signals. The average time is then subtracted from the average of the next 100 aux signals. Hence,

Average Rate = (10^8/subtracted value) in kHz.

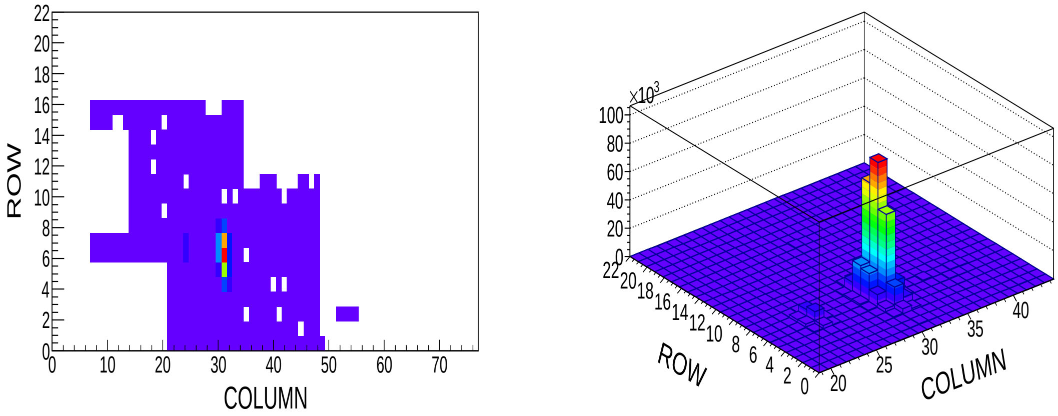

(a) (b)

Figure 4.26: Proton beam spot on GEM detector at the region of pad size 7.39 mm×7.39 mm : (a) 2D colour beam spot, only the region where beam region is covered by readout electronics, (b) lego beam spot.

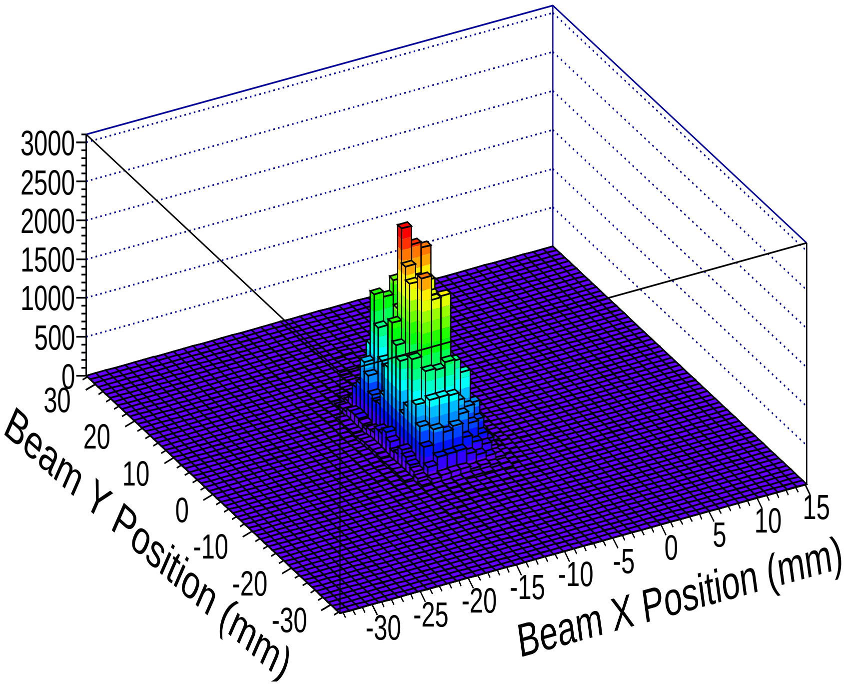

Figure 4.27: X, Y distribution of hits on Hodoscope.

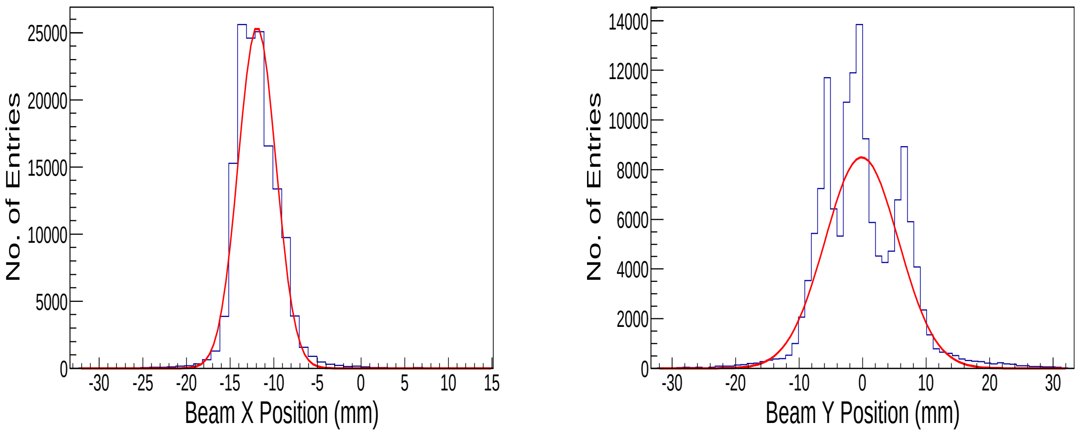

(a) (b)

Figure 4.28: Proton beam spot on rear hodoscopes : (a) projection of the beam spot along X axis, (b) projection of the beam spot along Y axis.

One such distribution of rate is shown in Fig. 4.29.

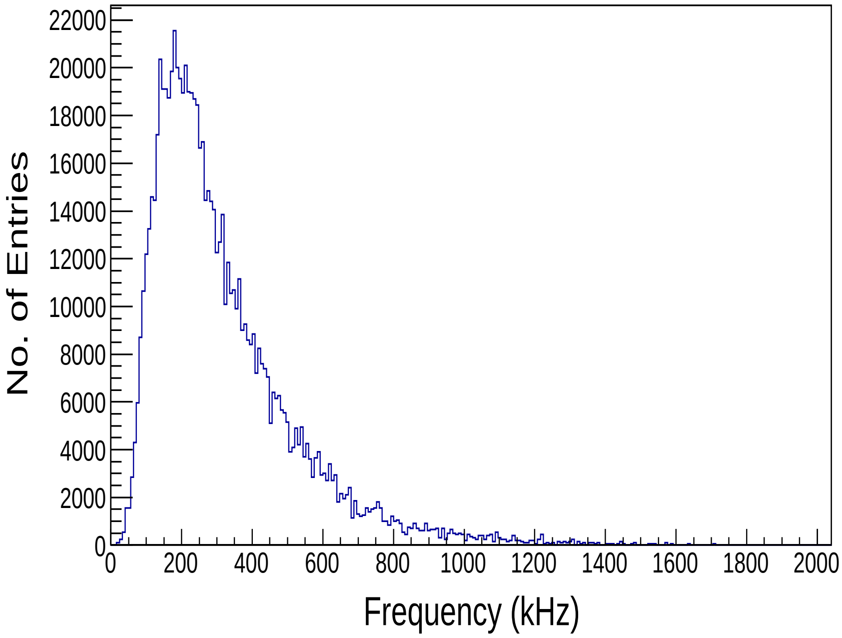

Figure 4.29: Frequency spectra of proton beam for $\Delta V_{GEM} = 375.2$ V.

4.3.2.4 Cell multiplicity

The cell multiplicity is calculated using the time correlated hits only. Fig. 4.30(a) shows the cell multiplicity plot for $\Delta V_{GEM} = 366.67$ V at a region where the cell size is 5.46

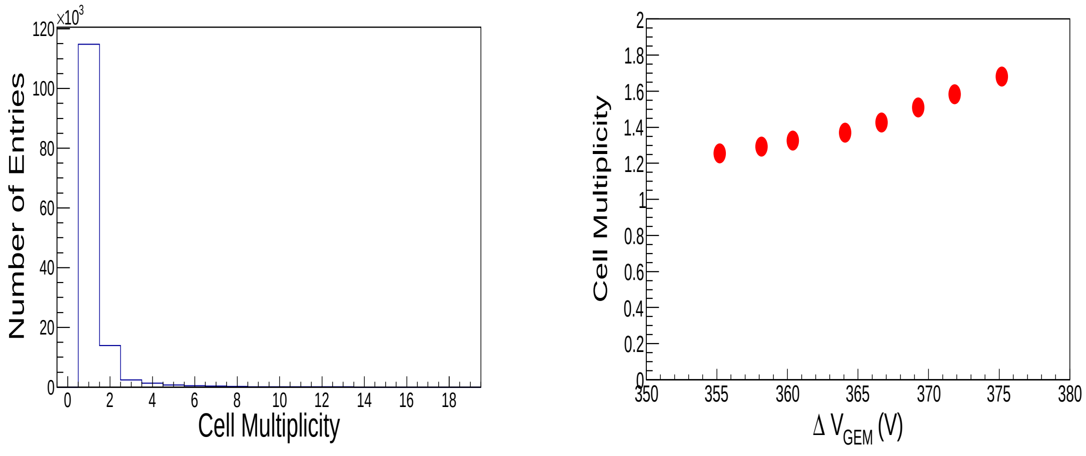

(a) (b)

Figure 4.30: (a) Cell multiplicity distribution for ΔV_{GEM} = 355.20 V, (b) The variation of cell multiplicity with ΔV_{GEM} at ΔV_{GEM} = 355.20 V at a region where pad size is 5.46 mm$\times$ 5.46 mm.

mm$\times$ 5.46 mm. The average cell multiplicity slowly increases with the ΔV_{GEM} from 1.256 at ΔV_{GEM} = 355.20 V to 1.681 at ΔV_{GEM} = 375.18 V at the same region as shown in Fig. 4.30(b). As the voltage across the GEM foils increases, the gain increases, resulting in an increase of transverse size of the beam.

4.3.2.5 Efficiency

As the GEM detector is aligned with the hodoscopes, the particles that have correlated hits on both sets of front and rear hodoscopes are taken as the incident particles to the GEM. Particles are considered to be detected at GEM if it has at least one hit on the GEM chamber within the time correlation window. The ratio of the number of particles detected at GEM and the number of triggers is the efficiency of the GEM detector. The variation of efficiency with ΔV_{GEM} is shown in Fig. 4.31(a) for four sets of time correlation window of 2σ, 3σ, 4σ, 5σ. The variation of efficiency with time correlation window for a particular ΔV_{GEM} suggests that a time correlation window of 3σ seems to be an optimum choice. The efficiency rapidly increases with ΔV_{GEM} and an efficiency of $\sim$ 96% is obtained at ΔV_{GEM} = 375.2 V [19, 20]. The CBM-MUCH will be used in high interaction rate so efficiency is required be stable at high rate of beam particles. The efficiency for a time correlation window of 3σ at different rates of the beam particles are plotted in Fig. 4.31(b). The efficiency at a fixed ΔV_{GEM} = 375.2 V are plotted up to 350 kHz. The area of the collimated proton beam is calculated from its spot on the hodoscopes. The beam makes a spot of size 12.42 mm^2 on the hodoscopes. So the rate of particles per cm^2 for a beam of average rate of 350 kHz is 2.85 MHz/cm^2. This rate is

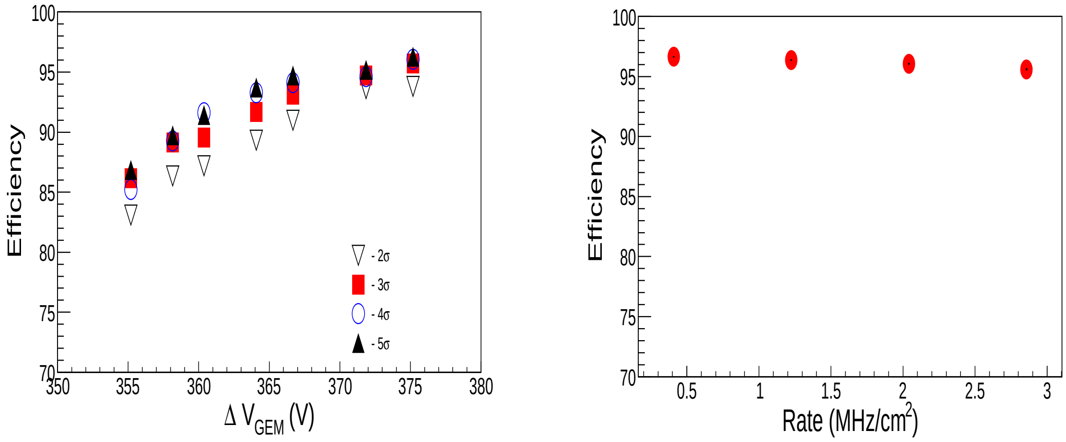

(a)

(b)

Figure 4.31: (a) Variation of efficiency of the detector with ΔV_{GEM} for different σ of time correlation window. (b) Variation of efficiency with the rate of incoming particles at 3σ of time correlation spectra at $\Delta V_{GEM} = 375.2$ V.

.

well above the rate, the first MUCH detector has to face. As the rate of particles increases efficiency is almost uniform with a slight decrease ($\sim 2\%$) above 2 MHz/cm^2.

4.3.2.6 ADC distribution and gain

In this setup a new method is used for pedestal subtraction. The method is the auto calibration of the pedestal. In this method the pedestal values are taken during the beam instead of stopping the beam. This is a method to acquire pedestals in pauses between taking physical data (in pauses between the beam spills, or periodically, every few tens of seconds or minutes). Pedestal is recorded either between two spills or periodically every few tens of seconds or minutes. In the data sample the pedestal data is separated from the physical data with special calibration marker messages. This marker indicates that nXYTER is going to be switched from one state to another (from self-triggered mode for taking physical data to externally-triggered mode for pedestal measurement, or vice versa). The pedestal distribution at a particular readout channel is shown in Fig. 4.32. The distribution is a Gaussian one, the mean values for each channel are stored in a text file and are used to subtract the pedestal from the signal. Channel by channel variation of the pedestal is shown in Fig. 4.32 for ΔV_{GEM} =366.67 V. The average value of the pedestal varies around 2000 ADC unit. The pedestal does not change significantly with the readout channels. No significant change has been observed in the average pedestal value due to increase of ΔV_{GEM}.

The ADC of the hits registered on GEM for an event are summed to get the total ADC in a cluster. The event-by-event ADC distribution after subtracting the pedestal

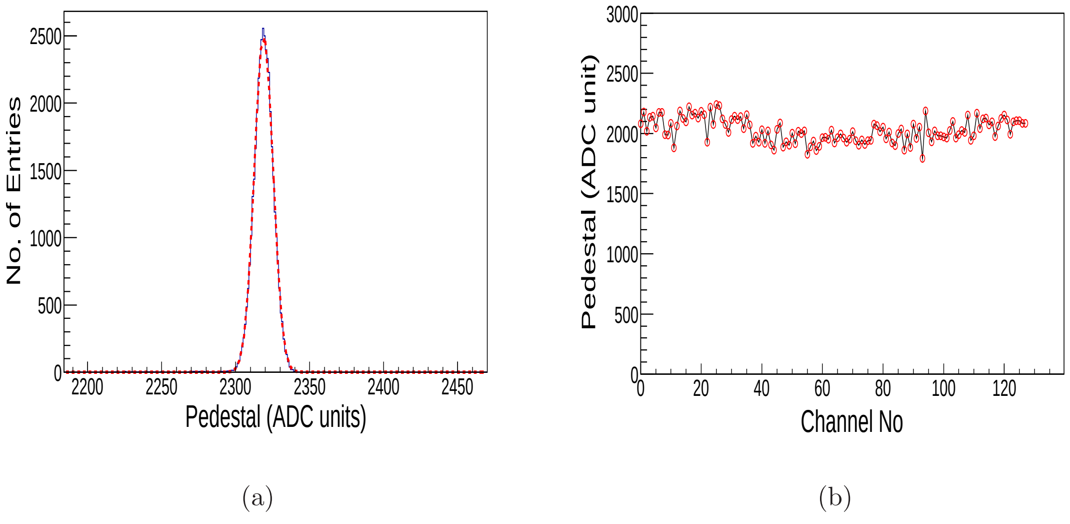

(a) (b)

Figure 4.32: (a) The pedestal distribution for ROC-0, FEB-2, Channel no. 10 of a nXYTER for ΔV_{GEM} =366.67 V, (b) The variation of the average pedestal for 128 channels of ROC-0 0f FEB-2 at same ΔV_{GEM}

.

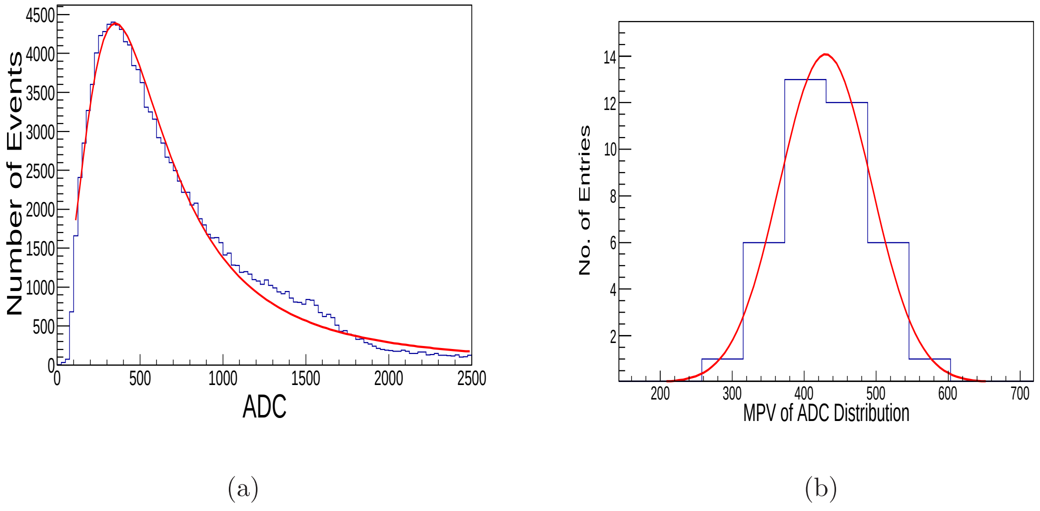

(a) (b)

Figure 4.33: (a) Pedestal subtracted cluster ADC distribution on GEM, (b) Uniformity of MPV of ADC distribution for different channels at ΔV_{GEM} = 369.3 V.

is shown in Fig. 4.33(a) for ΔV_{GEM} =366.67 V. The Landau distribution function is used to fit the distribution to find the MPV. The MPV value for this ADC distribution is = 386.64 ADC unit. The ADC distribution starts to saturate at higher ΔV_{GEM} due to limited dynamic range of the nXYTER. The MPV values of ADC distributions are obtained for eight sets of ΔV_{GEM} of GEM foil. From the $\frac{dE}{dx}$ calculation of proton beam of momentum 2.36 GeV/c in 3 mm drift gap in Ar:CO_2 gas in 70:30 ratio, the number of primary electrons are taken as 30. The gain is calculated in the same way as discussed in Sec. 4.1.4.4. Channel by channel variation of the gain of the chamber is studied for 39 different channels situated at different regions of the detector where the area of the pads are different. The gain looks reasonably stable over different parts of the detector with a spread of about $\sim$ 12% as shown in Fig. 4.33(b). The gain of the detector varies exponentially with ΔV_{GEM} following the expression,

$$Gain = A.e^{\alpha.\Delta V_{GEM}},$$

where A is a constant and α is a parameter that depends on temperature (T) and pressure (P) of the gas. In this experimental setup the temperature and pressure inside the cave was not changed significantly. No correction of the gain due to variation of temperature and pressure is studied. The variation of the gain of the large GEM prototype with ΔV_{GEM} is shown in Fig. 4.34(a). The gain of the detector needs to be uniform over a wide range of rate of particles for stable operation of the detector. The gain of the detector is calculated for different rate of the particle up to 2.85 MHz/cm^2. The variation of the gain is uniform up to 1.2 MHz/cm^2, but it shows fluctuation $\sim$ 9% at even higher rate.

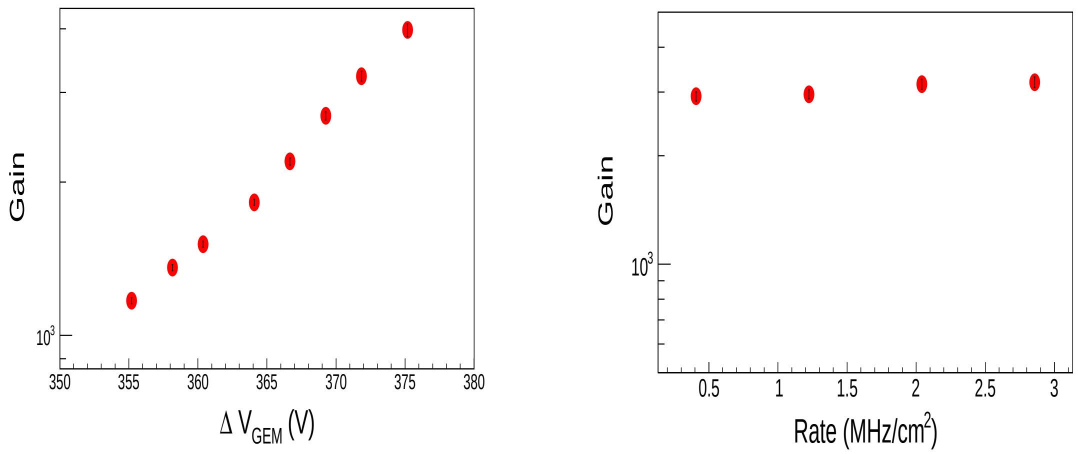

(a) (b)

Figure 4.34: (a) Variation of Gain with ΔV_{GEM}, (b) Variation of Gain with rate of incoming particle.

4.4 Long-term stability test of triple GEM prototype

The performance of the GEM detector may be degraded due to ageing for long-term operation in harsh radiation environment in any heavy ion collision experiment. The study of the long-term stability of a GEM detector is thus important before using GEM based detector in any experiment. The study of the long-term stability has been performed with a triple GEM detector.

4.4.1 Description of the GEM prototype

A triple GEM prototype has been assembled at RD51 laboratory [21, 22] using three standard single mask 10 cm × 10 cm GEM foils. The drift gap, 2 transfer gaps and the induction gap are 3 mm, 2 mm, 2 mm and 2 mm, respectively. The Kapton window is placed 11 mm above the drift plane. A negative HV supply is used to power the GEM chamber. A voltage divider network is used to supply high voltage (HV) across the GEM foils. The anode readout plane has a XY printed board in the base plane. There are 256 tracks in each X and Y direction. Each of the 128 tracks are connected to a 128 pin connector. In total, 4 such connectors are used. Instead of recording signals from individual strips, the signals from 128 strips are summed up with a sum-up board. 4 sum-up boards are used for the readout. The lemo output of the 4 sum-up boards are again added. The total current is then measured with a 6485 Keithley pico-ammeter.

4.4.2 Experimental set-up for ageing study

A schematic of the experimental setup is shown in Fig. 4.35. A Fe^{55} X-ray source is used to irradiate the GEM chamber. A jig is made to place the source on the top of the GEM chamber. The diameter of the source is 7.3 mm. A hole of same diameter is made on the jig for the X-ray to pass through. A particular position of the detector is irradiated in this set-up. A premixed gas of Ar:CO_2 in 70:30 volume ratio is used inside the GEM chamber. A gas flow meter is used to maintain a constant flow of gas at a rate of 3 lt/hr. The HV divider resistance chain is used to distribute the voltages to the GEM foils. A constant negative HV of -4300 V is applied to the drift plane. The input current from the HV supply is measured from the monitor of the HV supply. The voltages across the GEM foils and different gaps are calculated from the known value of the resistances and the current from the HV supply. For a HV supply voltage of -4300 V, the electric fields inside the drift, transfer, induction gaps are $\sim$ 2.4 kV/cm, 3.6 kV/cm and 3.6 kV/cm respectively. The voltage difference across 3 GEM foils (ΔV_1, ΔV_2, ΔV_3) are 395 V, 360 V and 320 V, respectively.

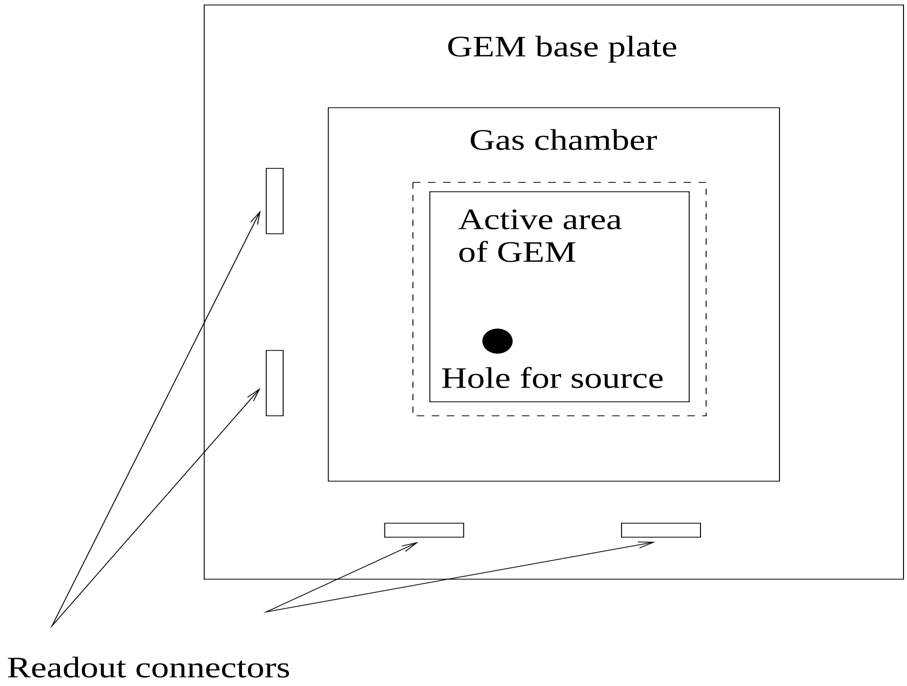

Figure 4.35: The setup for ageing study. The base plate has dimension of 25 cm × 25 cm. The gas tight edge frame has an area of 20 cm × 20 cm. The jig is shown by a dotted rectangle of area 10.5 cm × 10.5 cm. A hole is made on the jig for the X-ray to pass through.

4.4.3 Experimental results

The number of signal pulses from the readout plane is counted using a counter. A Fe^{55} X-ray source is used as the source of radiation. In order to study the stability of the gain of the detector, the current corresponding to the signal is measured with the source and without the source continuously. The technique is similar to the technique used earlier [23, 24] using an 8 keV Cu X-ray generator and Sr^{90} beta radioactive source. The anode currents are measured at an interval of 15 minutes. The anode current without source corresponds to the noise associated with the signal. The gain of the GEM detector depends on the temperature and pressure of the detector. In this regard, the temperature(T in °C), pressure (P in mbar) and the relative humidity (RH in %) are continuously measured with a data logger, built in-house with a time stamp. The variation of the output anode current is shown in Fig. 4.36 as a function of time with and without the radioactive source. The noise corrected anode current is given by,

$$i_{source} = i_{withsource} - i_{without\ source} \tag{4.6}$$

where $i_{withsource}$ and $i_{without\ source}$ are the anode current with and without the radioactive source, respectively. The gain of the GEM detector can be estimated from the

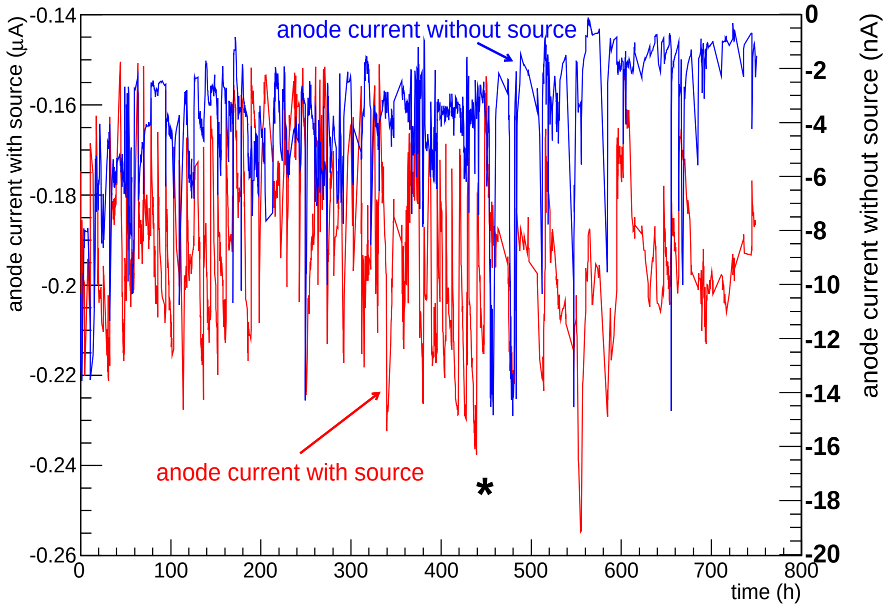

Figure 4.36: The anode current variation with time with and without the radioactive source. A star mark in the variation indicates change of the gas cylinder.

following formula,

$$Gain = \frac{i_{source}}{R * n * e} \tag{4.7}$$

where R is the count rate of the signal, n is the number of primary electrons and e is the electronic charge. The number of primary electrons, created in 3 mm drift gap in Ar : CO_2 gas mixture for 5.9 keV X-ray from Fe^{55}, is taken as 212. A full list of number of particles created in different gas mixtures can be found in [25]. The radioactive source has a half-life of 2.7 years, so the activity of the source should be modified accordingly. So the count rate of the signal is modified as,

$$R = R_0 \exp \frac{-0.693.t'}{t_{\frac{1}{2}}} \tag{4.8}$$

where R_0 is the initial rate and taken as 350 kHz and $t_{\frac{1}{2}}$ is the half-life of Fe^{55} radioactive source. The gain of GEM detector is related to the temperature and pressure by the following relation [26],

$$G(T/P) = A \ \exp{(B\frac{T}{p})} \tag{4.9}$$

where A and B are the two parameters. The variation of the $\frac{T}{p}$ corrected gain with the time is shown in Fig. 4.37. Here T ($= t + 273$) is in Kelvin and P (p in mbar/1013) is in atmospheric pressure. The variation of the gain with $\frac{T}{p}$ is fitted with an exponential function to calculate the parameters A and B. The value of A and B calculated from the fit are 75.37 ± 2.541 and 0.0181 ± 0.0001 atm/K. Now using the value of the fit parameters,

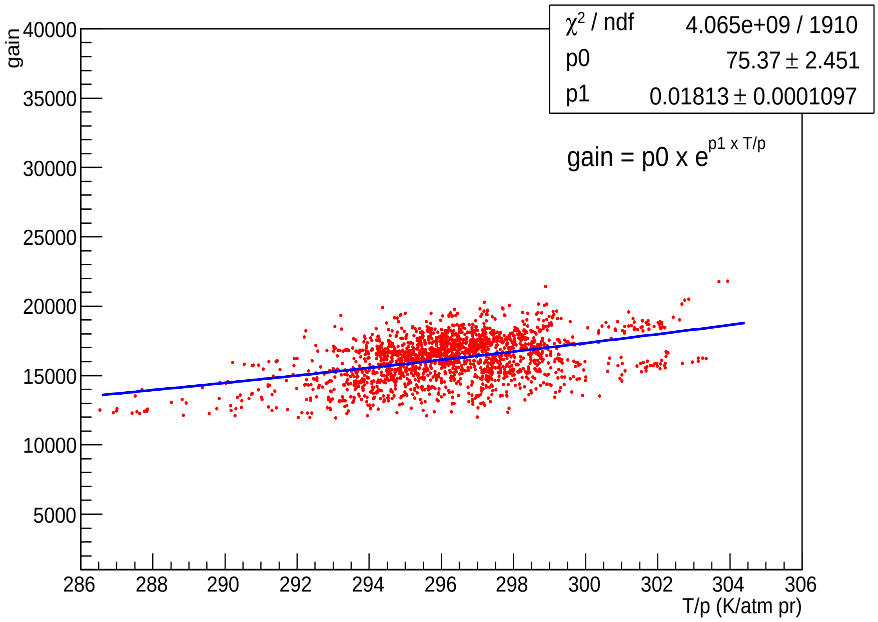

Figure 4.37: The variation of the $\frac{T}{p}$ corrected gain of the GEM prototype with the total time. The * mark in the plot indicates the change of the gas cylinder.

the normalised gain is obtained as,

$$Gain_{normalised} = \frac{Gain_{measured}}{A\exp\left(B\frac{T}{p}\right)} \tag{4.10}$$

The variation of the normalised gain with the charge accumulated per unit area is shown in Fig. 4.38. The variation has been shown up to a charge accumulation per unit area of 12 mC/mm^2 [27]. Though there are some small fluctuations in the normalised gain, the gain is not decreasing gradually or any such trend of decrease of gain is observed. No significant ageing is observed after an accumulation of charge of 12 mC/mm^2.

The normalised gain is also stable with some small fluctuation about the mean value. The intrinsic gain of the detector may vary up to 25 $\%$ due to variation of the geometry of the detector and also due to inhomogeneity in the gap sizes of the GEM as mentioned in [28, 29]. But in this case, a particular position is irradiated with X-ray radiation. So variation of gain due to inhomogeneity of geometry and gap size does not affect the results.

The normalised gain of the detector is plotted in Fig. 4.39. The distribution of the gain is fitted with a Gaussian distribution function whose mean is around 1.003 and a σ of 0.086. The normalisation due to temperature and pressure does not reduce the spread in the gain distribution. The left-over spread is significantly large with respect to the variation due to the varying T/P.

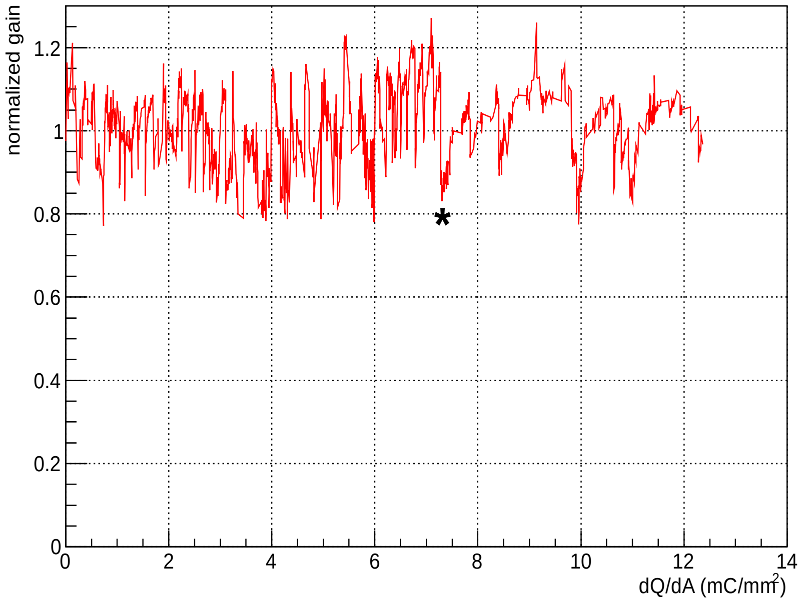

Figure 4.38: The variation of the normalised gain as a function of the charge accumulated per unit area. The * mark in the plot indicates the gas cylinder has been changed.

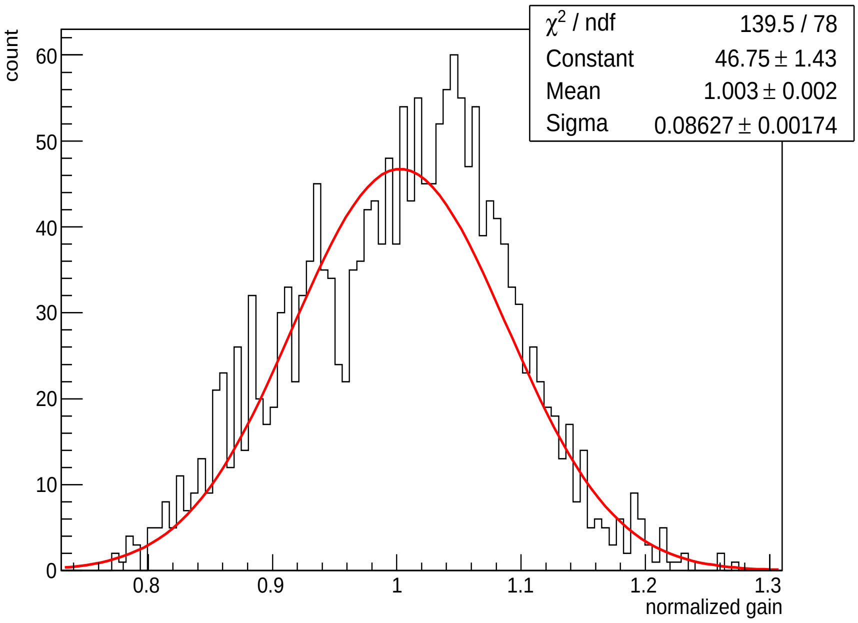

Figure 4.39: The distribution of the normalised gain of the detector. The distribution is fitted with a Gaussian distribution function with mean at 1.003 and a σ of 0.086.

4.5 Summary

R&D on GEM detector for the MUCH detector has been started by assembling a 10 cm× 10 cm triple GEM prototype using standard GEM foils exported from CERN and testing it in laboratory using radioactive source and using ion beams. The detector has been tested with efficiency $> 95\%$ for ΔV_{GEM} = 340 V. But the GEM modules to be used in constructing MUCH detector, are trapezoid in shape. So a triple GEM prototype of area 31 cm × 31 cm has been constructed which has a trapezoid shape active area. The prototype has been successfully tested using X-rays and ion beams. The detector attains an efficiency $> 96\%$ for ΔV_{GEM} = 366.6 V using proton beams. The actual size of the detector would be larger than the 31 cm × 31 cm GEM module. A large area triple GEM module which is a replica of the actual GEM module to be used in 1^{st} detector station during CBM experiment, has been assembled. The efficiency of the detector should be uniform with the high rate of particles and it should be capable of handling high flux of particles. The module has been tested for rate capability and uniformity with respect to efficiency and gain using intense proton beam. The efficiency of this full size GEM chamber reaches 96% for ΔV_{GEM} = 375.2 V at a gain of 2000. The efficiency of this detector is uniform with the rate of the ion beam up to 1 MHz/cm^2. Beyond this, the efficiency slightly decreases ($\sim 2\%$). The large area triple GEM can be used to design the MUCH of CBM experiment for tracking the dimoun. The efficiency and the gain of the detector should be stable for its long-term operation in real time experiment. The ageing of the GEM detector has been studied for a 10 cm × 10 cm GEM prototype using an strong ^{55}Fe source. The source is placed at a particular position of the detector for 750 hr. The gain of the detector has been calculated from time to time at an interval of 15 minutes. It is observed that the gain of the detector is stable over an accumulated charge of 12 mC$/$mm^2. Although there are small fluctuation in the normalised gain of the detector about the mean value, the fluctuation are small compared to the allowed value (up to 25 $\%$ due to inhomogeneity of geometry and gap sizes).

Bibliography

[1] C. Altunbas *et al.*, Nucl. Instr. Meth. A **490** (2002) 177-203.

[2] I. Vai *et al.*, Nucl. Instr. Meth. A **824** (2016) 586-588.

[3] C. Calabria *et al.*, Nucl. Instr. Meth. A **273-275** (2016) 1042-1047.

[4] B. Surrow, Nucl. Instr. Meth. A **617** (2010) 196-198.

[5] M. Alfonsi *et al.*, Nucl. Instr. Meth. A **581** (2007) 283.

[6] M. Alfonsi *et al.*, Nucl. Instr. Meth. A **518** (2004) 106.

[7] G. Bencivenni *et al.*, Nucl. Instr. Meth. A **488** (2002) 493.

[8] B. Ketzer *et al.*, Nucl. Instr. Meth. A **732** (2013) 237-240.

[9] M. Alfonsi *et al.*, Nucl. Instr. Meth. A **525** (2004) 17-19.

[10] A. S. Brogna *et al.*, Nucl. Instr. Meth. A **568** (2006) 301.

[11] EU-FP6 project.

[12] I. Sorokin *et al.*, Nucl. Instr. Meth. A **714** (2013) 136-140.

[13] R. P. Adak *et al.*,Proc. Indian. Natn. Sci. Acad. **81** (2015) 36-39.

[14] S. Ahmad *et al.*, Nucl. Instr. Meth. A **775** (2015) 139-147.

[15] CBM Progress Report 2013, GSI, Darmstadt

[16] L. Franconi *et al.*, Status of no-stretch no-spacer GEM assembly, the NS2 technique method and experiment result, 2012.

[17] You Wen-Hao *et al.*, arXiv:1405.1872 [physics.ins-det].

[18] J. Saini *et al.*, Proceedings of the DAE-BRNS Symp. on Nucl. Phys. **60** (2015) 9;.

[19] Rama Prasad Adak *et al.*, arXiv:1604.02899 [physics.ins-det].

[20] R. P. Adak *et al.*, Proceedings of the DAE Symp. on Nucl. Phys. **60** (2015) 1018.

[21] RD51 Collaboration.

[22] Supriya Das, Performance of a small triple GEM prototype.

[23] S. Biswas et al., JINST **8** (2013) C12002, [arXiv:1310.0642].

[24] R. N. Patra *et al.*, Nucl. Instr. Meth. A **824** (2016) 501

[25] Y. Assran, A. Sharma, arXiv:1110.6761 [physics.ins-det].

[26] M. C. Altunbas *et al.*, Nucl. Instr. Meth. A **515** (2003) 249.

[27] R. P. Adak *et. al.*, JINST **11** (2016) T10001, [arxiv:1608.00562].

[28] A. Orthen *et al.*, Nucl. Instr. Meth. A **512** (2003) 476.

[29] A. Orthen *et al.*, Nucl. Instr. Meth. A **500** (2003) 163.

Chapter 5

Conclusion and Outlook

In this thesis, the R&D on GEM detectors for their use to track the dimuons in the CBM experiment at FAIR has been discussed. The MUCH detector in the 1^{st} station will have to be operated at a particle rate of 1 MHz/cm^2. This is the most vital challenge for the detector to be used in MUCH system. Most of the presently available detector technologies are not compatible to handle such a high rate of particles. Out of the presently available detectors, GEM detector can handle such high rate of particles. The R & D on GEM detector started with a small 10 cm × 10 cm triple GEM detector. This detector was tested using pion and muon beams at CERN. The detector has an efficiency of 95$\%$ at a voltage across the GEM foil of 350 V.

Using mini-MUCH type set up using three GEM detectors, the tracks of the particles are reconstructed using the hits at the GEM detectors. The track point residue of the GEM detector is calculated using the data for the array of three GEM detectors. The track point residue obtained from the data is 0.12 cm which is comparable to the value calculated from the size of the readout pad (0.19 cm).

In CBM experiment the MUCH detector will be placed in a harsh environment exposing to neutrons about 10^{12} n$_{eq}$/cm^2/s. A GEM detector with a ^{55}Fe X-ray source fixed on it, was tested with neutron environment at VECC. For the highest neutron flux of 10^5/cm^2/s, corresponding to a beam current of 4 μA, there are about 350 hits/cm^2/s in the detector. The number of hits in the detector by the background neutrons will not affect significantly the track reconstruction as obtained from the result.

Next, a 31 cm × 31 cm, medium size triple GEM prototype was tested. The readout plane is a trapezium of parallel legs of 7.5 cm and 23 cm with a height of 31 cm. The detector has readout anode pads with dimension progressively increasing from 2.97 mm to a maximum of 11.21 mm. This detector is successfully tested using proton beam at COSY, Jülich university, Germany. The data was acquired in self-triggering mode using nXYTER based readout electronics. The data is analysed using the GSI object oriented online offline (GO4) framework. The efficiency of the detector is found to be $> 95\%$ at ΔV_{GEM}= 366.6 V.

Finally, a large trapezoidal shaped triple GEM detector was tested using intense proton beam at COSY. This is the realistic size detector module which will be used in MUCH in future. The time correlation between the hits on the GEM detector and the trigger signal is studied. The actual hits on the detector have a definite correlation in time with the trigger signal. A time correlation spectra with a sigma of 13.71 nsec is obtained at ΔV_{GEM}= 371 V. The distribution of the ADC of the hits are studied to obtain the gain of the detector. The variation of the gain over different regions of the detector is studied for 39 points. The gain looks reasonably stable with a spread of 12% about the mean value. The pad multiplicity of the large GEM prototype is calculated. The average pad multiplicity at a region of pad size 5.46 mm is found to be 1.2 at ΔV_{GEM}= 355.2 V. It is observed that the pad multiplicity slowly increases with the increase in ΔV_{GEM} due to the increase of the avalanche size. The efficiency of the detector reaches 96% at ΔV_{GEM}= 375.2 V. The variation of the efficiency and gain of the detector with the flux of the incident particles is studied. The efficiency is uniform with the flux of the incident particles up to 2.8 MHz/cm^2 with a fluctuation of 2%. The gain of the detector is also found to be uniform with the flux of the particles with a small fluctuation of $\sim$9%. The GEM detector can be operated at high efficiency and this detector can handle high flux of particles beyond the particle rate expected at the 1^{st} station of the MUCH. The particle rate at 2^{nd} station is lower, so GEM detector can detect the particle in the 2^{nd} station comfortably.

The ageing of the GEM detector due to the charge accumulated inside the detector during its long term operation is studied with an X-ray source. After accumulating charge inside the detector for a period of 750 hrs corresponding to a charge of 12 mC/mm^2, no significant change in terms of gain of the detector is observed. Therefore, no ageing is observed for its long term operation in laboratory.

The GEM detectors will be placed behind hadron absorbers in CBM experiment. The incoming beam will produce a shower of particle while passing through the absorber. The large GEM will face this shower of particles similar to the environment in an actual experiment. We call it the mini-MUCH setup which had been used for testing a medium size (31 cm × 31 cm). So, the large realistic size GEM prototype should be tested using absorber. The track point resolution has to be calculated for the large GEM prototype in this mini-MUCH setup. The readout pads of the large GEM are of different dimensions. The measurement of the track point resolution at different regions with varying readout pad size is very important for the reconstruction of the tracks of the particles. The gain and the efficiency of the large GEM detector may vary over different regions of the detector. The variation in gain and efficiency should be measured. The GEM detectors are less prone to spark due to the separation between the amplification region and the readout region. The spark probability of a 10 cm × 10 cm GEM has been done for the CBM experiment. It is expected that the spark probability is low for the large GEM module but this should be varified. The long-term operation of the large GEM detector in a harsh radiation environment may cause an ageing to the detector. A measurement of the ageing should be done using a large GEM prototype. The radiation hardness of the electronics associated with large GEM detector should be varified in order to sustain inside the harsh radiation environment.